

## REPORT DOCUMENTATION PAGE

Public "POC" or burden for this collection of information is estimated to average 1 hour per response, including the time for reviewing instructions, searching existing data sources, gathering and maintaining the data needed, and completing and reviewing the collection of information. Send comments regarding this burden estimate or any other aspect of this collection of information, including suggestions for reducing this burden, to Washington Headquarters Services, Directorate for Information Operations and Reports, 1215 Jefferson Davis Highway, Suite 1204, Arlington, VA 22202-4302, and to the Office of Management and Budget Paperwork Reduction Project (0704-0188), Washington, DC 20503.

1. AGENCY USE ONLY (Leave Blank)	2. REPORT DATE	3. REPORT TYPE AND DATES COVERED
	July 25, 1995	Final Report; June 1, 1992 - July 1, 1995

4. TITLE AND SUBTITLE	5. FUNDING NUMBERS
-----------------------	--------------------

Solidification Processing & Mechanical Behavior of Ta-W/W<sub>p</sub> Refractory Metal Base Composites

6. AUTHOR(S)	8. PERFORMING ORGANIZATION REPORT NUMBER
--------------	--

E.J. Lavernia and F. A. Mohamed

7. PERFORMING ORGANIZATION NAME(S) AND ADDRESS(ES)	9. SPONSORING / MONITORING AGENCY NAME(S) AND ADDRESS(ES)	10. SPONSORING / MONITORING AGENCY REPORT NUMBER
--	---	--

Department of Chemical/Biochemical Engineering and Materials Science  
University of California, Irvine  
Irvine, California 92717-2575

DTIC  
SELECTED  
OCT 10 1995  
G

11. SUPPLEMENTARY NOTES
-------------------------

The views, opinions and/or findings contained in this report are those of the author(s) and should not be construed as an official Department of the Army position, policy, or decision, unless so designated by other documentation.

12a. DISTRIBUTION / AVAILABILITY STATEMENT	12b. DISTRIBUTION CODE
--	------------------------

Approved for public release; distribution unlimited.

13. ABSTRACT (Maximum 200 words)
----------------------------------

In this research program, two solidification processing technique, that is spray atomization and deposition, and low pressure plasma spraying (LPPS) were both experimentally and theoretically studied for processing refractory metals and alloys, such as tantalum alloys and tungsten, and refractory intermetallic composites, such as SiC reinforced MoSi<sub>2</sub> composites. In this final report, the aforementioned experimental and numerical results are described and discussed in four respective sections, which are numerical analysis of droplet-gas interactions in spray atomization of Ta-2.5w alloy; low pressure plasma spraying of tungsten; numerical analysis of porosity evolution during low pressure plasma spraying of tungsten; and microstructure and behavior of low pressure plasma deposited SiC-reinforced MoSi<sub>2</sub>. In addition, the work on the elevated temperature deformation of 6061 aluminum alloy and SiC particulate reinforced 6061 aluminum composites is also included.

199510050361 DTIC QUALITY INSPECTED 6

14. SUBJECT TERMS	15. NUMBER OF PAGES	
Refractory metals; Intermetallics; Composites; Spray atomization and deposition; low pressure plasma spraying; Numerical analysis; Creep testing; Tungsten; Tantalum.		
16. PRICE CODE		
17. SECURITY CLASSIFICATION OF REPORT UNCLASSIFIED	18. SECURITY CLASSIFICATION OF THIS PAGE UNCLASSIFIED	19. SECURITY CLASSIFICATION OF ABSTRACT UNCLASSIFIED
		20. LIMITATION OF ABSTRACT UL

**Solidification Processing & Mechanical Behavior of Ta-W/W<sub>p</sub>**  
**Refractory Metal Base Composites**

**FINAL REPORT**

Submitted to:

Edward S. Chen  
Materials Science Division  
U.S. Army Research Office

Submitted by

Enrique J. Lavernia  
Associate Professor

and

Farghali A. Mohamed  
Professor

June 1, 1992-July 1, 1995

U.S. ARMY RESEARCH OFFICE

29410-MS

Grand Number: DAAL03-92-G-0181

Accesion For	
NTIS	CRA&I <input checked="" type="checkbox"/>
DTIC	TAB <input type="checkbox"/>
Unannounced	<input type="checkbox"/>
Justification _____	
By _____	
Distribution / _____	
Availability Codes _____	
Dist	Avail and / or Special _____
A-1	

Materials Science and Engineering  
Department of Chemical/Biochemical Engineering and Materials Science  
University of California, Irvine  
Irvine, CA 92717

APPROVED FOR PUBLIC RELEASE;  
DISTRIBUTION UNLIMITED

THE VIEWS, OPINIONS, AND/OR FINDINGS CONTAINED IN THIS REPORT ARE  
THOSE OF THE AUTHOR(S) AND SHOULD NOT BE CONSTRUED AS AN  
OFFICIAL DEPARTMENT OF THE ARMY POSITION, POLICY, OR DECISION,  
UNLESS SO DESIGNATED BY OTHER DOCUMENTATION

**TABLE OF CONTENTS**

LIST OF TABLES.....	iv
LIST OF FIGURES.....	v
FOREWORD.....	1
I. INTRODUCTION.....	2
II. BACKGROUND .....	5
2.1. Refractory Metals and Refractory Intermetallics .....	5
2.2. Kinetic Energy Applications.....	8
2.3. Spray Atomization and Deposition.....	10
2.4 Low Pressure Plasma Spraying.....	12
2.5. Porosity .....	13
III. NUMERICAL ANALYSIS OF DROPLET-GAS INTERACTIONS IN SPRAY ATOMIZATION OF TA-2.5W ALLOY .....	16
3.1. Model Formation.....	16
3.1.1. 2-D Flow Model .....	16
3.1.2. Lumped Parameter Formulation .....	19
3.1.3. Rapid Solidification of Droplets .....	21
3.2. Results and Discussion.....	24
3.2.1. Velocity Evolution and 2-D Distribution of Atomization Gas and Droplets In Spray Cone.....	24
3.2.2. Temperature, Cooling and Solidification Histories of Droplets In Spray Cone.....	27
3.2.3. 2-D Distribution of Temperature, Cooling Rate and Solid Fraction of Droplets In Spray Cone.....	31
3.2.4. Microstructural Characteristics of Particles and Sprayed Materials.....	36
IV. LOW PRESSURE PLASMA SPRAYING OF TUNGSTEN .....	38
4.1. Experimental Procedures.....	38

4.2.	Results and Discussion.....	39
4.2.1.	Microstructure of Plasma Sprayed Tungsten.....	39
4.2.2.	Formation of Porosity During Plasma Spraying of Tungsten.....	39
4.2.2.1.	Porosity From Unmelted Particles .....	43
4.2.2.2.	Porosity From Melted Powder Particles.....	48
4.2.2.3.	Porosity From Gas Entrapment .....	50
4.2.2.4.	Porosity From Solidification Shrinkage.....	51
4.2.2.5.	Porosity From As-Received Powders .....	52
V.	NUMERICAL ANALYSIS OF POROSITY EVOLUTION DURING LOW PRESSURE PLASMA SPRAYING OF TUNGSTEN.....	54
5.1.	Numerical Model and Computational Method.....	54
5.2.	Results and Discussion.....	57
5.2.1.	Formation of Micro-Pores During Deformation of A Single Droplet on Flat Surface.....	57
5.2.3.	Effect of Droplet Viscosity On Formation of Micro-Pores .....	62
5.2.4.	Effect of Initial Impact Velocity On Formation of Micro-Pores.....	63
5.2.5.	Formation of Micro-Pores During Interaction of Multiple Droplets On Flat Surface .....	64
VI.	MICROSTRUCTURE AND BEHAVIOR OF LOW PRESSURE PLASMA DEPOSITED SiC- REINFORCED MoSi <sub>2</sub> .....	77
6.1.	Experimental Procedures.....	77
6.1.1.	Low Pressure Plasma Deposition of SiC- Reinforced MoSi <sub>2</sub> .....	77
6.1.3.	Fracture Toughness .....	78
6.1.4.	Creep Testing .....	78
6.2.	Results and Discussion.....	78
6.2.1.	Density and Porosity of Low Pressure Plasma Deposited SiC-Reinforced MoSi <sub>2</sub> .....	78
6.2.2.	Microstructure of Low Pressure Plasma Deposited SiC- Reinforced MoSi <sub>2</sub> .....	79
6.2.3.	Fracture Toughness of Low Pressure Plasma Deposited SiC-Reinforced MoSi <sub>2</sub> .....	79
6.2.4.	Creep Behavior of Low Pressure Plasma Deposited SiC- Reinforced MoSi <sub>2</sub> .....	81

VII. HIGH TEMPERATURE DEFORMATION BEHAVIOR OF 6061 ALUMINUM ALLOY AND SiC PARTICULATE REINFORCED 6061 ALUMINUM ALLOY.....	87
7.1. Experimental Procedures.....	87
7.2. Results and Discussions .....	87
7.2.1. Creep Curves of $\text{SiC}_p$ -6061 Al and 6061 Al .....	87
7.2.2. Activation Energy for Creep and Stress Dependence of the Steady-State Creep Rate .....	88
7.2.3. Analysis of Creep Behaviors of $\text{SiC}$ -6061 Al and 6061 Al.....	95
7.2.4. Power Law Creep for the Composite .....	97
7.2.5. Correlation Between the Present Results and Various Analytical Treatments.....	102
VIII. SUMMARY.....	106
NOMENCLATURE.....	110
REFERENCES .....	114
LIST OF PUBLICATIONS .....	122
LIST OF PARTICIPATING SCIENTIFIC PERSONNEL.....	127

## LIST OF TABLES

Table 1.	Physical Properties of Tantalum .....	5
Table 2.	Mechanical Properties of Tantalum .....	6
Table 3.	Values of $\Delta H_s^\circ$ and $\Delta H_f^\circ$ for Tantalum .....	6
Table 4.	Parameters Used in Computations.....	17
Table 5.	Physical Properties of Alloy Used in Computations.....	19
Table 6.	Physical Properties of N <sub>2</sub> Atomization Gas Used in Computations .....	19
Table 7.	LPPS Processing Parameters.....	38
Table 8.	Measured Density and Porosity For Deposited W Specimen.....	39
Table 9.	Comparison of Gas Content Before and After Plasma Deposition.....	50
Table 10.	LPPS Processing Parameters Used to Prepare the SiC/MoSi <sub>2</sub> Composites .....	77
Table 11.	Density Characteristics .....	79
Table 12.	Microhardness and Fracture Toughness for the Plasma-Sprayed SiC/MoSi <sub>2</sub> Composites .....	81
Table 13.	The Values of $\tau_0$ Obtained from the Plot of $\dot{\gamma}^{1/5}$ vs. $\tau$ For 30 vol.% SiC <sub>p</sub> -6061 Al and 6061 Al. ....	92
Table 14.	Values of The Load Transfer Coefficient, $\alpha$ , in 30 vol.% SiCp-6061 Al.....	98

## LIST OF FIGURES

Figure 1.	Schematic diagram showing spray atomization and deposition processing. ....	11
Figure 2.	Velocity field of the atomization gas in the spray cone.....	25
Figure 3.	Velocity field of the droplets of 60 $\mu\text{m}$ diameter in the spray cone.....	26
Figure 4.	Axial velocity evolution of the atomization gas and droplets along the axis line of the spray cone.....	27
Figure 5.	Axial velocity distributions of the atomization gas and droplets in the radial direction of the spray cone. ....	28
Figure 6.	Temperature histories of droplets along the axis line of the spray cone.....	29
Figure 7.	Cooling histories of droplets along the axis line of the spray cone.....	29
Figure 8.	Solidification histories of droplets along the axis line of the spray cone.....	30
Figure 9.	Temperature distributions of droplets in the radial direction of the spray cone. ....	33
Figure 10.	Cooling rate distributions of droplets in the radial direction of the spray cone.....	34
Figure 11.	Solid fraction distributions of droplets in the radial direction of the spray cone .....	35
Figure 12.	Second dendrite arm spacing and cooling rate during post-recrystallization solidification as a function of droplet diameter.....	36
Figure 13.	Microstructure of LPPS processed W .....	40
Figure 14.	Morphology of LPPS processed W.....	41
Figure 15.	The distribution of grain sizes obtained from computerized image analysis.....	41
Figure 16.	Microstructure of as-polished cross section of LPPS processed W .....	42
Figure 17.	SEM micrographs showing the pores present: (a) intragranularly and (b) intergranularly in the plasma sprayed W.....	44
Figure 18.	Morphology of as-received W powders.....	45
Figure 19.	The relationship between flight distance and surface temperature of particles for various particle sizes .....	46
Figure 20.	Surface temperature profile of a W particle versus particle flight distance.....	47
Figure 21.	The formation of pores due to the interaction (a) between partially melted particles and (b) between partially melted particles and deposition surfaces .....	49

Figure 22. The formation of pores due to the stacking of flattened particles .....	50
Figure 23. The large pores observed in the LPPS processed W .....	51
Figure 24. SEM photograph showing solidification shrinkage in LPPS processed W .....	52
Figure 25. SEM photograph showing the pores present in the as-received W powders.....	53
Figure 26. Schematic showing computation method of micro-porosity .....	56
Figure 27. Deformation and solidification sequence of a single W droplet.....	58
Figure 28. Schematic diagram showing formation mechanism of micro-pores.....	59
Figure 29. Micro-porosity formed during droplet deformation and solidification and its dependence on substrate temperature and droplet temperature.....	60
Figure 30. Initial rising velocity of solid/liquid interface as a function of substrate temperature and droplet temperature .....	61
Figure 31. Separation time as a function of substrate temperature and droplet temperature .....	61
Figure 32. Micro-porosity formed during droplet deformation and solidification and its dependence on the initial impact velocity .....	63
Figure 33. Deformation and solidification sequence during interaction of two droplets in tandem .....	65
Figure 34. Deformation and solidification sequence during interaction of an axisymmetric toroidal ring and a droplet beneath it .....	66
Figure 35. Deformation sequence of a single droplet impinging onto a solid particle on a substrate .....	68
Figure 36. Deformation sequence of an axisymmetric toroidal liquid ring impinging onto a solid particle on a substrate.....	69
Figure 37. Deformation sequence of an axisymmetric toroidal liquid ring, co-existing in the same space level with a droplet at the symmetry axis, and impinging onto a solid particle on a substrate .....	70
Figure 38. Deformation sequence of an axisymmetric toroidal liquid ring, co-existing in the same space level with a droplet at the symmetry axis, and impinging onto two solid particles on a substrate .....	71
Figure 39. Deformation sequence of a single droplet impinging onto a solid, waved surface layer on a substrate .....	72
Figure 40. Deformation sequence of an axisymmetric toroidal liquid ring, co-existing in the same space level with a droplet at the symmetry axis, and impinging onto a solid, waved surface layer on a substrate .....	73
Figure 41. Deformation sequence of a single droplet impinging onto a solid, waved surface layer on a substrate .....	74

Figure 42. Deformation sequence of a single droplet impinging onto a solid, waved surface layer on a substrate.....	75
Figure 43. Deformation sequence of a single droplet impinging onto a solid, waved surface layer on a substrate.....	76
Figure 44. Microstructure of the plasma-sprayed SiC/MoSi <sub>2</sub> composite .....	80
Figure 45. Steady-state creep rate vs. true stress for plasma-sprayed SiC/MoSi <sub>2</sub> at various temperatures.....	82
Figure 46. Temperature dependence of the stress exponent.....	83
Figure 47. Creep rate versus reciprocal absolute temperature for plasma-sprayed SiC/MoSi <sub>2</sub> ....	84
Figure 48. Microstructure of plasma-sprayed SiC/MoSi <sub>2</sub> after creep testing.....	85
Figure 49. Creep behavior as a function of orientation at 1200°C and 1500°C.....	86
Figure 50. Example of creep curve for 30 vol.% SiC <sub>p</sub> -6061 Al and 6061 Al.....	88
Figure 51. Steady-state creep rate as a function of the applied stress .....	89
Figure 52. The variation in the apparent stress exponent with the applied stress for 30 vol% SiC <sub>p</sub> -6061 Al and 6061 Al.....	89
Figure 53. The variation of the apparent activation energy with the applied stress for 30 vol.% SiCp-6061 Al and 6061 Al.....	90
Figure 54. A plot of $\dot{\gamma}^{1/5}$ vs. $\tau$ for 30 vol.% SiCp-6061 Al and 6061 Al .....	93
Figure 55. A plot of logarithm of ( $\tau_o/G$ ) vs. 1/T for 30 vol.% SiC <sub>p</sub> -6061 Al and 6061 Al.....	94
Figure 56. Determination of the load transfer coefficient, $\tau_o$ , by plotting $\tau_{LT}$ as a function of ( $\tau_{com} - \tau_{o.com}$ ) for 30 vol.% SiCp-6061 Al .....	98
Figure 57. Schematic representation of the (modified) power creep law in conjunction with the effect of load transfer and the threshold stress.....	100
Figure 58. A plot of the normalized strain rate vs. the normalized effective stress for 30 vol.% SiC <sub>p</sub> -6061 Al and 6061 Al for n = 5.....	102

## FOREWORD

It is the objective of this research program to utilize solidification synthesis techniques to process tantalum-tungsten (and other refractories) metal composites with attractive combinations of microstructure, mechanical properties, and density. These processing techniques were selected for two main reasons. First, they have been successfully applied to numerous metallic systems, especially reactive alloys, and have led to significant improvements in microstructure and mechanical behavior. Second, these techniques are also advantageous in terms of manufacturing costs. The relevance of the proposed program to the Army will be on assessing the potential use of these high density materials in applications requiring high kinetic energy, such as penetrators. The selection of tungsten additions to tantalum was made on the basis of its extremely high density, which makes tantalum-tungsten alloys competitive with other tungsten alloys in applications that require high densities.

This final report summarizes both experimental and theoretical results on the processing refractory metal alloys and composites by using spray atomization and deposition, as well as low pressure plasma spraying.

## I. INTRODUCTION

Novel alloys based on the family of refractory metals -Zr, Hf, V, Nb, Ta, Mo, W and Re are attractive candidate materials for applications requiring high strength, thermal stability, corrosion resistance, and high density [1-13]. Niobium and tantalum, for example, combine ductility and toughness, as a result of their bcc structures, with a strong resistance to chemical attack by many liquid metals: Li < 1000°C, Na, K + Na K < 1000°C, Th-Mg < 850°C, U < 1400°C, Zn < 450 °C, Pb < 850°C, Bi < 500°C, and Hg < 600°C [1, 2]. In high energy applications that require maximum kinetic energy, such as projectiles, tungsten heavy alloys provide an attractive alternative to depleted uranium (DU), due to safety and other environmental hazards associated with DU [14-19]. Other applications of tungsten heavy alloys include: radiation shields, vibration damping devices, and electrodes [10, 13, 20-22].

The properties of refractory metal alloys are extremely sensitive to processing conditions [10, 12, 19, 21, 23]. Niobium and tantalum, for example, react with oxygen and nitrogen when melted in air at temperatures as low as 300-400°C [3]. The properties of tungsten heavy alloys are severely degraded by the presence of porosity [19, 21], and oxygen contamination during processing [18]. The extreme reactivity of this family of materials precludes their fabrication utilizing conventional techniques. Inspection of the available scientific literature shows that fabrication of refractory alloys has been successfully carried out utilizing arc-melting [3], electron beam melting [3], and liquid phase sintering [4, 5, 10, 12, 13, 20, 21]. In general, however, the high temperatures associated with melting and casting processes limit the types of alloying additions which can be utilized to strengthen these materials.

The above difficulties impose some limitations on our ability to take full advantage of the attractive properties of refractory alloys, and consequently, restrict the complete development of this important class of materials. While it is expected that efforts will continue to improve the procedures associated with traditional fabrication techniques, studying alternative fabrication processes to overcome the present drawbacks is highly desirable.

In this research program, two solidification processing technique, that is spray atomization and deposition, and low pressure plasma spraying (LPPS) were both experimentally and theoretically studied for processing refractory metals and alloys, such as tantalum alloys and tungsten, and refractory intermetallic composites, such as SiC reinforced MoSi<sub>2</sub> composites.

To elucidate the microstructural evolution of the droplets during spray atomization and deposition, a simple 2-D Lagrangian model was applied to investigate the momentum and thermal interactions that occur between N<sub>2</sub> atomization gas and Ta-2.5W (in wt.%) alloy droplets. The rapid solidification phenomena that are present during the droplet-gas interactions were considered by combining a 2-D model with a phase change kinetic model. A 4th-order Runge-Kutta-algorithm

was employed for the simultaneous solution of the 2-D non-linear differential equations of motion of droplets. Particular emphasis was placed on elucidating the spatial distribution of droplet velocity, temperature and rapid solidification histories, as well as the microstructural characteristics of solidified particles in the spray cone and the as-deposited materials. Such mathematical modeling is highly desirable, due to the large expense and difficulties associated with the melting and spray processing of the material considered in the numerical investigation. The selection of this alloy composition was promoted by recent interest in this material for heat exchangers and other welded-tube applications as a result of its unique combination of high melting temperature, high ductility, high density, high formability and ultra corrosion resistance at temperatures below 150 °C [24].

The high melting point, low oxidation resistance, and poor workability of W and W alloys have prompted the study and application of near-net shape processes as potential approaches to fabricate these materials. Plasma spraying is a promising near-net shape technique, which combines melting, quenching and consolidation into a single operation and produces very fine-grained and homogeneous microstructures [25-28]. The application of plasma spraying for the production of intricate shapes of W may be traced back to 1960's, when a W expansion nozzle and a W crucible were produced by plasma spraying [29]. Among the various plasma spraying techniques that are available, low pressure plasma spraying (LPPS) appears to yield the most promising results for a variety of materials, such as metallic alloys, intermetallic, ceramics, and composites [28]. More recently, it has been reported that W and W alloy structures may be readily fabricated by using low pressure plasma spraying (LPPS). These structures include tungsten rocket nozzles [28] and tungsten pipes with internal threads [30]. Moreover, the interest in LPPS processed W also encompasses alloys, such as W-Ni-Fe [31]. There are, however, several issues that must be resolved before optimal microstructure and properties may be achieved in LPPS processed W. Jackson, et al. [32], for example, note that incomplete melting of coarse W powders leads to excessive porosity in LPPS processed W. Accordingly, the study on LPPS processed W was undertaken with the objective of providing preliminary information on the evolution of microstructure. To accomplish this objective, the microstructure of the LPPS W was characterized in detail, paying particular attention to the presence of porosity, and contamination by oxygen, nitrogen and carbon. The mechanisms that govern the formation of porosity during LPPS were discussed in light of experimental results. Furthermore, numerical studies on porosity evolution in plasma spray deposition of W were undertaken to provide insight into the formation and evolution of porosity. The deformation, interaction and solidification of molten droplets impinging onto a flat and non-flat substrate during plasma spraying were investigated. The full Navier-Stokes equations coupled with the Volume Of Fluid (VOF) function were solved to determine the exact movement and interaction of droplets. A 2-domain method was employed for the treatment of the

thermal field and solidification problem within the flattening droplet to track the moving solid/liquid interface. A two-phase flow continuum model were employed for the simulation of the flow problem with a growing solid layer during droplet impingement. On the basis of the VOF function and the two-phase flow continuum model the micro-porosity is quantitatively calculated.

Molybdenum disilicide ( $\text{MoSi}_2$ ) has attracted considerable attention in recent years as an elevated temperature structural material to be used in gas turbine engines expected to operate at temperatures of up to  $1600^\circ\text{C}$  as a result of its unique combination of physical attributes, which include: moderate density of  $6.31 \text{ g/cm}^3$ , high melting point of approximately  $2030^\circ\text{C}$ , excellent oxidation resistance, and high modulus at elevated temperatures [33]. Monolithic  $\text{MoSi}_2$ , however, is brittle at room temperature, and moreover, generally exhibits low strength at elevated temperatures ( $>1200^\circ\text{C}$ ). Inspection of the available scientific literature reveals that it is possible to achieve dramatic improvements in the room temperature toughness and elevated temperature strength of  $\text{MoSi}_2$  through the selective addition of second phases. For example, the addition of  $\text{SiC}$  to  $\text{MoSi}_2$  leads to improvements in elevated temperature strength and fracture toughness [34-38], whereas the addition of ductile second phases (e.g.,  $\text{Ta}$ ) improve toughness [39, 40]. Accordingly, the study was undertaken with the objective of providing fundamental information on the microstructure and mechanical behavior of  $\text{MoSi}_2$  composites processed by LPPS. Thus, the microstructure, room temperature fracture toughness, and elevated temperature behavior of a  $\text{SiC}$ -reinforced  $\text{MoSi}_2$  composite processed by LPPS were reported and discussed.

In this final report, the aforementioned experimental and numerical results are described and discussed in four respective sections, which are numerical analysis of droplet-gas interactions in spray atomization of  $\text{Ta}-2.5\text{w}$  alloy; low pressure plasma spraying of tungsten; numerical analysis of porosity evolution during low pressure plasma spraying of tungsten; and microstructure and behavior of low pressure plasma deposited  $\text{SiC}$ -reinforced  $\text{MoSi}_2$ . In addition, the work on the elevated temperature deformation of 6061 aluminum alloy and  $\text{SiC}$  particulate reinforced 6061 aluminum composites is also included.

## II. BACKGROUND

### 2.1. Refractory Metals and Refractory Intermetallics

Novel alloys based on the family of refractory metals Zr, Hf, V, Nb, Ta, Mo, W and Re are attractive candidate materials for applications requiring high strength, thermal stability, corrosion resistance, and high density [1-13]. Of the refractory metals family, niobium and tantalum are attractive candidates for structural applications, as a result of their attractive combinations of chemical inertness and high toughness. The physical properties of tantalum are summarized in Table 1 [2]. Tantalum's high atomic weight makes it a good candidate material for applications requiring high density. In addition, tantalum exhibits extremely high ductility (>30%) as a result of its bcc crystal structure. This characteristic is attractive from the standpoint of metal working operations. For example, tantalum parts can be cold worked 95% without failure. Some of the mechanical properties of tantalum are summarized in Table 2.

In terms of corrosion resistance, tantalum offers a strong resistance to chemical attack by most liquid metals. Table 3 shows the heat of solution ( $\Delta H_s^\circ$ ) of hydrogen, nitrogen, and oxygen in tantalum, and the heat of formation ( $\Delta H_f^\circ$ ) of the corresponding tantalum-rich compounds, also with hydrogen, nitrogen and oxygen. The results shown in this table indicate that the heat of compound formation with H, N, and O is more negative than the heat of solution. In addition, the results show that  $\Delta H_f^\circ$  rises in the sequence H, N, and O indicating that there is a strong driving force to form metallic oxides [4]. However, at temperatures between 1600°C and 2400°C, tantalum exhibits relatively high nitrogen solubilities (0.1-10 at.%) even when exposed to relatively low nitrogen pressures. In summary, these results suggest that in order to derive maximum benefit

Table 1. Physical Properties of Tantalum [2]

Atomic Weight	180.95
Density	16.6 g/cc
Melting Point	2996° C
Boiling Point	5431° C
Coefficient of Thermal Expansion (RT)	6.5 x 10 <sup>-6</sup> /°C
Electrical Resistivity	13.5/cm
Electrical Conductivity	13.9% IACS
Specific Heat	0.140 J/g
Thermal Conductivity	0.544 J
Crystal Structure	bcc
Thermal Neutron Cross Section	21.3b

from tantalum-niobium alloys, it will be necessary to process them under strict atmospheric control.

The family of tungsten base alloys may be thought of as a special class of composite materials. They are unusual in that they consist of an extremely high volume fraction of a hard phase (e.g., tungsten) in a metal matrix, usually containing iron, nickel and tungsten [21, 41]. The extremely high melting point of tungsten precludes fabrication of these types of materials using conventional techniques, and as a result, they are usually formed by liquid phase sintering [41]. This procedure typically involves mixing elemental powders, followed by sintering at temperatures above the eutectic temperature [21]. The pioneering work of German and co-workers [5, 11, 13, 21, 41, 42] has demonstrated that the properties of these types of materials are extremely sensitive to alloy

Table 2. Mechanical Properties of Tantalum [2]

	Annealed	Cold-Worked
Ultimate Tensile Strength, MPa (ksi)	285 (41)	650 (95)
Yield Strength, MPa (ksi)	170 (25)	5
Elongation, %	30+	-
Reduction in Area, %	80 +	-
Hardness, HV	90	210
Poisson's Ratio	0.35	
Strain Hardening Exponent	0.24	
Elastic Modulus (Tension), GPa (psi)		186 (27 x 10 <sup>6</sup> )
Ductile Brittle Transition Temperature, °K		<75*
Recrystallization Temperature, °C		900-1200

\* Significantly affected by increasing interstitial contents.

Table 3. Values of  $\Delta H_s^\circ$  and  $\Delta H_f^\circ$  for Tantalum (KJ/g.atom) [4]

	Hydrogen	Nitrogen	Oxygen
$\Delta H_s^\circ$	-36.4	-182	-383
$\Delta H_f^\circ$	-	-204	-402

chemistry and processing conditions. German and co-workers [21] noted that the mechanical properties of tungsten heavy alloys are strongly dependent on the amount of tungsten present. In this study they reported that although the ultimate tensile strength remained unchanged with increasing tungsten contents of up to 97%, the elongation declined continuously with tungsten content. Furthermore, increasing the amount of tungsten in the alloy leads to a decrease in the

volume of liquid phase present during sintering, making it more difficult to completely eliminate porosity. The presence of residual porosity in the alloy, not only inhibits densification, but also leads to a degradation in mechanical properties [21, 41]. In related work, Bose and German [12] showed that increasing the nickel/iron ratio from 7/3 to 8/2 increases the solubility of tungsten in the matrix, thereby increasing the grain size and ductility. Alternatively, molybdenum additions were noted to decrease the solubility of tungsten in the matrix, leading to smaller grain sizes and solid solution strengthening.

Refractory metal silicides (*e.g.*, MoSi<sub>2</sub>, NbSi<sub>2</sub>, TaSi<sub>2</sub>, and WSi<sub>2</sub>) are actively being used in a wide variety of applications, including: very large scale integrated (VLSI) devices (as gate materials), interconnectors, ohmic contacts, heating elements and Schottky barriers, partly due to their excellent chemical and thermal stability and low electrical resistivity [43-46]. In recent years, molybdenum disilicide (MoSi<sub>2</sub>) has attracted considerable attention [33, 34, 47-52] as an elevated temperature structural material as a result of its unique combination of physical characteristics, which include: a moderate density of 6.31 g/cm<sup>3</sup>, a high melting point of approximately 2030°C, an excellent oxidation resistance and a high modulus at elevated temperatures. In view of these attributes, it is not surprising that MoSi<sub>2</sub> is considered to be one of the most promising candidate materials to be used in gas turbine engines expected to operate at temperatures of up to 1600°C.

Although MoSi<sub>2</sub> is inherently brittle at low temperatures, it exhibits plasticity at temperatures above the BDTT (Brittle-Ductile Transition Temperature, about 1000°C). Accordingly, when MoSi<sub>2</sub> is deformed at temperatures below 1000°C, fracture often occurs without significant plastic deformation [53-55]. Interestingly, however, despite this lack of plasticity, a significant amount of slip markings ( $\{110\} \langle 3\bar{3}1\rangle$ ) near the fracture surface have been observed [53, 55, 56]. Moreover, in these studies, dislocations and stacking faults were reported to be active during elevated temperature deformation [53], thus rendering the deformation to be relatively ductile in nature, in contrast to that exhibited by most ceramic materials. At temperatures above 1300°C,  $\langle 100 \rangle$ - and  $\langle 110 \rangle$ -type dislocations have been reported to control the plastic deformation [53, 55-59]. In studies on the deformation behavior of SiC<sub>whisker</sub>-reinforced MoSi<sub>2</sub> metal matrix composites (MMCs), it was reported that when tested at 1200°C, no dislocation dissociation was observed in this material [56]. It was also suggested that the formation of stacking faults on  $\{110\}$  planes further improves the high-temperature ductility. The formation of stacking faults in MoSi<sub>2</sub> has been closely related to the phase stability of the C11<sub>b</sub> tetragonal structure, relative to that of the C40 hexagonal structure [53].

The C11<sub>b</sub> structure is a long-range ordered crystal structure made up by stacking three b.c.c. lattices along the *c* axis, as depicted. This particular crystal structure is thought to be responsible for the anisotropy that is frequently associated with MoSi<sub>2</sub>. For example, compression tests on MoSi<sub>2</sub> single crystals at evaluated temperatures showed that the dominant primary slip planes are

the {110} planes although slip on the {013} planes were also observed [53-59]. At approximately 1900°C, MoSi<sub>2</sub> transforms from a tetragonal (C11<sub>b</sub> type,  $a=3.202 \text{ \AA}$ ,  $c=7.851 \text{ \AA}$ ) to a hexagonal (C40 type) crystal structure.

Regarding the measurement of the elastic properties of MoSi<sub>2</sub>, some information is available. Nakamura and co-workers [57], for example, used a pulse echo method involving the measurement of elastic wave velocities in different orientations of MoSi<sub>2</sub> single crystals to determine the value of the elastic constants. Moreover, on the basis of this information, and using Voigt's, Reuss's, and Hill's approximations, Nakamura and co-workers [57] determined the magnitude of the bulk modulus,  $K$ , (209.7 GPa), Young's modulus,  $E$ , (439.7 GPa), shear modulus,  $G$ , (191.1 GPa), and Poisson's ratio,  $\nu$ , (0.151) for polycrystalline MoSi<sub>2</sub>.

Regarding environmental stability, MoSi<sub>2</sub> exhibits an excellent resistance to oxidation, equivalent to that of SiC. This is evidenced by the successful utilization of MoSi<sub>2</sub> as heating elements capable of operating in air, at temperatures in excess of 1500°C [60-63]. In particular, the best grade of MoSi<sub>2</sub> heating element, commercially known as "Kanthal Super" is capable of operating up to a temperature of 1800°C. This material consists of a mixture of fine MoSi<sub>2</sub> particles bonded together with an aluminosilicate ( $x\text{Al}_2\text{O}_3.y\text{SiO}_2$ ) glass phase [63]. The excellent oxidation resistance of MoSi<sub>2</sub> is attributed in part to the formation of a self-healing, glassy silica (SiO<sub>2</sub>) layer, which prevents the MoSi<sub>2</sub> matrix from undergoing further oxidation. However, this low melting-point, glassy phase is detrimental to the elevated temperature strength. The formation of weak second phase or liquid phase along grain boundaries drastically enhances grain boundary sliding (in MoSi<sub>2</sub>) and mass transport during elevated temperature exposure, and thus reduces creep resistance. In addition, the relative low elevated temperature strength of MoSi<sub>2</sub> further diminishes the creep resistance.

On the basis of the above findings, it is evident that despite its attractive combinations of elastic properties and oxidation resistance, MoSi<sub>2</sub> is inherently brittle when deformed at temperatures below 1000°C, and furthermore, exhibits a poor creep resistance at temperatures above 1200-1300°C. Therefore, investigators have sought to achieve further improvements in low temperature ductility and elevated temperature strength by blending MoSi<sub>2</sub> with a soft metallic phase (*e.g.*, ductile phase reinforcement) and a hard ceramic phase (metal matrix composites), respectively [33, 34, 47-52].

## 2.2. Kinetic Energy Applications

The unique combination of elevated melting point and high density that is characteristic of tungsten and its alloys, has prompted their utilization in defense applications, particularly those requiring very high densities, such as kinetic energy penetrators. The performance of kinetic

energy penetrators depends on many variables, such as penetrator material properties and geometry, penetration and failure mechanisms, launch dynamics, velocity, mass, and target material properties and geometry [64]. The design of modern penetrators, as indicated by Ekbom et al. [65] is based on the principle that the kinetic energy is concentrated on as small an area of the target as possible so that the penetration performance is maximized. Consequently, the geometry of penetrators is typically akin to that of a long, thin rod with large length to diameter ratios (usually 10 to 20); these are described as long rod kinetic energy penetrators. In order to achieve as high a kinetic energy as possible, the density of a material represents one of the key components in the design of successful kinetic energy penetrators, since the kinetic energy that a long rod penetrator brings to the target needs to be concentrated in a small region. Moreover, the use of high density materials for penetrators plays an important role in reducing aerodynamic losses, and in reducing flight time [66]. Considering the factors such as availability, cost and properties, only two high density materials, (i.e., depleted uranium (DU) and tungsten heavy alloys), have been developed and used in the application of kinetic energy penetrators [64, 66-70]. As a result of their superior terminal ballistic performance, DU alloys are currently the most widely used and favored materials for long rod kinetic energy penetrators. However, because of increasing environmental concerns and political pressures related to the contamination that results from residual low-level radiation of DU materials, finding suitable substitutes for these alloys has become increasingly necessary [64, 68, 71]. As a result, tungsten-based alloys have been developed and used as long rod kinetic energy penetrators. However, for two types of targets that are typically used, that is, monolithic semi-infinite targets (the flight direction of penetrators is normal to targets) and oblique, spaced array targets (the targets are composed of multiple plates and the flight direction of penetrators is at an angle to targets), terminal ballistic performance of tungsten-based alloys is inferior to that of DU alloys [64]. To overcome the lower performance of tungsten alloys, numerous research efforts are actively underway with the objective of improving the performance of tungsten-based alloys to match that of DU materials. The high performance of DU alloys is recognized to be attributed to the self-sharpening effects observed during penetration [68]. In the case of classical tungsten heavy alloy penetrators, however, self-sharpening is not observed during ballistic tests [64, 67] which is thought to be the primary reason for their poor performance. The self-sharpening phenomenon is a result of adiabatic shear or flow localization that generally occurs during material deformation at high strain rates or at low temperatures. Therefore, increasing the propensity of tungsten-based alloys to adiabatic shear or flow localization has been one of the primary objectives of the research and development of these alloys. The adiabatic shear or flow localization of a material is functions of the mechanical properties of the material, such as the work-hardening exponent, and thermal properties, such as specific heat, thermal conductivity and temperature dependence of yield stress (thermal softening). It is predicted that adiabatic shear

banding will be promoted by low strain hardening and low strain rate hardening (corresponding to a small work-hardening exponent), and high thermal softening [72, 73]. Moreover, on the basis of ballistic experiments, Dowding [67] indicated that the occurrence of adiabatic shear is preferred in a matrix that is composed of elements with low melting point, low density, low crystal symmetry and low average atomic number.

### 2.3. Spray Atomization and Deposition

Recently, spray atomization and deposition processes have received considerable attention for the synthesis of high performance materials, including metal matrix composites (MMCs) as a result of a number of factors. First, because of highly efficient heat convection during atomization, relatively low processing temperatures can be maintained, and hence, deleterious interfacial reactions can be minimized. This provides the opportunity to process metal/ceramic combinations that would otherwise react extensively when exposed to elevated temperatures. Second, spray atomized and deposited materials have been reported to exhibit some of the characteristics associated with rapid solidification, namely: fine grained microstructures, increased solid solubilities, non-equilibrium phases and the absence of macro-segregation. Third, spray atomization and co-deposition processes have the potential of being utilized for near net shape manufacturing of difficult to form materials, such as intermetallics (e.g., Ni<sub>3</sub>Al, TiAl). Spray atomization and co-deposition processing involves the mixing of the reinforcements and the matrix in a regime of the phase diagram where the matrix contains both solid and liquid phases. In principle, such an approach will inherently avoid the extreme thermal excursions, with concomitant degradation in interfacial properties and extensive macrosegregation, normally associated with casting processes. Furthermore, this approach also eliminates the need to handle fine reactive particulates, as is necessary with powder metallurgical processes.

During spray atomization and co-deposition, a matrix material is disintegrated into a dispersion of droplets with an average size denoted as  $d_{50}$  using high velocity inert gas jets. Simultaneously, ceramic particulates are co-injected into the atomized spray at a previously determined spatial location ( $Z_i$ ) and angle,  $\phi$ , as shown in Figure 1. Also shown in Figure 1 are the primary physical properties and synthesis parameters governing the resultant average droplet size during atomization ( $d_{50}$ ); the physical characteristics and synthesis parameters of the reinforcing phase ( $Fe_\phi$ ); and the two principal modes of heat extraction: convection ( $Q_n$ ) and conduction ( $Q_c$ ). The injection distance,  $Z_i$ , is determined on the basis of numerical analysis of the fraction solid contained in the atomized matrix as a function of flight distance. This synthesis approach attempts to achieve interfacial control by injecting the reinforcing particulates at a spatial location where the atomized

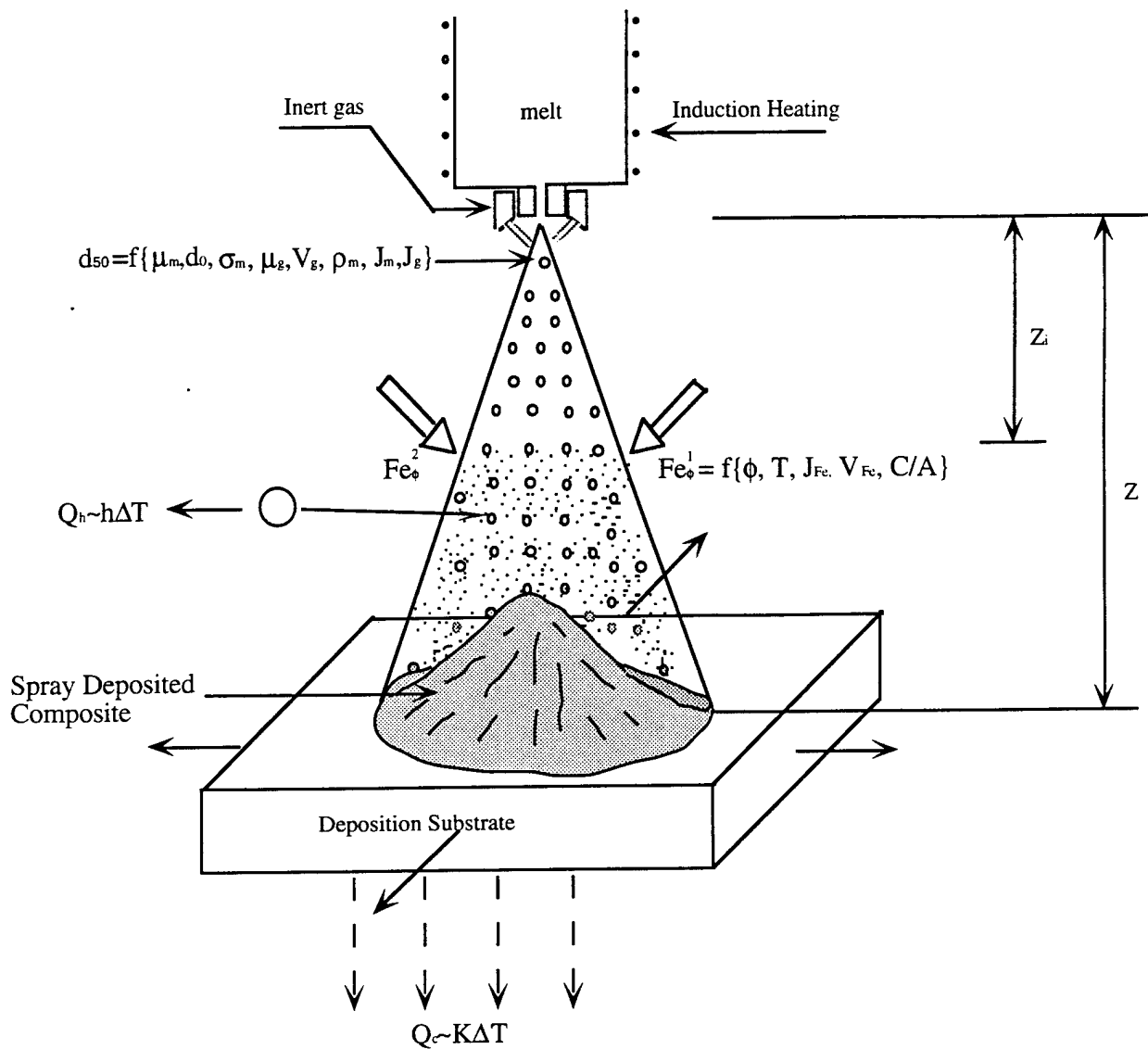


Figure 1. Schematic diagram showing spray atomization and deposition processing.

matrix spray contains a limited amount of volume fraction liquid. In this manner, contact time, thermal exposure of the reinforcing particulates to the partially solidified matrix, and interfacial reactions can be minimized. In order to avoid extensive oxidation of the matrix during processing, the experiments are typically conducted inside of an environmental chamber.

## 2.4 Low Pressure Plasma Spraying

Over the past several decades, plasma technology has been successfully exploited as a high enthalpy heat source (capable of reaching temperatures in excess of  $10^4$  K) to heat, melt, or vaporize a wide variety of materials. Plasma deposition has also been widely used to coat materials for corrosion and wear protection; to process superconducting materials [74]; and more recently, to synthesize bulk structural materials, including composites [75-77]. Moreover, plasma processing may be readily utilized to accelerate the kinetics of a particular chemical reaction, and thereby enhance the formation of desirable reaction products [31]. Among the various types of plasma techniques that are actively being used to synthesize structural materials, low-pressure plasma deposition (LPPS) has been used to produce relative dense (~98%) high purity deposits, with low residual thermal stresses [30].

LPPS technique yields advantages such as very small grain size, chemical homogeneity, non-equilibrium solubility and near final-shape production. In LPPS, the process is carried out in an evacuated chamber, which permits higher pressure ratios leading to higher gas velocities. The major advantages of LPPS are higher particle velocities and transferred arc heating of substrate , both of them improve deposit density. During LPPS process, an inert gas stream, such as Ar or N<sub>2</sub>, is commonly used to accelerate the powder particles as they are being injected into the plasma gases. Due to the high speed of the plasma gases, exceeding Mach 3 in some cases, the time spent from injection to deposition is almost infinitesimal (on the order of milliseconds). To obtain optimal microstructural characteristics during plasma spraying, it is therefore critical to select appropriate gun-to-substrate distances by taking into account factors such as alloy composition and particle size. If the particles are too large, for example, they will not melt completely, whereas if the particles are too small, they may be vaporized by the plasma. Similarly, particle morphology has been shown to influence the final microstructure of plasma-sprayed materials and spherical particles are preferred over irregularly-shaped particles, due to the better fluidity from spherical particles which can provide a better powder feeding control and thus a better control on the final microstructure.

Plasma processes may be readily utilized to prepare composite materials, simply by spraying, either pre-blended composite particles, or by simultaneously co-spraying metal and ceramic particles. In related work, Castro et al. [40, 78] successfully fabricated monolithic and composite MoSi<sub>2</sub> using the LPPS technique. The density of both reinforced and monolithic plasma-sprayed MoSi<sub>2</sub> was noted to be in the 95~98% range, and the materials exhibited a highly-refined microstructure. Moreover, the hardness and fracture toughness of the LPPS-processed materials were noted to be significantly improved relative to that of conventionally-processed materials. An

interesting, although not surprising, characteristic that was observed in the LPPS-processed material was the presence of a laminar, plate-like microstructure. When fracture tested in a direction parallel to the principal axis of the plates, preferential crack growth occurred along the prior splat-boundaries, suggesting less-than-optimum inter-particle bonding. In related work, Tiwari et al. [79] used the vacuum plasma spraying (VPS) technique to prepare monolithic,  $TiB_2$ -based and  $SiC$ -based  $MoSi_2$  composites. In this study, highly-dense monolithic and composite  $MoSi_2$  were fabricated with concomitant improvement in toughness response. Various reinforcement morphologies were reported, including splat-like  $TiB_2$  and relatively-equiaxed  $SiC$ . These morphologies were attributed to the concurrent melting of  $TiB_2$  and the sublimation of  $SiC$ , respectively. It is worth noting that the reactant content, which resulted in the formation of amorphous  $SiO_2$ , was significant increased via this technique. More recently, Jeng et al. [80] used a plasma synthesis approach to manufacture  $SiC$ -reinforced  $MoSi_2$  composites. Their work was conducted under a low vacuum environment in a industrial-scale plasma spray unit. In this study, dense composites with improved toughness were obtained. No preferential crack growth along the transverse direction (the direction perpendicular to the spray direction) was observed, indicating a well-bonded interface. In the same study, a very high creep rate was found, and it was attributed to the formation of  $SiO_2$ .

## 2.5. Porosity

In manufacturing processes involving the consolidation of numerous solidifying droplets, such as in spray atomization and deposition, and plasma spraying, porosity is an inherent problem. Porosity typically reduces useful properties such as bond strength, hardness and corrosion resistance, degrading the deposited coatings or bulk materials.

In spray atomization and deposition process, an important microstructural characteristic frequently associated with spray deposited materials is the presence of a finite amount of non-interconnected porosity [81-84]. The overall amount of porosity present in spray deposited materials depends on: (a) the thermodynamic properties of the material, (b) the thermodynamic properties of the gas, and (c) the processing parameters. Under conditions typical for aluminum alloys, for example, the amount of porosity present in spray deposited materials has been reported to be in the 1 to 10% range. In addition, the size distribution of pores is bimodal, with a large proportion of pore sizes in the 1-2  $\mu m$  and 10  $\mu m$  range. It has been suggested that the origin of porosity in spray atomized and deposited materials may be attributed to one or a combination of the following mechanisms: (a) gas entrapment, (b) solidification shrinkage, (c) interparticle porosity. The first mechanism, gas entrapment, is anticipated as a result of the limited solid solubility of inert gases in most structural materials. As the temperature of the material decreases during

solidification, any amount of gas that might have dissolved during the melting and superheating stage will be rejected into the matrix, leading to the formation of gas pores. However, results obtained using fast neutron activation analyses show that spray atomized and deposited materials exhibit extremely low levels of dissolved gases, suggesting that this mechanism is not as important as originally thought [84]. Furthermore, in view of the irregular morphology of the pores it is highly improbable that a large proportion of the porosity originates from the rejection of entrapped gases, since gas porosity generally exhibits a spheroidal morphology.

The formation of shrinkage porosity is generally associated with sluggish solidification kinetics, such as those present during ingot casting. In view of the limited amount of liquid phase present under proper spray atomization and deposition conditions, it is highly unlikely that solidification shrinkage plays an important role in the formation of the observed pore distribution. It is worth noting, however, that if the spray atomization and deposition conditions are such that there is an excessive amount of liquid phase present at the deposited surface, this mechanism may play a significant role in the formation of porosity. The presence of excess amounts of liquid phase during impact may develop as a result of: (a) coarse droplet sizes, (b) high deposition temperatures, and (c) remelting of solid phases caused by high spray enthalpies [81]. Under these conditions, the atomization gas may interact with the molten metal, leading to the formation of large amount of porosity.

The available experimental evidence suggests that a large proportion of the porosity that is generally observed in spray deposited materials may be attributed to the third mechanism, interpaticle porosity. As the droplets descend, first on the deposition surface, and eventually on each other, they overlap leaving micron-sized cavities in between. In spite of the large amount of turbulence present, the relatively rapid drop in temperature during deposition prevents any liquid phase present from filling all of the cavities, leading to the formation of irregular pores. This mechanism is consistent with the observed correlation between deposition conditions such as spray density, powder size, and fraction solidified, and the amount of porosity present throughout the deposit [84-87]. For example, the higher density associated with the central region of the deposit has been attributed to the elevated mass flux of droplets in this region of the spray, relative to the periphery [88]. These droplets contain elevated fractions of liquid phase, effectively filling the interstices between droplets. In contrast, the high amount of porosity generally observed in the periphery of the spray deposited materials results from a large proportion of small, presolidified droplets.

Numerous investigators have studied the effects of processing parameters on the density of plasma processed materials [26, 31, 89, 90]. For example, Smith and Mutasim [89] studied the concomitant influences of gas flow rate, nozzle type, spray distance and other variables on the density of the deposit. Murakami et al. [91] investigated the effects of substrate cooling on the

formation of porosity. Evidently, the formation of porosity during plasma spraying and deposition is influenced by numerous processing parameters. However, the critical factors that strongly influence the formation of porosity are listed as follows: the particle melting state (or usually known as degree of melting); particle velocity upon impingement with the substrate; particle deformation and solidification. The degree of melting during plasma spraying is primarily associated with the particle-plasma interactions [25, 92], in which the primary factors are energy content of the plasma gas, powder particle feeding velocity and trajectories [93]. During plasma processing, an extremely sharp temperature gradient exists in the plasma jet. For example, the work done by McKellicet et al. [92] has indicated that the temperature field varies from 1000 K to 12,000K in a plasma jet using argon/hydrogen. Therefore, depending on powder type, size, shape and injection velocity, various powder states are produced as the powders travel through this gradient. These include fully molten powders (droplets) and partially molten powders and/or unmelted powders. Consequently, the dispersion of particles contains fully molten, partially molten or unmelted powders during impingement on the deposition surface. Upon impingement with deposition surface, the powders and droplets exhibit different deformation and solidification behavior. As a result, interactions between these powders, between powders and deposition surfaces account for a significant proportion of porosity.

### III. NUMERICAL ANALYSIS OF DROPLET-GAS INTERACTIONS IN SPRAY ATOMIZATION OF TA-2.5W ALLOY

#### 3.1. Model Formation

The droplet dispersion that is present during atomization and deposition is comprised of a distribution of droplets of different sizes. The momentum and heat transfer processes between the atomization gas and droplets may be treated using either an Eulerian or a Lagrangian approach. We employ the Lagrangian approach due to its relative simplicity in numerical calculations. In the 2-D Lagrangian model that will be introduced below, we consider first the 2-D motion, cooling and solidification histories of a single droplet. Then, calculations are carried out for some specific droplet diameters determined by earlier experimental measurements to characterize the entire size distribution of droplets.

##### 3.1.1. 2-D Flow Model

The spatial motion of a droplet during atomization and deposition, not only determines its residence time in the spray cone, but also critically influences its cooling and solidification by changing the surface interaction conditions. Therefore, knowledge of the velocity fields of both the gas and droplets is a precondition of the numerical calculation of droplet temperature and solidification histories. The 2-D motion equations of a single droplet may be derived on the basis of a 2-D force balance on a single sphere in a high speed, axisymmetric gas flow, and may be written in Lagrangian frame as [94, 95]

$$\frac{dv_d}{dt} = g(1 - \frac{\rho_g}{\rho_d}) + \frac{3}{4} \frac{1}{d} \frac{\rho_g}{\rho_d} U_r (v_g - v_d) C_{drag} \quad \text{in axial direction} \quad (1)$$

$$\frac{du_d}{dt} = \frac{3}{4} \frac{1}{d} \frac{\rho_g}{\rho_d} U_r (u_g - u_d) C_{drag} \quad \text{in radial direction} \quad (2)$$

where it has been assumed that

- (a) The concentration of droplets in the atomization gas is sufficiently dilute, so that droplet-droplet interactions may be safely neglected;
- (b) The Basset history term and lift force may be ignored compared to the inertia and the standard drag forces;
- (c) Droplets are spherical and their size remains unchanged during flight, so that the correlation for the drag coefficient of a solid sphere is applicable;

Table 4. Parameters Used in Computations [96-98]

Atomic diameter	$a(m)$	$2.94 \times 10^{-10}$
Avogadro's constant	$N(\text{atoms/mol})$	$6.02 \times 10^{23}$
Boltzmann's constant	$\kappa(J/K)$	$1.38 \times 10^{-23}$
Effective molecular diameter	$d_m(m)$	$2.94 \times 10^{-10}$
Emissivity of surface	$\epsilon_E$	0.5
Equilibrium partition coefficient	$k_e$	2
Gas constant	$R(J/K \text{ mol})$	8.319
Gas temperature	$T_g(K)$	220
Geometrical parameter in Eq. (3)	$z_l(m)$	0.02
Geometrical parameter in Eq. (3)	$z_s(m)$	0.17
Geometrical parameter in Eqs. (4)-(5)	$C$	0.268
Geometrical parameter in Eqs. (4)-(5)	$D(m)$	0.004
Initial axial velocity of droplet	$v_{d0}(m/s)$	2
Initial axial velocity of gas	$v_{g0}(m/s)$	520
Initial droplet temperature	$T_{d0}(K)$	3750
Liquidus temperature	$T_l(K)$	3306
Mechanical equivalent of heat	$J(m \text{ kg/J})$	0.102
Molar volume of melt	$V_m(m^3/mol)$	$1.086 \times 10^{-5}$
Self-diffusivity in melt	$D_{lm}(m^2/s)$	$3.335 \times 10^{-9}$
Solid/liquid interfacial energy	$\sigma_m(J/m^2)$	0.322
Solidus temperature	$T_s(K)$	3299
Solvent melting temperature	$T_m(K)$	3293
Specific heat ratio of gas	$\gamma$	1.4
Stephen-Boltzmann's constant	$\sigma(W/m^2 K^4)$	$5.677 \times 10^{-8}$

- (d) The flow of the atomization gas is axisymmetric, hence droplets neither rotate nor move in the angular direction of the spray cone so that the motion of droplets may be considered to be 2-dimensional (in the axial and radial directions of the spray cone).

The gas velocity distribution that is necessary for the solution of Eqs. (1) - (2) can be determined using the data measured by Bewlay et al. [99, 100]. Based on their experiments, which were conducted with an atomizer similar to the one used in our experiments, the decay in the mean axial gas velocity at the center line of the spray cone satisfies an exponential relationship of the following type [97],

$$v_g(0, z) = v_{g0} \exp\left(-\frac{z - z_i}{z_s - z_i}\right) \quad (3)$$

The gas exit velocity,  $v_{g0}$ , and the constants,  $z_i$  and  $z_s$ , as listed in Table 4, are related to atomizer geometry and atomization parameters and have been determined and discussed elsewhere [97].

On the basis of our experimental observations and the experimental results of Bewlay et al. [99, 100], the radial distribution of the axial and radial gas velocities may be formulated as

$$\frac{v_g(r, z)}{v_g(0, z)} = \left[1 - \left(\frac{r}{D + Cz}\right)^{1.5}\right]^2 \quad (4)$$

$$u_g(r, z) = v_g(r, z) \left[\frac{r}{D/C + z}\right] \quad (5)$$

under the axisymmetric assumption. In Eqs. (4) - (5), the constants D and C are related to atomizer geometry and atomization parameters and have been determined experimentally, as listed in Table 4.

It should be indicated that under our experimental conditions, the gas exits the atomizer nozzle at supersonic velocity [97]. The gas expands and accelerates within the distance  $z_i$  and then decays through shocks and diffusion to subsonic speed in a non-uniform "roller-coaster" fashion. Hence, the compressibility of the gas may significantly influence the transfer processes between the gas and droplets. However, the dependence of the drag coefficient,  $C_{drag}$ , on the Mach number seems to be negligibly small in our Reynolds number regime according to Schlichting [101]. Hence,  $C_{drag}$  is expressed here only as a function of Re using an improved approximation [102] for the standard drag curve

$$C_{drag} = \begin{cases} 24/Re, & 0 < Re < 1 \\ 24/Re^{0.646}, & 1 < Re < 400 \\ 0.5, & 400 < Re < 3 \times 10^5 \\ 3.66 \times 10^{-4} Re^{0.428}, & 3 \times 10^5 < Re < 2 \times 10^6 \\ 0.18, & 2 \times 10^6 < Re \end{cases} \quad (6)$$

Table 5. Physical Properties of Alloy Used in Computations [98, 103]

	Ta-2.5 wt.%W (l)	Ta-2.5 wt.%W (s)
$c_{pd}$ (J/kg K)	244	234
$\rho_d$ (kg/m <sup>3</sup> )	14862	15000
$\Delta H_m$ (J/kg)	171400	

The 2-D velocity distributions of the droplets and gas in the spray cone can be then calculated using Eqs. (1) - (6), once the droplet size and the properties of the droplets and gas have been established. Eqs. (1) - (2), along with Eqs. (3) - (6) and the parameters listed in Tables 4-6, were solved using a 4th-order Runge-Kutta-algorithm.

### 3.1.2. Lumped Parameter Formulation

In atomization and deposition of a Ta-2.5W alloy with N<sub>2</sub> atomization gas, a droplet undergoing cooling and phase change may experience three states: (a) fully liquid, (b) mushy, and (c) fully solid. In all three states, the Bi number calculated under our experimental conditions is smaller than 0.1. Thus, the lumped parameter formulation used in previous studies [97, 105-107] can be employed for the droplet temperature calculation.

During the flight of droplets in the spray cone, the forced convective and radiative heat

Table 6. Physical Properties of N<sub>2</sub> Atomization Gas Used in Computations [104].

$c_{pg}$	(J/kg K)	$c_{pg} = 1021.290 + 0.135T' - 1.794 \times 10^6/T'^2$
$K_g$	(W/m K)	$K_g = K_{g0}(\frac{T'}{273})^n$
$\rho_g$	(kg/m <sup>3</sup> )	$\rho_g = \frac{273 \rho_{g0}}{T'}$
$\mu_g$	(kg/m s)	$\mu_g = \mu_{g0}(\frac{273+c}{T'+c})(\frac{T'}{273})^{1.5}$
$K_{g0}$	(W/m K)	$2.401 \times 10^{-2}$
n		0.8
$\rho_{g0}$	(kg/m <sup>3</sup> )	1.250
$\mu_{g0}$	(kg/m s)	$1.658 \times 10^{-5}$
c		118
$r_e$		0.770
$v_s$	(m/s)	302.396
Ma		0.893
R	(m <sup>2</sup> /s <sup>2</sup> K)	296.893

exchange with the atomization gas leads to a rapid heat extraction from the droplets. On the other hand, the frictional heat produced by the violent interactions between the gas and droplets reduces the heat extraction rate. This effect becomes important in a supersonic atomization gas where the compressibility of the gas is significant [108]. Hence, the transient temperature of a single droplet during flight in the high speed atomization gas is calculated using the modified Newton's law of cooling [108]

$$\frac{dT_d}{dt} = - \frac{6}{d\rho_d c_{pd}} \left[ h(T_d - T_g) - r_e \frac{u_0^2}{2gJc_{pg}} + \sigma\epsilon_E (T_d^4 - T_g^4) \right] \quad (7)$$

with

$$c_{pd} = \begin{cases} c_{pl} & \text{fully liquid} \\ c_{pl} - \Delta H_m \frac{df_s}{dT_d} & \text{mushy} \\ c_{ps} & \text{fully solid} \end{cases} \quad (8)$$

where the term,  $r_e \frac{u_0^2}{2gJc_{pg}}$ , in Eq. (7) represents the effect of the frictional heat on the droplet temperature. The recovery factor,  $r_e$ , as a function of the Mach number is approximated according to experimental results in [108].

In a supersonic gas flow, the convective heat-transfer coefficient,  $h$ , is not only a function of the Reynolds number and the Prandtl number, but also depends on the droplet surface temperature and the Mach number [108]. However, the effects of the surface temperature and the Mach number may be substantially eliminated if all properties are evaluated at a film temperature,  $T'$ , defined by [108]

$$\frac{T'}{T_g} = 1 + 0.032 Ma^2 + 0.58 \left( \frac{T_d}{T_g} - 1 \right) \quad (9)$$

Thus,  $h$  may still be estimated using the experimental correlation proposed by Ranz and Marshall [109]

$$h = \frac{K_g}{d} \left( 2 + 0.6 Re^{\frac{1}{2}} Pr^{\frac{1}{3}} \right), \quad 1 < Re < 70000 \quad (10)$$

It should be indicated that a discrepancy between modeling and experimental results has been found and reported in [97] when modeling was conducted using Newton's law of cooling and the convective heat-transfer coefficient was calculated directly using the Ranz and Marshall correlation. In that particular study [97], the discrepancy was eliminated by modifying the heat-transfer coefficient on the basis of the individual experimental data, hence limiting generalization of the method and results. In the present work, however, a good agreement between the modeling and experimental results can be ensured through employing the modified Newton's law of cooling and through calculating the heat-transfer coefficient at the film temperature. Hence, such treatment may obtain more wide application in the numerical simulation of droplet cooling and solidification histories during supersonic atomization.

### 3.1.3. Rapid Solidification of Droplets

For the purpose of analysis, the thermal history of atomized droplets in the spray cone can be divided into four regions: a) rapid cooling in the fully liquid state, b) nucleation and recalescence, c) post-recalescence solidification, and d) cooling in the fully solid state. The thermal histories in regions a) and d) can be described directly using Eqs. (7) and (8). The nucleation temperature (hence the achievable undercooling) and the solid fraction evolution during recalescence and post-recalescence solidification must be determined additionally.

In atomization and deposition, a large undercooling may generally be attained prior to the onset of nucleation. An upper bound of the degree of undercooling may be estimated using Hirth's formulation [110] for homogeneous nucleation within a droplet

$$\frac{0.01I \frac{1}{6} \pi d^3 \Delta T}{\dot{T}} = 1 \quad (11)$$

The homogeneous nucleation rate,  $I$ , may be calculated using [111]

$$I = \frac{N}{M} \rho_d \frac{D_{lm}}{a^2} \exp \left[ - \frac{16}{3} \pi \frac{V_m^2 T_1^2 \sigma_m^3}{\kappa T_d \Delta T^2 \Delta H_m^2} \right] \quad (12)$$

It should be indicated that in Eq. (12), the dependence of the free-energy change on undercooling has been formulated according to the work of Turnbull et. al. [112] in order to maintain the problem tractable, although an improved correlation [113] has recently been reported.

In view of the high probability of heterogeneous nucleation associated with the conditions that are present in atomization and deposition processes, the undercooling calculated with Eqs. (11) - (12) must be modified by a factor, depending on droplet size. This factor has been derived in Ref. [97] based on microstructural observations of the atomized powders. In the present work, we estimate the degree of undercooling for heterogeneous nucleation using the method suggested in Ref. [97].

Following nucleation, the release of the latent heat of fusion generally occurs at a rate that is substantially higher than that of convective and radiative heat dissipation at the droplet surface, leading to an overall temperature rise in the droplet, i.e., recalescence. The extent of the temperature rise during recalescence depends basically on undercooling and cooling rate, and can be described by Eq. (7), ignoring the surface heat extraction [114]

$$\frac{dT_d}{dt} = \frac{\Delta H_m}{c_{pl}} \frac{df_s}{dt} \quad (13)$$

The solid/liquid interface velocity during recalescence is also a function of undercooling and cooling rate. Different expressions for the interface velocity have been employed in previous studies [107, 114-117], including the linear and exponential laws for planar continuous growth at small and large undercoolings, respectively [107, 114-117], the Ivantsov equation for growth of paraboloid dendrites [105], as well as the power law for dendrite growth [118]. In view of the ability of power laws with different power indices to describe different growth mechanisms, we employ the power law to estimate the growth velocity of dendrites into undercooled melt. Accordingly, the solid fraction evolution during recalescence is calculated using the following expression [107], ignoring the errors induced by higher order  $dt$

$$\frac{df_s}{dt} = \frac{6K_m \Delta T^m}{d} \quad (14)$$

where  $K_m$  and  $m$  are related to the relevant droplet properties, cooling conditions and growth mechanisms, and should be experimentally determined. In this study, we estimate  $K_m$  using [115, 117]

$$K_m = \frac{D_{lm} \Delta H_m}{d_m R T_1^2} \quad (15)$$

and select  $m$  as unity on the basis of the analyses in [118]. Although it appears that there is no difference between the interface velocity expression in Eq. (14) (for  $m = 1$ ) and the linear law, it should be noted that the linear law is valid only for planar continuous growth at small undercoolings. Our experimental data [97] suggest that the undercoolings experienced by droplets during spray atomization are large, and the most likely growth mechanism is dendrite growth. Hence, we refer to the interface velocity expression in Eq. (14) as a power law, as defined in [118].

The limit of the droplet temperature rise during recalescence is the liquidus temperature. The maximum solid fraction during recalescence,  $s$ , may be calculated using the following relationship [97]

$$s = (T_l - T_n) \frac{c_{pl}}{\Delta H_m} \quad (16)$$

As recalescence proceeds, the interface velocity and hence the release rate of the latent heat of fusion decrease. When the latter equals the rate of heat extraction at the droplet surface, or the solid fraction during recalescence attains the maximum  $s$ , whichever occurs first, recalescence terminates.

Following recalescence, the interface velocity decreases to a relatively steady value. Further solidification of the droplet in the mushy zone, referred to as post-recalescence solidification, is dictated by the Scheil equation [114, 119]

$$\frac{df_s}{dT_d} = \frac{1-s}{(k_e - 1)(T_m - T_l)} \left( \frac{T_m - T_d}{T_m - T_l} \right)^{(2-k_e)/(k_e-1)} \quad (17)$$

Using Eqs. (7) - (15), and (17), along with the related parameters given in Tables 4-5, the 2-D distributions of transient droplet temperature, cooling rate, solid fraction, and achievable undercooling in the spray cone can be calculated, once the droplet size, velocity and trajectory have been established. Eqs. (7), (13), (14) and (17) were solved using a finite difference method with a time-step of  $10^{-8}$  second. During the calculations, the gas temperature is assumed to be constant due to the large mass flow rate of the gas under the present conditions. All computations were completed on a DEC 3000/400 AXP workstation.

### 3.2. Results and Discussion

The numerical model described above is used to compute 2-D velocity, temperature, cooling and solidification histories of Ta-2.5W droplets in N<sub>2</sub> atomization gas. Five specific droplet diameters: 10, 30, 60, 100 and 200  $\mu\text{m}$  are selected to characterize the entire size distribution of droplets. Moreover, it is assumed that molten Ta-2.5W at a superheat temperature of 3750 K and an initial velocity of 2 m/s is atomized by relatively cool (220 K) N<sub>2</sub> gas. The physical properties of Ta-2.5W and N<sub>2</sub> gas used in the computations, along with other relevant parameters, are summarized in Tables 4-5. In the following sections, we present and discuss the numerical results.

#### 3.2.1. Velocity Evolution and 2-D Distribution of Atomization Gas and Droplets In Spray Cone

The velocity vectors of the atomization gas in the spray cone are summarized in Figure 2. It can be seen that the axial gas velocity on the axis line decays rapidly with increasing distance in the axial direction. At the same time, the gas spreads and mixes with the surrounding environment, leading to an increase in the gas flow diameter. The radial profiles of axial gas velocities exhibit a shape that is akin to a Gaussian probability distribution. The gas flow is predominantly in the axial direction as a result of the axisymmetric assumption. These results are in qualitative agreement with the features of the LDA measurements of the gas velocities reported in [99, 100].

Figure 3 shows the velocity vectors of the droplets of 60  $\mu\text{m}$  diameter in the spray cone. Initially, both the axial and radial droplet velocities increase along the axial direction and attain rapidly their maximum values. At the same time, the radial profiles of axial droplet velocities approach rapidly a shape that is analogous to that of the axial gas velocity at the axial distance of approximately 0.2 m. With increasing axial distance, the radial profiles become wider. Moreover, at any axial distance, the droplet velocity at the spray axis is larger than at the periphery of the spray cone. Hence, the flight time required to reach a given axial distance is shorter at the spray axis than at the periphery of the spray cone. The computed profiles are in qualitative agreement with the deposit contours obtained in related experiments [105, 120].

Figure 4 shows the axial velocity evolution of the atomization gas and droplets of different diameters along the axis line of the spray cone. The gas velocity remains constant within the distance  $z_i$  and then decays exponentially in the axial direction. Each droplet is accelerated to its maximum velocity at the flight distance where the relative velocity between the droplet and gas is zero. Beyond this point, the droplet is decelerated. However, due to the large density of the material considered (Table 5), the deceleration of larger droplets (for example, d=60, 100 and 200  $\mu\text{m}$ ) is small, leading to a nearly constant velocity during further flight. The flight distance

required to attain the maximum velocity decreases with decreasing droplet size. A small droplet generally has a large acceleration and a high velocity. Hence the flight time that is required for any given flight distance decreases with decreasing droplet size. However, there is an exception with the droplets of 10  $\mu\text{m}$  diameter, as evident from the figure. These droplets follow closely the gas flow due to their small inertia. Consequently, the flight time is shorter for these droplets in the region close to the atomizer and turns to longer in the region far from the atomizer. For example, the flight time to a distance of 600 mm at the spray axis is 5.1, 4.4, 5.5, 6.6, and 8.8 ms for 10, 30, 60, 100, and 200  $\mu\text{m}$  droplets, respectively. Similar behavior has also been reported in earlier studies [105, 114].

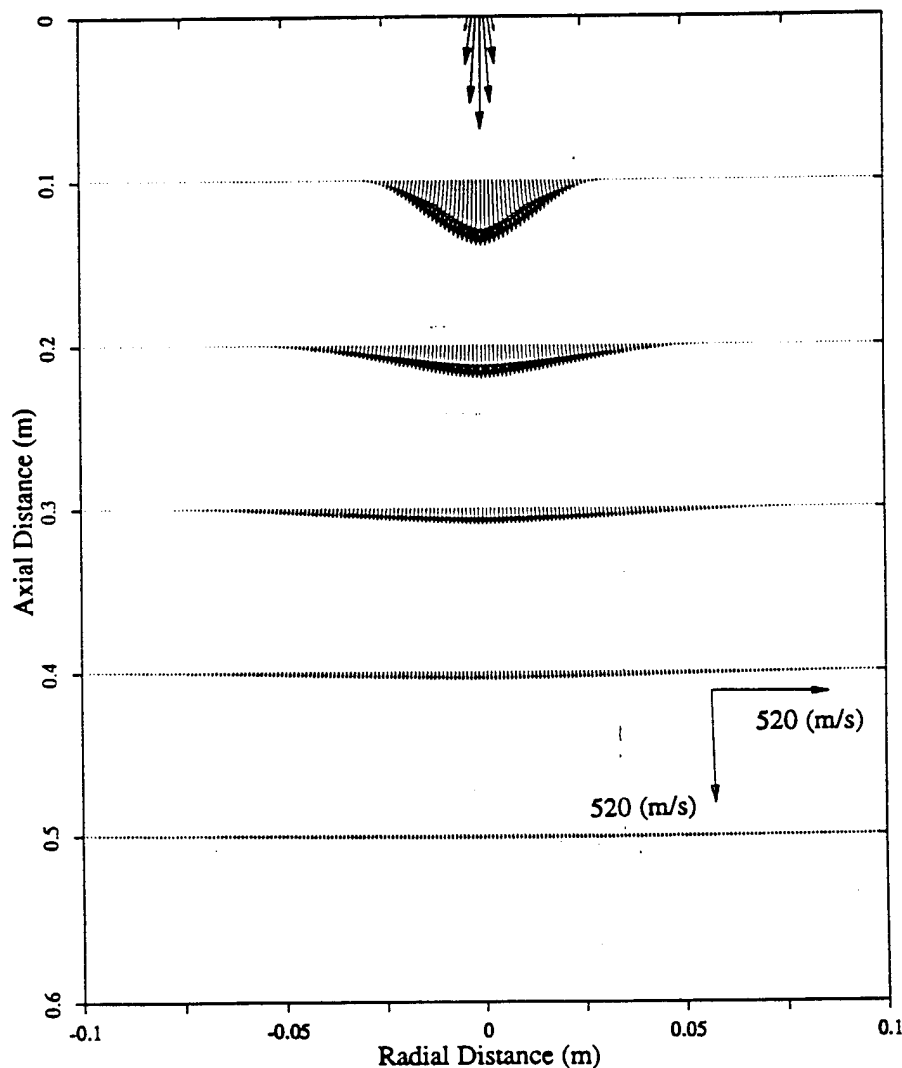


Figure 2. Velocity field of the atomization gas in the spray cone.

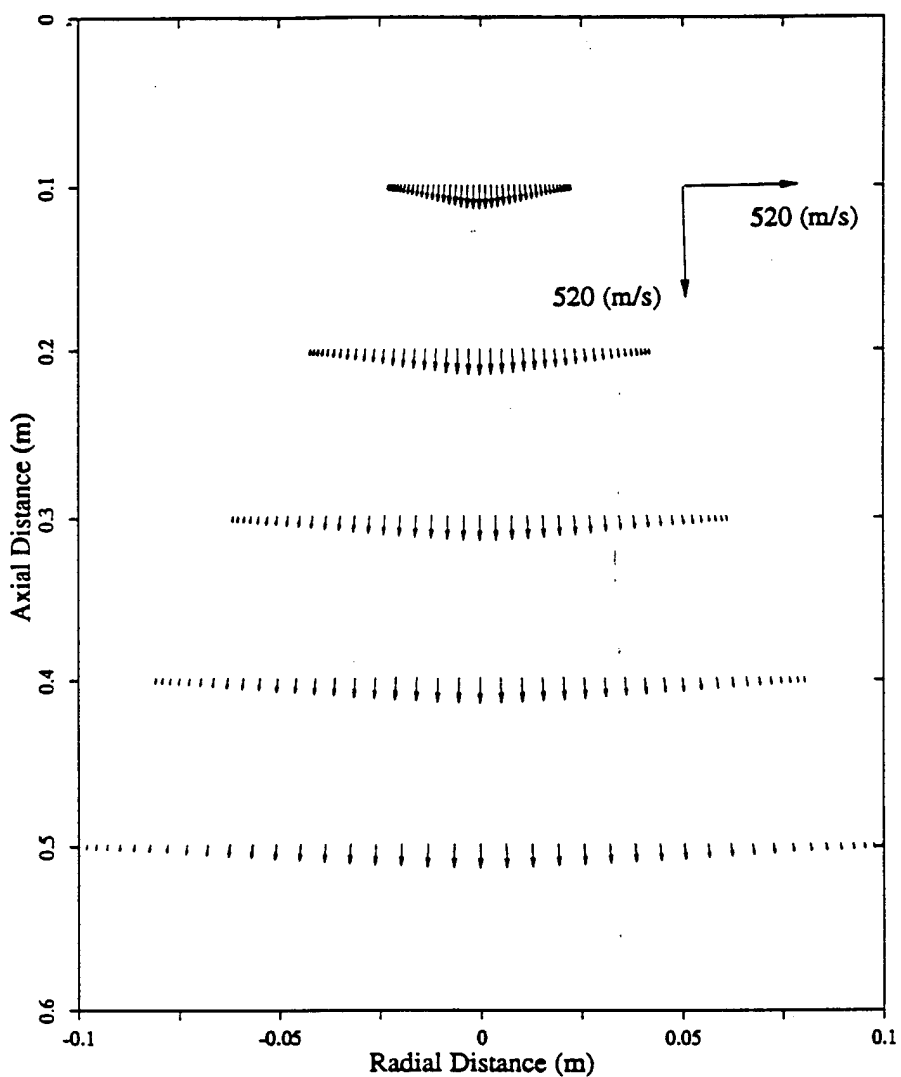


Figure 3. Velocity field of the droplets of  $60 \mu\text{m}$  diameter in the spray cone.

Figure 5 shows the radial distributions of the axial velocities of the atomization gas and droplets of different diameters in the spray cone. Clearly, small droplets exhibit larger axial velocities at any radial distance. Small droplets also have a wider radial distribution at any axial distance (for example,  $z=30, 60$  and  $90 \text{ mm}$ ). This suggests that a larger population of small droplets impinge on the surface in the periphery region of the sprayed deposit. This suggestion is verified by an experimental study of particle size distributions [121] which demonstrated that the oversprayed particles collected during atomization and deposition exhibit a smaller median size than the average size of powders generated and acquired during atomization. The experimental

observation of small median particle diameters and a narrow size distribution of oversprayed powders indicates that the coarse droplets generally form the core whereas the periphery of the spray cone is populated by fine droplets [121]. In another analysis of the spray deposition process [105], the experimental results also revealed that the mass-median droplet diameter decreases along the radial direction from the spray axis. These phenomena may be attributed to the fact that small droplets have small inertia and hence can be easily dragged and accelerated by the atomization gas in both the axial and radial directions. The good agreement between the numerically predicted and the experimentally determined tendency supports the model formulation described herein.

### 3.2.2. Temperature, Cooling and Solidification Histories of Droplets In Spray Cone

Figures 6, 7 and 8 show the temperature, cooling and solidification histories of droplets of different diameters along the axis line of the spray cone, respectively. From Figure 6 it can be seen that the droplet temperature rapidly decreases to the nucleation temperature within a short flight distance of approximately 1, 13, 41, 63 and 121 mm for 10, 30, 60, 100 and 200  $\mu\text{m}$  droplets, respectively. The achievable undercooling is calculated to be 699, 633, 476, 241 and 44 K for 10, 30, 60, 100 and 200  $\mu\text{m}$  droplets, respectively. The corresponding values of  $\Delta T/T_1$  are 0.21, 0.19, 0.14, 0.07 and 0.01, respectively, which are within the range observed experimentally for a number of materials [122]. Although the amount of the achievable undercooling was not measured for tantalum, it was believed to be high [122].

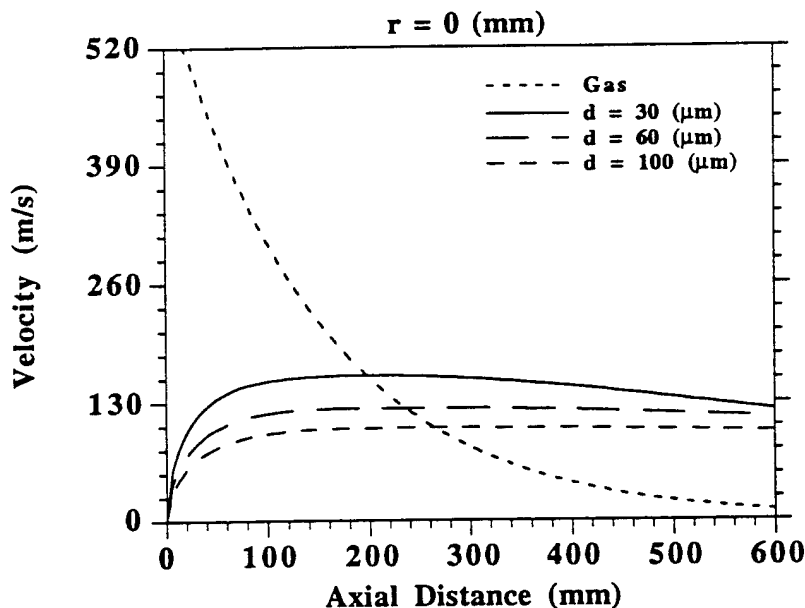


Figure 4. Axial velocity evolution of the atomization gas and droplets along the axis line of the spray cone.

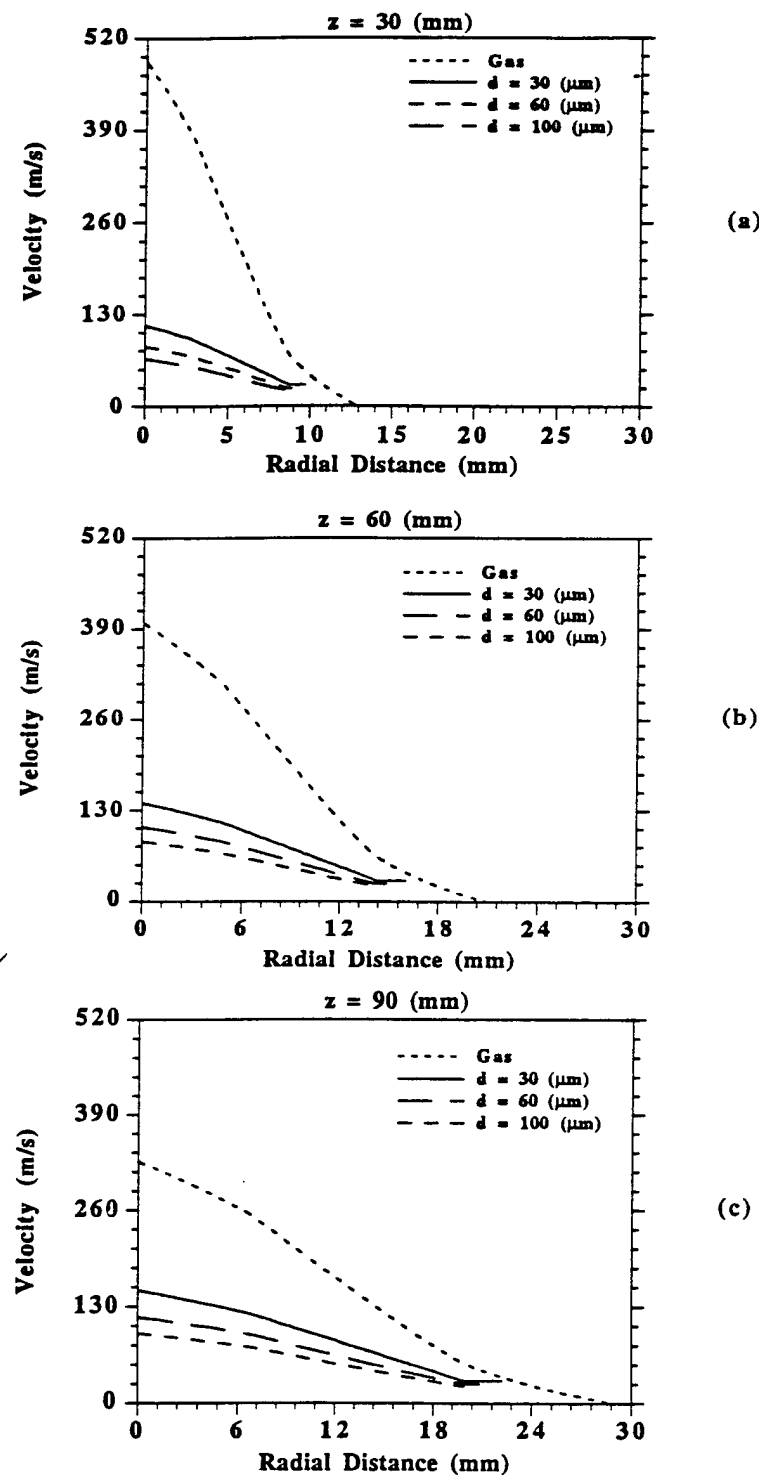


Figure 5. Axial velocity distributions of the atomization gas and droplets in the radial direction of the spray cone.

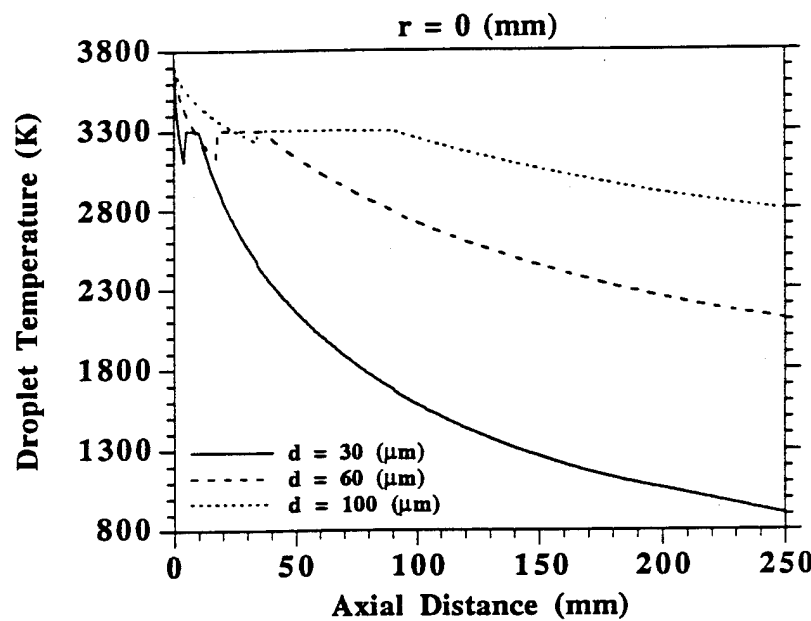


Figure 6. Temperature histories of droplets along the axis line of the spray cone.

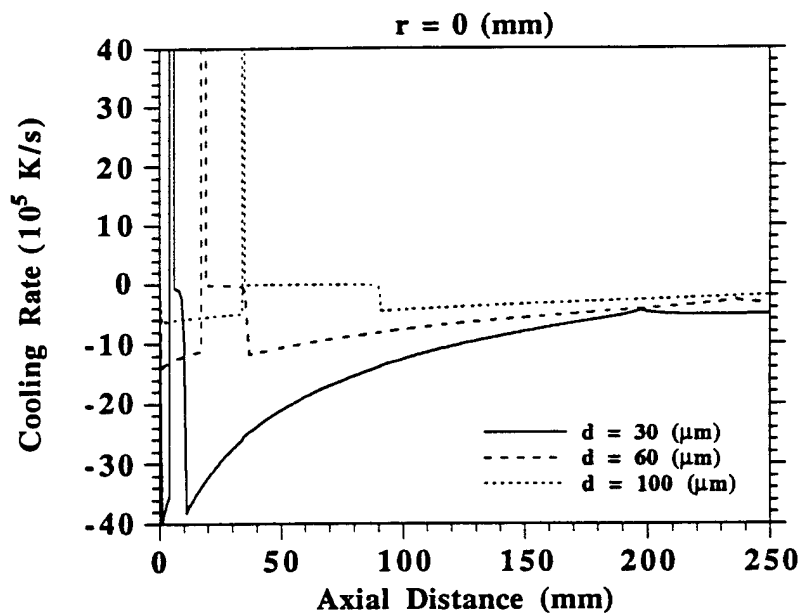


Figure 7. Cooling histories of droplets along the axis line of the spray cone.

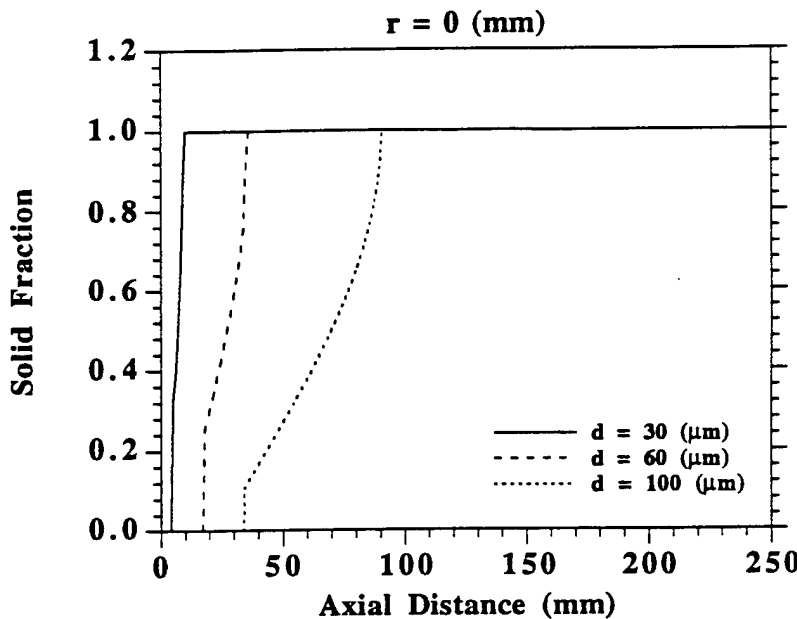


Figure 8. Solidification histories of droplets along the axis line of the spray cone.

From Figure 7 it can be seen that the cooling rate experienced by each droplet attains a maximum value initially (corresponding to the negative side in Figure 7) on the order of  $10^5 - 10^6$  K/s for the droplets larger than 30  $\mu\text{m}$ , and  $10^7$  K/s in magnitude for 10  $\mu\text{m}$  droplets. The cooling rate then decreases continuously along the axial direction until the onset of solidification. Following nucleation, the latent heat of fusion is released at a rate that is substantially higher (positive side in Figure 7) than the convective heat extraction rate at the droplet surface due to the large undercooling, leading to recalescence. During recalescence, the droplet temperature rises up to the equilibrium liquidus temperature (Figure 6) and the solid fraction increases rapidly (Figure 8). For example, a dominant amount of solid forms during recalescence in the 10 and 30  $\mu\text{m}$  droplets ( $f_s = 0.99$  and 0.90, respectively), while the solid fraction in the 60, 100 and 200  $\mu\text{m}$  droplets increases to 0.68, 0.34 and 0.06 during recalescence, respectively. Apparently, the solid formed during recalescence is critically dependent on undercooling. The supercooling may be expected if the droplet diameter is smaller than 10  $\mu\text{m}$ .

At the end of recalescence, the cooling rate of each droplet changes from positive (heating) to negative (cooling) (Figure 7) and then exhibits a small, progressive increase during post-recalescence solidification occurring at a cooling rate of approximately  $10^3 - 10^5$  K/s in magnitude for the droplets larger than 30  $\mu\text{m}$ , and  $10^6$  K/s in magnitude for 10  $\mu\text{m}$  droplets (Figure 7).

During post-recalcescence solidification, the temperature of each droplet decreases slowly from the liquidus to the solidus temperature (Figure 6) and the solid fraction increases progressively (Figure 8). At the end of post-recalcescence solidification, there is a sharp increase in cooling rate due to the termination of the release of the latent heat of fusion (Figure 7). The cooling rate then turns to decrease with decreasing temperature- and velocity-difference between the atomization gas and droplets.

Solidification is completed at a flight distance of approximately 2, 18, 70, 138 and 305 mm, corresponding to a total solidification time of approximately 0.04, 0.25, 0.72, 1.30 and 2.71 ms for 10, 30, 60, 100 and 200  $\mu\text{m}$  droplets, respectively (Figure 8). At an axial distance of 100 mm, the droplet temperature is approximately 290, 1797 and 3034 K for 10, 30 and 60  $\mu\text{m}$  droplets, and the temperature of a 100 and 200  $\mu\text{m}$  droplet remains close to the solidus and liquidus temperatures, respectively (Figure 6). At an axial distance of 600 mm, the droplet temperature is calculated to be 220, 324, 1286, 2187 and 2940 K for 10, 30, 60, 100 and 200  $\mu\text{m}$  droplets, respectively.

The effect of the droplet size on the temperature, cooling and solidification histories is evident from Figures 6, 7 and 8. Overall, small droplets exhibit high cooling rate, large undercooling, short solidification time and low temperature. These phenomena result from the high convective heat transfer rate between small droplets and the atomization gas. As the flight distance increases, the cooling rate of small droplets decreases rapidly due to the decreasing relative velocity and temperature.

### 3.2.3. 2-D Distribution of Temperature, Cooling Rate and Solid Fraction of Droplets In Spray Cone

Figures 9, 10 and 11 show the distributions of the temperature, cooling rate and solid fraction of droplets of different diameters in the radial direction of the spray cone. As demonstrated in Figures 9 and 10, at most axial distances (where droplets are in a single phase state: fully liquid or fully solid), the droplet temperature and cooling rate attain their maximum values at the spray axis and decrease to minimum values at the periphery of the spray cone. There are some exceptions, for example, at  $z=30$  mm, Figure 9(a). At this axial distance, the 60 and 100  $\mu\text{m}$  droplets experience solidification at some radial distance between 2 and 8 mm, and solidification is completed at the periphery of the spray cone, while at the spray axis solidification has not begun yet (Figure 11(a)). Therefore, the temperature maximums of the 60 and 100  $\mu\text{m}$  droplets are not at the spray axis, but instead at the radial locations where solidification takes place. From the same reason, the temperature of the 60  $\mu\text{m}$  droplet is higher at the spray axis than that of the 100  $\mu\text{m}$  droplet (Figure 9b). This tendency is also reflected in the distributions of cooling rates. It can be seen that the cooling rate of a droplet is relatively low at the radial location where post-recalcescence

solidification is occurring (compare Figure 10 to Figure 11), and even positive (heating) at the radial location where recalescence is taking place (Figure 10b). In contrast to the radial distributions of the temperature and cooling rate, the radial distributions of the solid fraction exhibit a distinct tendency, i.e. a maximum at the periphery and a minimum at the spray axis (Figure 11). This implies that at a given axial distance, the droplets in the periphery will solidify earlier than those at the spray axis. These phenomena may be rationalized as follows.

As illustrated in Figure 5, the velocity difference between droplets and the atomization gas is much larger at the spray axis than at the periphery of the spray cone, leading to a much higher convective heat transfer rate and hence the much larger cooling rate. In addition, the relatively low droplet velocities at the periphery of the spray cone correspond to relatively long flight time to a given axial distance, as discussed in the previous section. The long flight time of droplets at the periphery of the spray cone causes the lower droplet temperature and the higher solid fraction at the periphery for a given axial distance.

Experimental support to these numerical results may be found in an earlier microstructural investigation of spray deposited materials at different radial positions [120] in which thick prior-droplet-boundaries (more porosity and less droplet deformation) were observed in the fringe region of the deposits. Moreover, our calculations demonstrate that for a given droplet diameter, the achievable undercooling decreases and the solidification time increases with increasing radial distance. These results may be explained similarly on the basis of the droplet velocity and cooling rate distributions in the radial direction.

The results summarized in Figures 9, 10 and 11 also show that with increasing axial distance, for example from  $z=30, 60$  to  $90$  mm, the radial distributions of the droplet temperature, cooling rate and solid fraction become wider and the difference between the spray axis and the periphery of the spray cone decreases. In addition, the effect of the droplet size on the radial distributions is also apparent from Figures 9, 10 and 11. A small droplet has a low temperature, a high cooling rate and a large solid fraction at any radial distance, the exception being at the fringe of the spray cone (Figure 10), where the cooling rate of a small droplet is low due to the small relative velocity between the droplet and the atomization gas (see Figure 5). The larger the droplet, the smaller the difference in the droplet temperature and cooling rate between the spray axis and the fringe of the spray cone, hence the more even the distributions are. The only exception is for the  $10\ \mu\text{m}$  droplets, as discussed above in the velocity distribution.

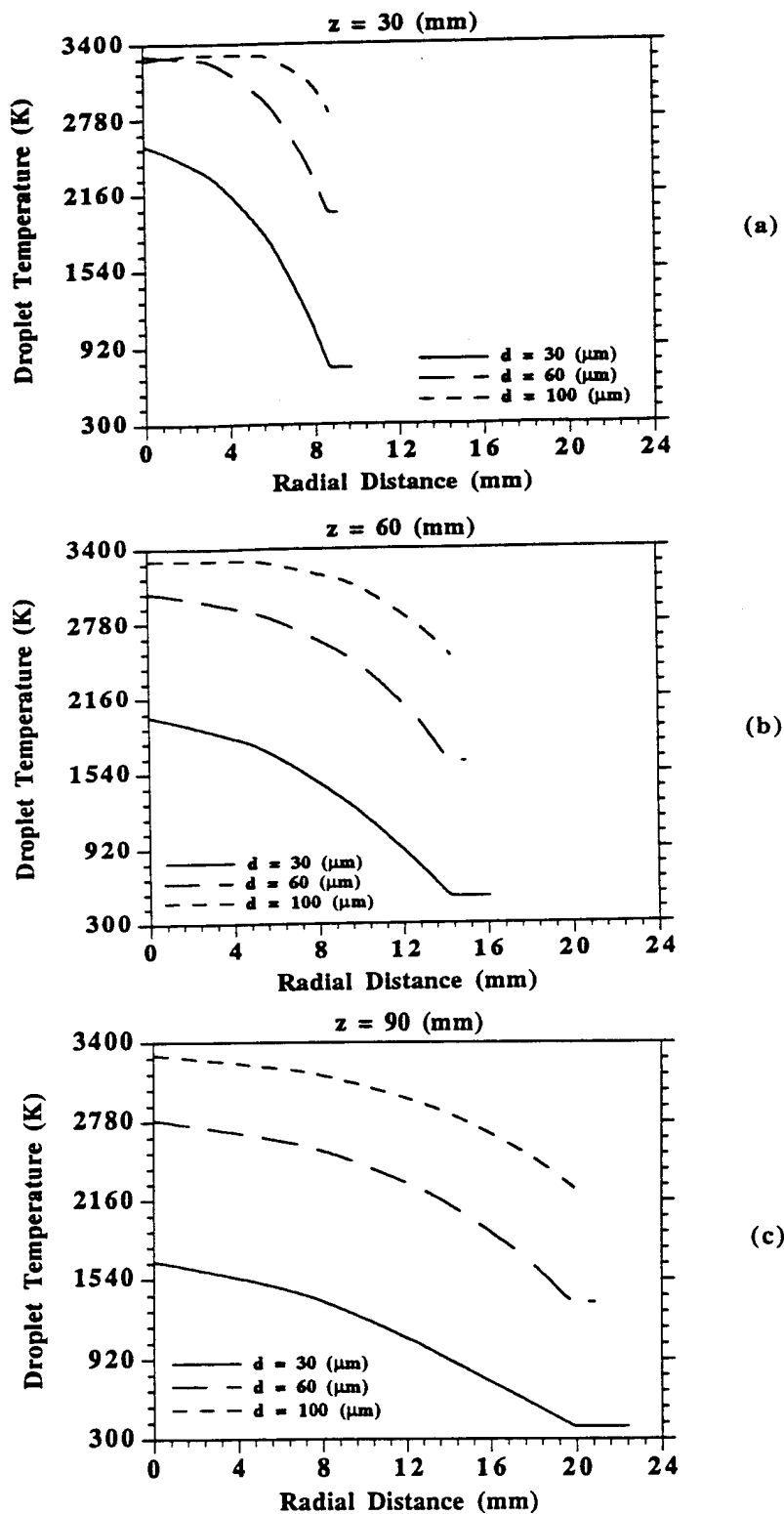


Figure 9. Temperature distributions of droplets in the radial direction of the spray cone.

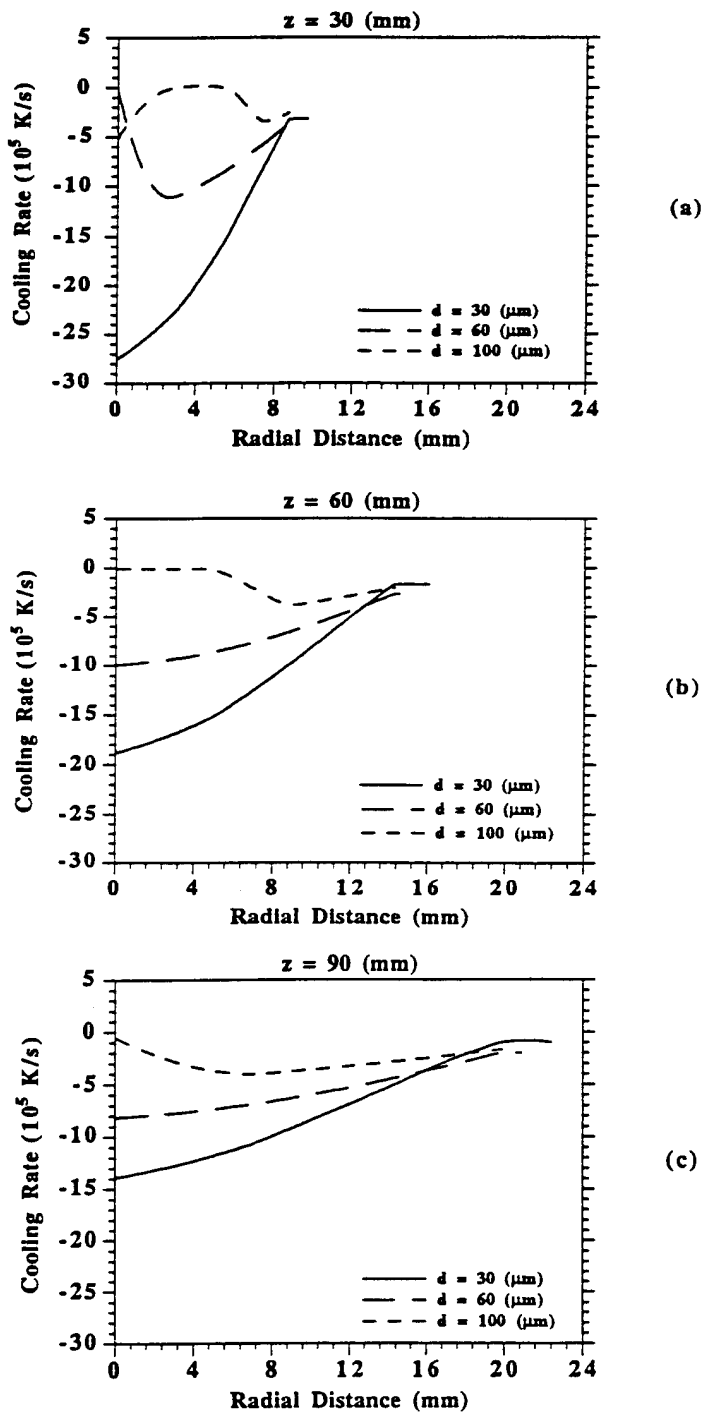


Figure 10. Cooling rate distributions of droplets in the radial direction of the spray cone.

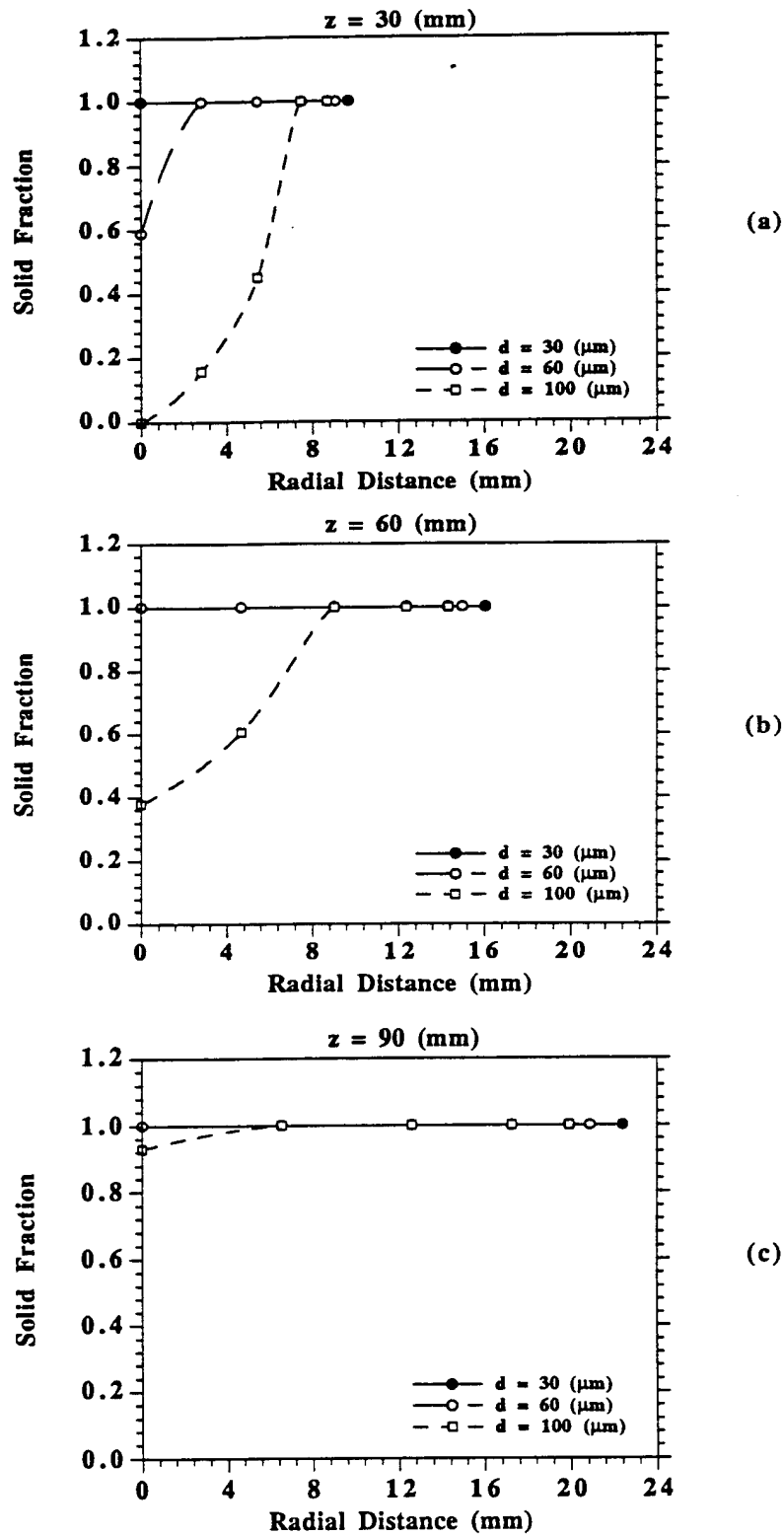


Figure 11. Solid fraction distributions of droplets in the radial direction of the spray cone.

### 3.2.4. Microstructural Characteristics of Particles and Sprayed Materials

In gas atomization, solidification process is typified by the formation of a fine dendritic microstructure in atomized powders. The secondary dendrite arm spacing (SDAS) depends critically on the cooling rate during post-recrystallization solidification [123]. Refinement of dendritic structure by increasing the rate of heat extraction during solidification has become the most important advantage of atomization and deposition processes.

As mentioned above, post-recrystallization solidification takes place at a cooling rate of  $10^3$  -  $10^6$  K/s in magnitude, depending on droplet size and processing conditions. In order to quantitatively determine the effect of the droplet size on the SDAS, the cooling rates of droplets during post-recrystallization solidification are calculated and summarized in Figure 12 as a function of droplet diameter. The corresponding values of the SDAS are also plotted in Figure 12. The SDAS is estimated using the following relationship [123]

$$\text{SDAS} = 39.8 \cdot \dot{T}^{-0.3} \quad (18)$$

As expected, the cooling rate decreases drastically with increasing droplet diameter (from  $8.8 \times 10^6$ ,  $2.8 \times 10^5$ ,  $5.3 \times 10^4$ ,  $1.7 \times 10^4$  to  $5.5 \times 10^3$  K/s when increasing the diameter from 10, 30, 60, 100 to 200  $\mu\text{m}$ ). Correspondingly, the SDAS increases from 0.33, 0.92, 1.53, 2.13 to 3.00

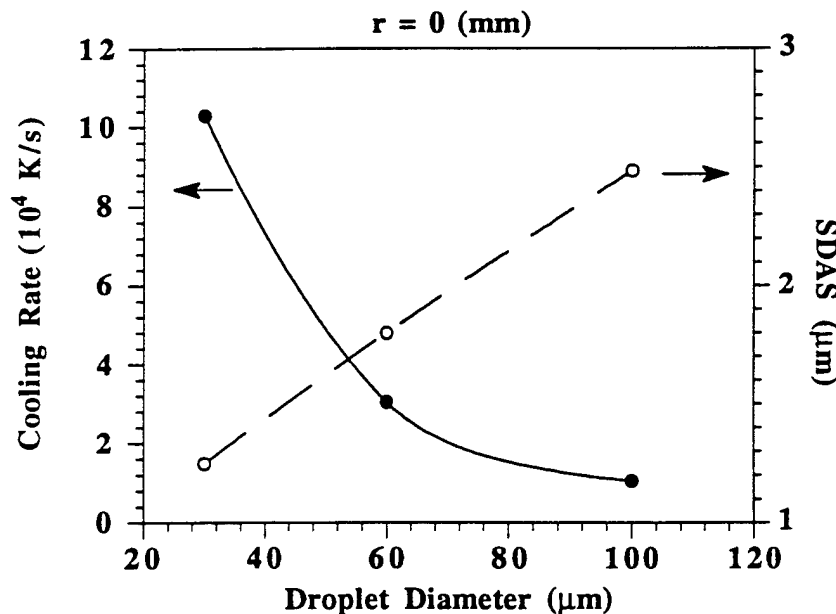


Figure 12. Second dendrite arm spacing and cooling rate during post-recrystallization solidification as a function of droplet diameter.

µm. Since more small droplets impact on the fringe region of the sprayed deposit and a small droplet exhibits a high cooling rate and a fine SDAS (as shown in Figure 12), it may be predicted that the microstructure is fine in the fringe region of the spray deposited material. This tendency is in good, qualitative agreement with the findings of the microstructural characterization studies of spray deposited materials [120, 121] in which a distribution of the microstructural characteristics in the radial direction of the spray cone was found and finer grain size was observed in the edges of the deposits.

## IV. LOW PRESSURE PLASMA SPRAYING OF TUNGSTEN

### 4.1. Experimental Procedures

The plasma spraying of W was conducted at Electro-Plasma Inc. (Irvine, CA) using an EPI-LPPS™ system and EPI-03CP plasma gun. Two specimens (A and B) were prepared with different experimental procedures described as follows. For specimen A, the substrate used was graphite. During processing, a thin Mo coating (of thickness about 0.2 mm) was initially plasma-sprayed on a cylindrical graphite substrate, the reason for which is to prevent the interaction between W and graphite substrate. Pure W powders (purity ~99.9% and size -45+15 µm) were then plasma sprayed and deposited on the Mo coated graphite substrate. The cylindrical shaped deposit was approximately 4 mm in thickness. The substrate was heated to a temperature of 1500°C prior to and following plasma spraying. For specimen B, a molybdenum plate was used. Pure W powders (purity ~99.9% and size -45+10 µm) were plasma sprayed and deposited directly on the plate. The final deposit exhibited a Gaussian geometry with a base size of 170 mmx60 mm and height of approximately 12 mm. The primary processing parameters used in the experiments are listed in Table 7.

Table 7. LPPS processing parameters

	Specimen A	Specimen B
Power (KW)	135	126
Plasma Gas Ratio: Ar:H <sub>2</sub>	10 : 1	4:1
Powder feed rate (g/min)	75	70
Spray distance (mm)	250	350
Atmosphere (torr)	80	100

Following LPPS processing, the porosity in the as-sprayed W was evaluated. First, the density of the as-deposited W was determined on the basis of Archimedes' principle. It should be pointed out that prior to density measurements, the substrates were removed either by chemical dissolution or by mechanical sectioning. For specimen A, after the graphite cylinder was removed, the Mo layer and the interaction zone (approximately 125 µm in thickness) that formed between Mo and W, were dissolved using a solution of 2% hydrogen peroxide. For specimen B, the Mo substrate was sectioned off using a diamond saw. The porosity was then determined by the following equation

$$\text{Porosity} = \frac{\rho_{\text{th}} - \rho}{\rho_{\text{th}}} \quad (19)$$

where,  $\rho_{\text{th}}$  and  $\rho$  are theoretical density and measured density, respectively. Second, optical microscopy was employed to observe the pores presented in the specimen. The specimens were

sectioned, polished and observed under optical microscopy. Moreover, to determine the location of pores relative to the matrix materials, as-polished specimens were etched using modified Murakami's reagent (15 g K<sub>3</sub>Fe(CH)<sub>6</sub>, 2g NaOH and 100 ml H<sub>2</sub>O). Third, scanning electron microscopy (SEM) was used to document the morphology and location of pores on the fracture surface of the deposited W with a Hitachi-S-500 instrument. Fourth, the levels of nitrogen and oxygen in the deposit were determined (The analysis was done by Hermann C. Starck Berlin, Germany) in order to evaluate nitrogen and oxygen entrapment during plasma spraying. Finally, the as-received W powders were examined using SEM to identify the presence of porosity in the as-received powders.

#### 4.2. Results and Discussion

##### 4.2.1. Microstructure of Plasma Sprayed Tungsten

The microstructure of as-plasma sprayed W (Specimen B) is shown in Figure 13. It is clearly seen that a large amount of unmelted W particles present. However, the plasma processed W (specimen A) exhibits a different microstructure as shown in Figure 14. The deposited material exhibited an equiaxed grain morphology, with a range of grain sizes varying from 3 to 90 µm and an average of 17 µm (Figure 15). Moreover, inspection of the grain morphology reveals that some recrystallization occurred during deposition. This microstructure is different from the lamellae or wavy microstructures that are typically exhibited by other as-plasma-sprayed materials, such as Ni<sub>3</sub>Al and Ni base alloys [27, 124]. Upon annealing, however, the microstructure of these materials becomes similar to that observed herein for W, suggesting that the W experienced an elevated temperature exposure during plasma deposition. Actually, deliberate heating of the substrate following deposition can be viewed as an annealing process. This practice is generally used during the plasma spraying of refractory metals in order to control residual stress and increase density, as indicated by Smith and Apelian [124]. Moreover, the interaction between the plasma and the substrate, as well as the release of the latent heat of fusion ( $H_f = 1.71426 \times 10^5$  J/Kg for W [[125]]), further enhance recrystallization and grain growth in the deposited materials [27].

##### 4.2.2. Formation of Porosity During Plasma Spraying of Tungsten

The measured density and porosity for the deposited W specimens are listed in Table 8. The measured densities were 17.51 g/cm<sup>3</sup> for specimen A and 17.36 g/cm<sup>3</sup> for specimen B. Thus, the measured densities suggest a porosity of 9.0% and 9.8%, for specimen A and specimen B

Table 8. Measured Density and Porosity For Deposited W Specimen

	Specimen A	Specimen B
Density (g/cm <sup>3</sup> )	17.51	17.36
Porosity (%)	9.0	9.8

respectively when compared to the theoretical density of W ( $19.25 \text{ g/cm}^3$  [126]). This result is consistent with metallographic observations, which revealed that an elevated concentration of pores was present in LPPS processed W. Figure 16 reveals the as-polished surface of specimen (B) sectioned from the central section of the deposit. The pore sizes range from approximately about 5  $\mu\text{m}$  to 50  $\mu\text{m}$  in diameter. Furthermore, SEM studies of fracture surfaces revealed an elevated concentration of micrometer sized pores present in the LPPS processed W, as shown in Figure 17. This figure clearly reveals that the pores were present both intragranularly and transgranularly. Small intragranular pores, with an equivalent diameter that was generally smaller than 2  $\mu\text{m}$  (0.1 to 2  $\mu\text{m}$ ), were observed on cleavage surfaces (Figure. 17a). The relatively large pores (in the range of 1 to 5  $\mu\text{m}$ ) were generally present on the grain boundaries (Figure. 17b). Accordingly, the pores can be roughly classified into three categories in light of their sizes: that is, pores from 0.1  $\mu\text{m}$  to 2  $\mu\text{m}$  (present transgranularly); 1  $\mu\text{m}$  to 5  $\mu\text{m}$  (present intragranularly); and 5  $\mu\text{m}$  to 50  $\mu\text{m}$ . In the section that follows, the mechanisms associated with the formation of porosity during plasma spraying are discussed in detail.

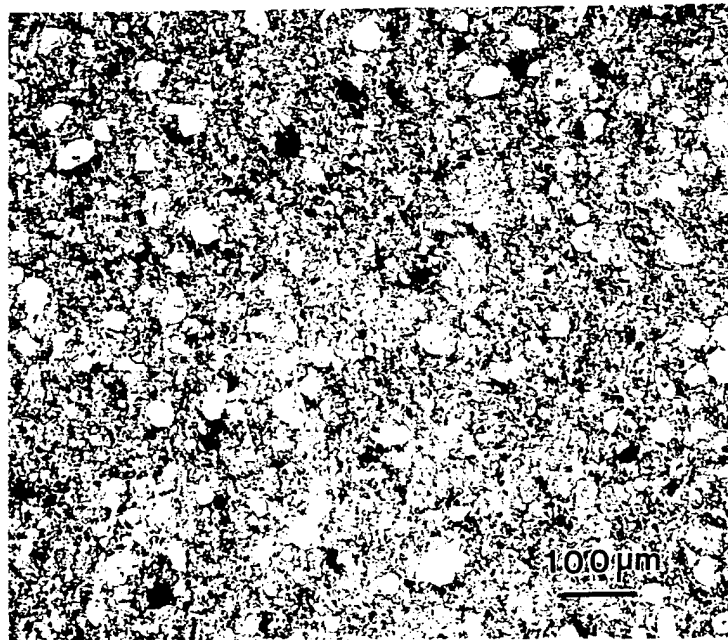


Figure 13. Microstructure of LPPS processed W (Specimen B).



Figure 14. Morphology of LPPS processed W. (Specimen A, Etchant: modified Murakami's reagent)

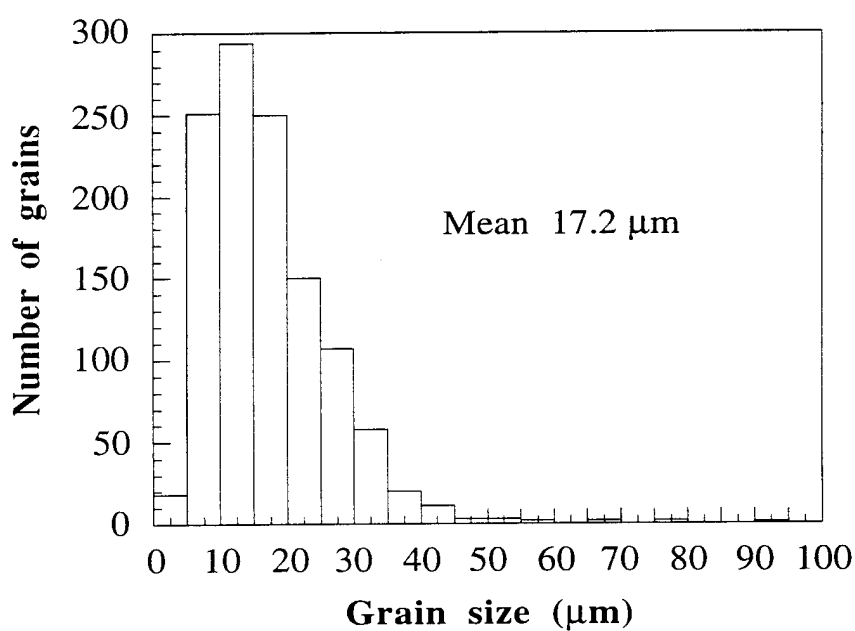


Figure 15. The distribution of grain sizes obtained from computerized image analysis.

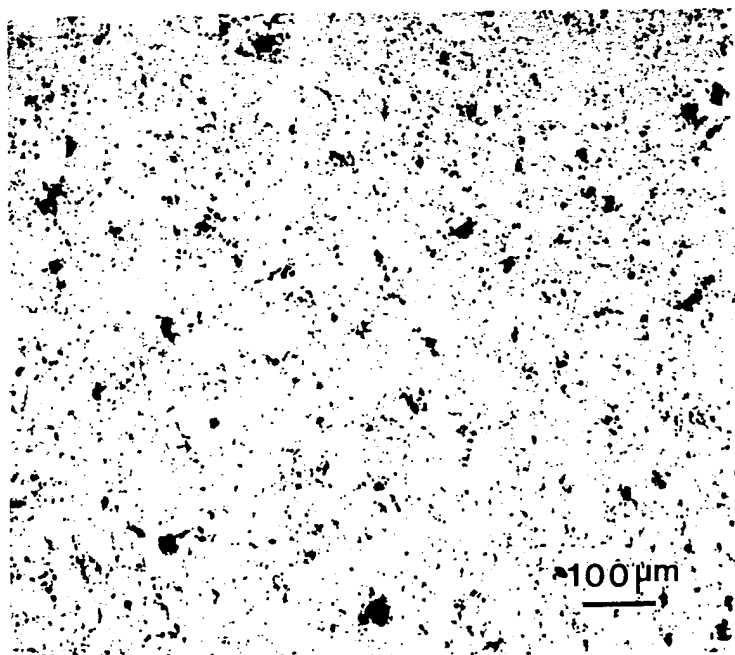


Figure 16. Microstructure of as-polished cross section of LPPS processed W (specimen B).

Numerous investigators have studied the effects of processing parameters on the density of plasma processed materials [26, 31, 89, 90]. For example, Smith and Mutasim [89] studied the concomitant influences of gas flow rate, nozzle type, spray distance and other variables on the density of the deposit. Murakami et al. [91] investigated the effects of substrate cooling on the formation of porosity. Evidently, the formation of porosity during plasma spraying and deposition is influenced by numerous processing parameters. However, the critical factors that strongly influence the formation of porosity are listed as follows: the particle melting state (or usually known as degree of melting); particle velocity upon impingement with the substrate; particle deformation and solidification. The degree of melting during plasma spraying is primarily associated with the particle-plasma interactions [25, 92], in which the primary factors are energy content of the plasma gas, powder particle feeding velocity and trajectories [93]. During plasma processing, an extremely sharp temperature gradient exists in the plasma jet. For example, the work done by McKelliget et al. [92] has indicated that the temperature field varies from 1000 K to 12.000K in a plasma jet using argon/hydrogen. Therefore, depending on powder type, size, shape and injection velocity, various powder states are produced as the powders travel through this gradient. These include fully molten powders (droplets) and partially molten powders and/or unmelted powders. Consequently, the dispersion of particles contains fully molten, partially molten or unmelted powders during impingement on the deposition surface. Upon impingement

with deposition surface, the powders and droplets exhibit different deformation and solidification behavior. As a result, interactions between these powders, between powders and deposition surfaces account for a significant proportion of porosity. In the discussion that follows, the mechanisms that may be responsible for the formation of porosity are discussed in light of the following factors: porosity from unmelted powder particles, porosity from flattened powder particles, porosity from gas entrapment, porosity from solidification shrinkage, and porosity from as-received powders.

#### 4.2.2.1. Porosity From Unmelted Particles

Figure 13 shows the etched cross-section of as-sprayed W (Specimen B). Clearly, a relatively large amount of unflattened particles are present in the deposit. These unflattened particles are morphologically similar to round particles. A microscopic examination by SEM indicated that most of the as-received particles exhibit an irregular morphology (Figure 18), which suggests that these unflattened particles have been partially melted and spheroidized during plasma processing. To further study the evolution of unmelted particles during plasma spraying, thermal history of W particles in the plasma processing was evaluated with the following heat transfer equation [127]

$$\frac{1}{\alpha_s} \frac{\partial T}{\partial t} = \frac{1}{r^2} \frac{\partial}{\partial r} \left( r^2 \frac{\partial T}{\partial r} \right) \quad (20)$$

where,  $r$  is distance in the radial direction and  $\alpha_s$  is the thermal diffusivity of W particle

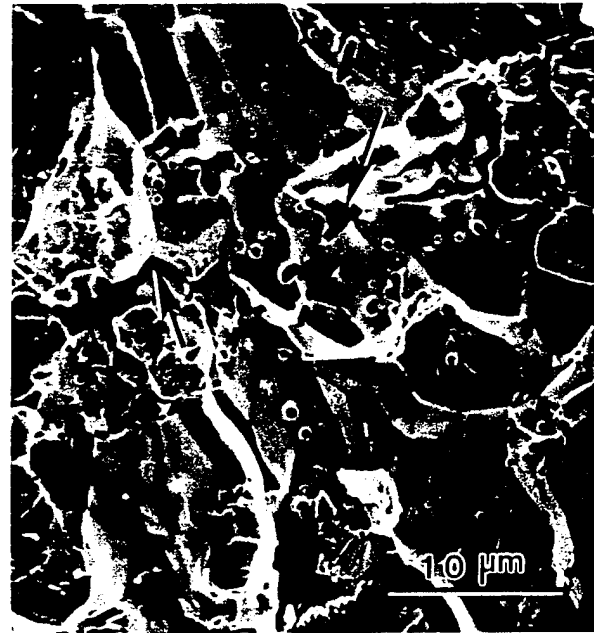
$$\alpha_s = \frac{K_s}{\rho_s C_s} \quad (21)$$

and  $K_s$ ,  $\rho_s$ ,  $C_s$  are thermal conductivity, density and heat capacity of W, respectively. For simplicity, the following assumptions were incorporated in the calculation:

- (1) The particle is spherical with constant thermal conductivity and heat capacity;
- (2) The initial temperature of the particle is uniform;
- (3) Each particles is suddenly injected into a plasma gas region that has constant temperature;



(a)



(b)

Figure 17. SEM micrographs showing the pores present (a) intragranularly and (b) intergranularly in the plasma sprayed W. (Specimen A)



Figure 18. Morphology of as-received W powders.

- (4) When the surface temperature of a particle reaches melting temperature, the entire particle is assumed to be molten. This assumption is justified on the basis of the results of Bourdin et al. [127], which indicated that the differences between center and surface temperature for W particles are negligible;
- (5) The radiation of the particles is not considered. This assumption is justified by the comparison between the radiative heat flux from particles and conductive heat flux from plasma gas. In most of the case, the radiative heat flux from particles is negligible [127].

The calculations were carried out for plasma gas temperature ranging from 4000K to 12000K and for particles sizes ranging from 10 to 50  $\mu\text{m}$  in diameter. The calculations revealed that the time required for melting a W particle in a plasma environment depends on the plasma gas temperature and the W particle size. It is evident that the time required to reach the melting point of W decreases with decreasing particle size. For example, it takes  $2 \times 10^{-2}$  sec. for a particle of 20  $\mu\text{m}$  in diameter to reach melting temperature, while for a particle of 50  $\mu\text{m}$  it takes  $1.5 \times 10^{-1}$  sec. Furthermore, as the plasma gas temperature increases, the time required for reaching melting point of W decreases. Accordingly, on the basis of these results, it is possible to estimate the extent of melting of W particles. For that purpose, the particle velocity measured by Vardelle et al. [128] were used. Their results showed that for the particle sizes ranging from 23 to 46  $\mu\text{m}$ , the particle

velocities range from 50 to 150 m/sec., approximately. Thus, if the velocity is assumed as an average of 100 m/sec., the relationship between flight distance and surface temperature of particles may be determined, as shown in Figure 19 and Figure 20. For specimen B, the spray distance is 350 mm as listed in Table 7. Then, the temperature of W particles with size greater than 30  $\mu\text{m}$  will be below the melting point (3683K); that is, particles are unmelted, upon the impingement on the substrate (Figure 19). On the other hand, a W particle of 25  $\mu\text{m}$  in diameter that is injected into the plasma gas region with a temperature below 6000K, will not be molten upon impingement on the substrate (Figure 20). Therefore, depending on the plasma temperature, particle size and particle velocity in the plasma gas, a finite amount of injected W particles will remain unmelted upon impingement, which is in agreement with the experimental observation (Figure 13). It is worth to noted that since the as-received W particles were not completely spherical (Figure 18), the presence of experimentally observed spherical particles in the LPPS W suggests that these particles may have partially melted, and hence spheroidized, which is probably resulted from the curvature effect.

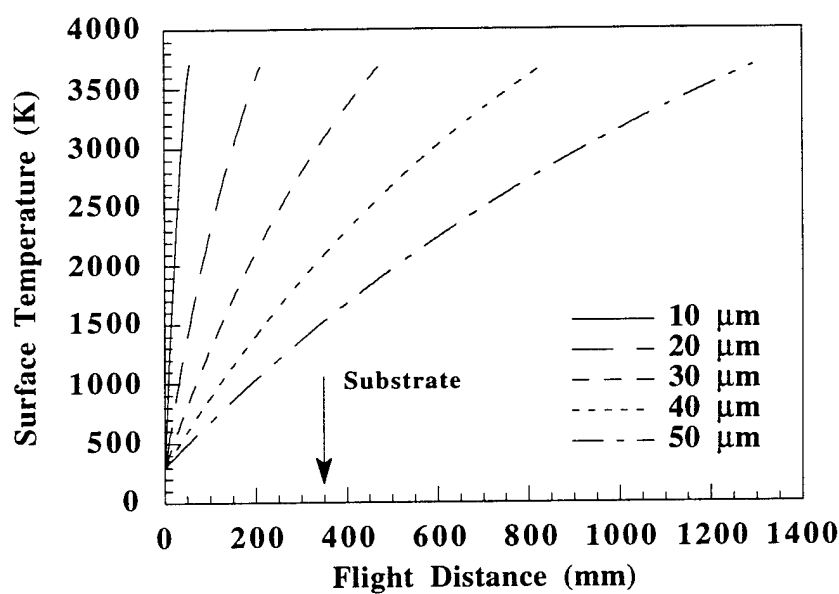


Figure 19. The relationship between flight distance and surface temperature of particles for various particle sizes.

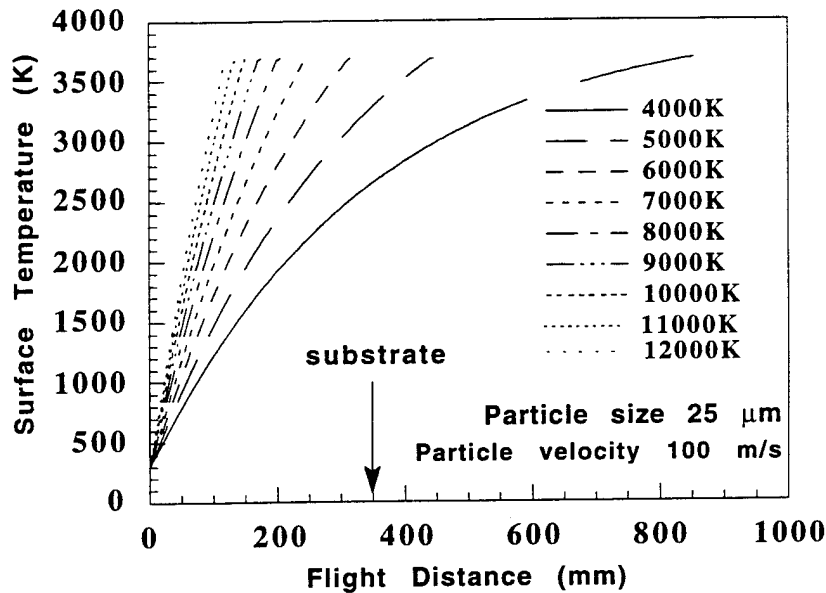


Figure 20. Surface temperature profile of a W particle versus particle flight distance.

One of the mechanisms for the formation of porosity from partially melted particles was discussed by Sivakumar et al. [129]. A partially melted particle consists of a solid core surrounded by liquid. When the particle impinges on the substrate, the solid core rebounds from the substrate and leaves a cavity. This mechanism may be responsible for some of the pores formed in LPPS processing, especially the larger pores (5 to 50  $\mu\text{m}$ ). However, other mechanisms must also be considered. By carefully examining the microstructures of as-sprayed W, two mechanisms of porosity formation are identified. The first one is due to the interaction between partially melted particles. Consider two partially melted particles impinging on the deposition surface adjacent to each other (Figure 21a). Since there is limited deformation upon impingement on the substrate, the interstitial sites between the two particles will eventually become cavities if there is not enough liquid flowing into these spaces. Therefore, it is reasonable to anticipate that porosity will increase as the proportion of partially melted particles increases in the plasma spray. In this mechanism, the pore size will depend on the size of the partially melted particles. Simple geometrical estimations indicated that the pore size resulting from this mechanism will be approximately 7 to 11  $\mu\text{m}$  for 20 to 30  $\mu\text{m}$  of the partially melted particles, which is fairly in agreement with microstructure observations. The second mechanism is related to the interaction between partially melted particles and previously deposited layers. When a partially melted particle impinges on an irregular surface (e.g., pre-solidified particles), pores form as the liquid is unable to completely fill in the interstices below the particle. One example is shown in Figure 21b. Many investigators [25, 90, 124, 128,

[130] have indicated that to achieve high densities during plasma spraying, it is necessary that a large proportion of the powders be completely molten during impingement with the deposition surface. Apparently, the present experimental results support this argument. The elevated temperature of fusion of W is thought to be the primary reason for the presence of the observed large amount of partially melted particles in the deposit. According to the calculation results stated above, it is anticipated that the use of smaller powder sizes should lead to a decrease in the proportion of partially melted particles and therefore lead to a decrease in porosity.

#### 4.2.2.2. Porosity From Melted Powder Particles

The interaction between completely molten particles and the deposition surface is also proposed as a possible mechanism responsible for the formation of porosity. This mechanism of porosity has been described by Apelian et al. [25]. A completely molten droplet, after impinging on the substrate or on other droplets, tends to deform radially in the form of a thin disc. When the bonding between the thin disc and the contact surface below is not sufficiently strong, however, the outer portion of the disc tends to separate from the surface and fold in towards the center region. Hence, any cavities that are not subsequently filled up by incoming droplets remain as porosity in the plasma deposited material. To that effect, a numerical investigation has been conducted on porosity formation during plasma spraying W. The detailed is described elsewhere [131, 132], and hence only a brief description is given here. It is indicated that the formation of porosity is a result of interactions between droplet deformation and droplet solidification after impingement on the deposition surface. In the study, the droplet solidification is related to the moving velocity of solid-liquid interface, while the droplet deformation is related to flattening splat diameter. If the solidification occurs after the deformation is complete, any voids formed during droplet deformation will be filled in by liquid, which results in a low porosity. If solidification is much faster than deformation, the droplet will freeze before voids are formed, which also results in a low porosity. However, if the solidification and deformation carry out comparably fast, the situation will be that unsolidified liquid above solid/liquid interface continues to deform and spread out whereas the underlying solidified portion of the splat is fixed on the deposition surface. This eventually leads to the separation of the liquid from the solid/liquid interface and leads to the formation of voids. The pores are anticipated to be formed within the splat and the sizes are small, which probably correspond to the pores with the sizes of 0.1 to 5  $\mu\text{m}$  observed in the experiments.

Moreover, as a result of close microstructural examination, another mechanism is identified. This mechanism can be described as the stacking of flattened particles. Consider the impingement of two completely melted particles. When the first particle impinges on the deposition surface, it becomes flattened. Subsequently, a second one impinges on the first one. If the second one spreads over the edge of the first one, pores will form. One example observed in the LPPS

processed W studied here is shown in Figure 22. Since the thickness of flattened particles is small (roughly in the range of 1 to 5  $\mu\text{m}$ ), the pores formed should also be small (about 1 to 5  $\mu\text{m}$ ).

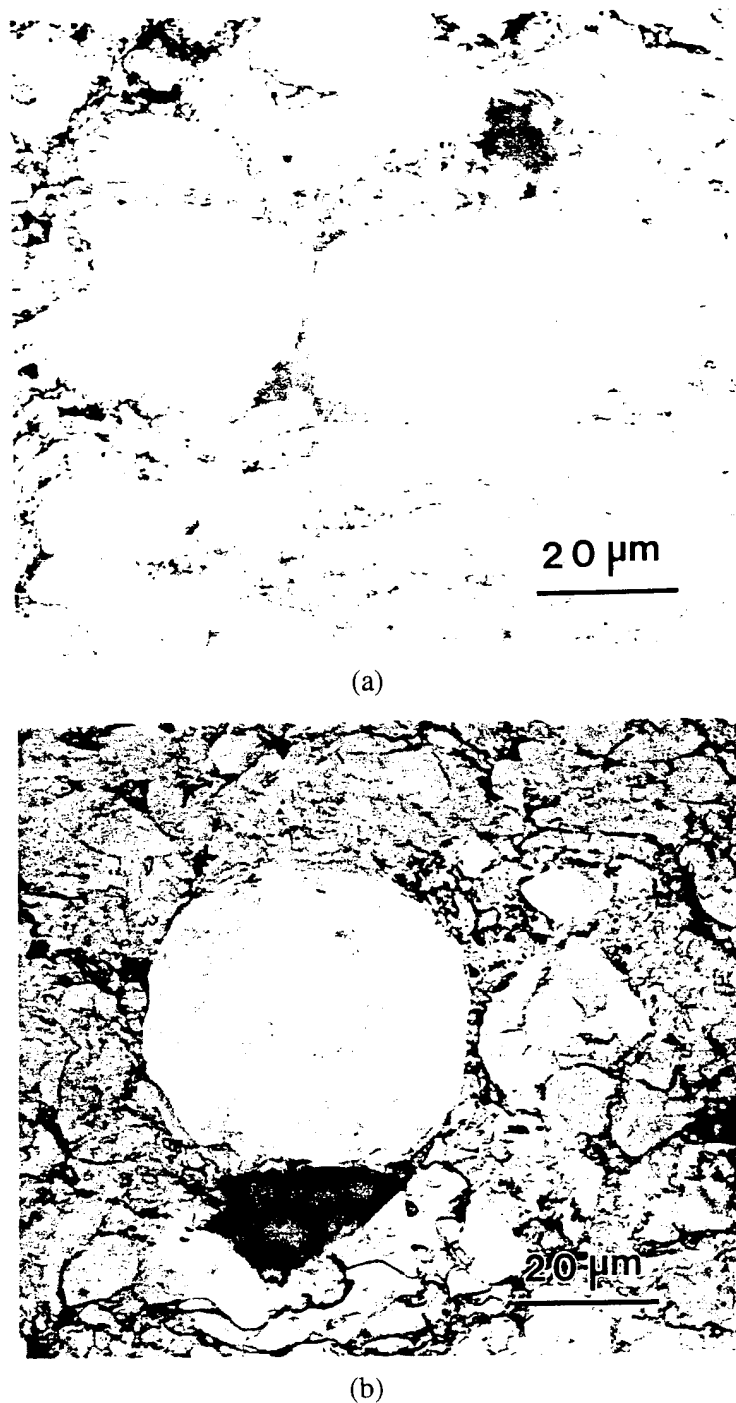


Figure 21. The formation of pores due to the interaction (a) between partially melted particles and (b) between partially melted particles and deposition surfaces. (Specimen B)

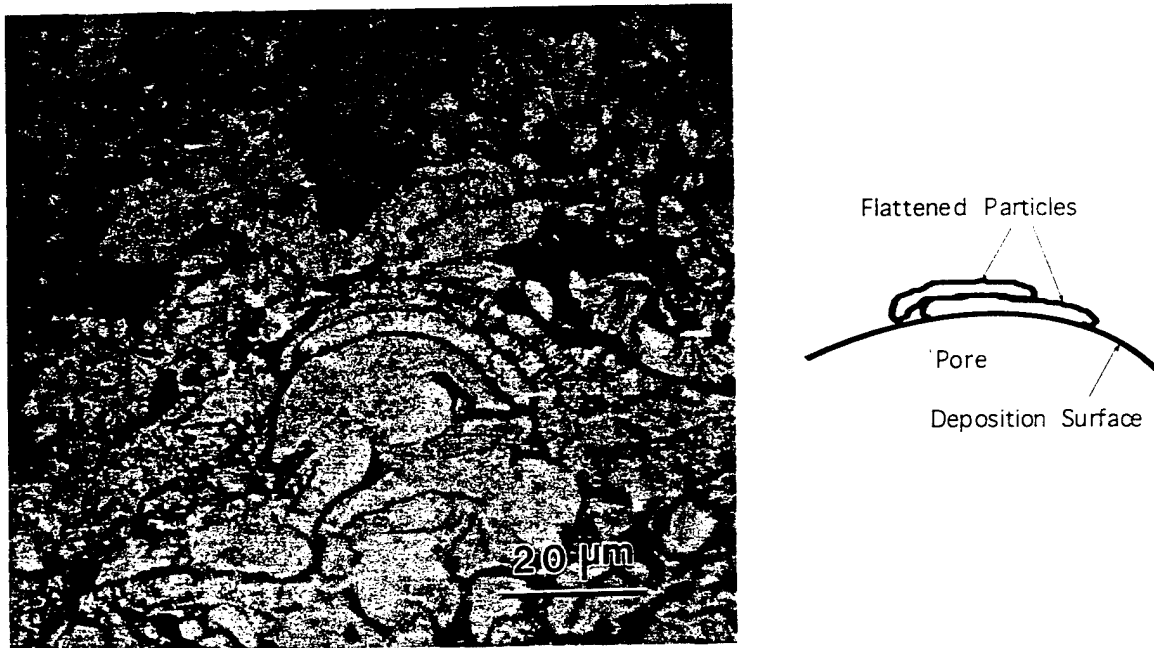


Figure 22. The formation of pores due to the stacking of flattened particles (Specimen B).

#### 4.2.2.3. Porosity From Gas Entrapment

Gas entrapment in the material during plasma processing may lead to formation of the porosity. Accordingly, the concentration of nitrogen and oxygen in as-received W powders and the LPPS processed W was measured, and the results are summarized in Table 9. It is observed that the nitrogen content was found to slightly increase from 12 to 26 ppm. Since the increased amount is small, it is anticipated that the contribution to the formation of the porosity from nitrogen is very insignificant. On the other hand, it is worth noting that the content of oxygen decreased from 250 ppm to 154 ppm, following LPPS processing. This phenomena has also been observed for plasma-deposited Nb and its alloys [32], and Beryllium [133]. Jackson et al. [32] suggested that the decrease in oxygen content in Nb and its alloys may be attributed to the removal of oxygen from the powder surface due to volatilization of the powder during spraying. This mechanism may also explain the decrease in oxygen contents observed herein. To that effect, it is well established

Table 9. Comparison of Gas Content Before and After Plasma Deposition

	W Powder, ppm	W Deposit, ppm
Carbon	10	100
Nitrogen	12	26
Oxygen	250	154

that  $\text{WO}_3$  is volatile above  $800^\circ\text{C}$  [134], therefore, it is highly probable that any  $\text{WO}_3$  that may have been present on the surface of the W powders was vaporized during plasma spraying, thereby leading to a decrease in the oxygen content. Evidently, oxygen does not contribute significantly to the observed porosity. However, the entrapment of plasma gases such as hydrogen and argon may account for formation of some porosity, especially the large round pores observed in the deposit (Figure 23).

#### 4.2.2.4. Porosity From Solidification Shrinkage

The presence of solidification shrinkage may also have contributed to the formation of pores during plasma processing. To that effect, the fracture surface of the LPPS processed W provides experimental support to this suggestion, as shown in Figure 24. In this figure, solidification shrinkage is present as irregular cavities that form as a result of differences in the molar volume of the solid ( $9.5 \text{ cm}^3/\text{mole}$ ) and liquid ( $10.4 \text{ cm}^3/\text{mole}$ ) during the material solidification. Therefore, the non-uniform shrinkage during solidification of both completely molten powders and partially molten powders, would certainly contribute to the porosity in the deposited materials.

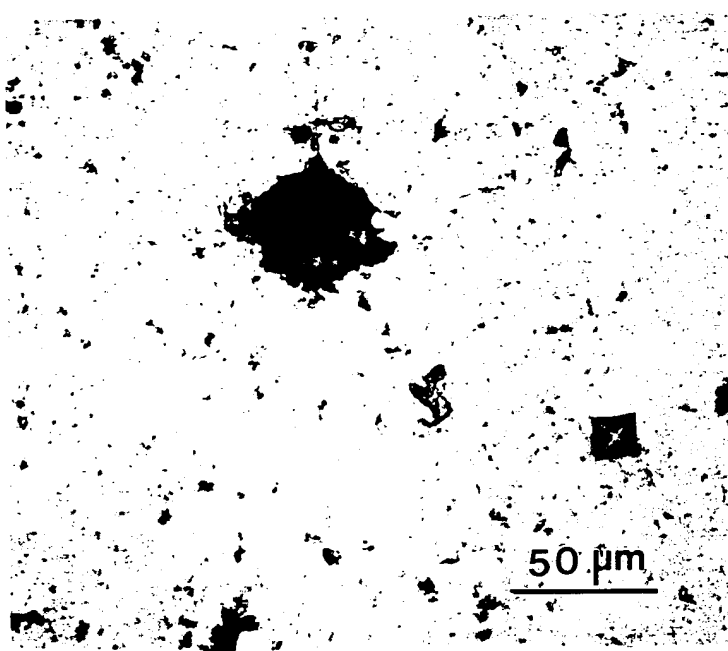


Figure 23. The large pores observed in the LPPS processed W (Specimen B)

#### 4.2.2.5. Porosity From As-Received Powders

The presence of porosity in the as-received W particle powders is also proposed to have contributed to porosity in the LPPS processed W. To that effect, observation of the as-received W powders using SEM revealed the presence of pores in the as-received W powders. Most of these pores appeared to be located in the interior of powders (Figure 25) and the surface seldom revealed any porosity (Figure 18). Since some of powders were partially melted or unmelted during spraying as discussed above, it is plausible that the porosity that was present in the as-received powders eventually became entrained in the deposited W.



Figure 24. SEM photograph showing solidification shrinkage in LPPS processed W (Specimen A).

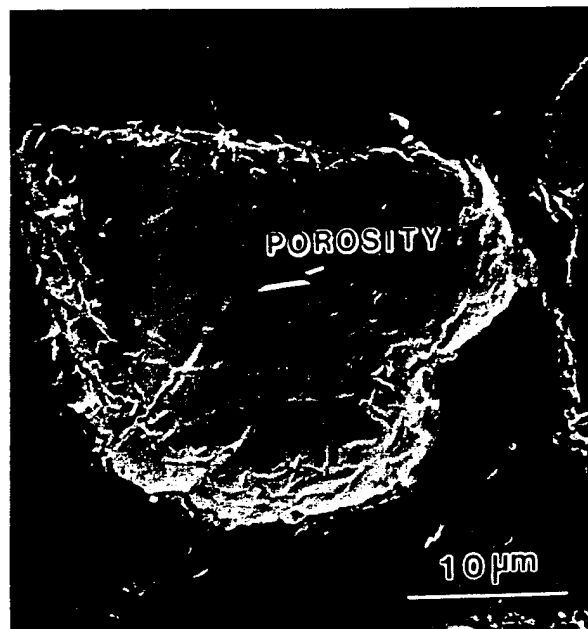


Figure 25. SEM photograph showing the pores present in the as-received W powders.

## V. NUMERICAL ANALYSIS OF POROSITY EVOLUTION DURING LOW PRESSURE PLASMA SPRAYING OF TUNGSTEN

### 5.1. Numerical Model and Computational Method

Two challenging problems existing in the numerical study are: a) the treatment of complex interfacial phenomena induced by the solidification and the formation of free surfaces with arbitrary geometrical shape, and b) the simulation of three phases, i.e., liquid, solid and gas (void) phases present and/or generated during the deformation and solidification of droplets. The transient nature of the moving solid/liquid interface is one of the most difficult factors inherent in the modeling. Since the details of the model formulation and computational methodology have been given elsewhere [132], only a brief description will be presented here.

The governing equations describing the motion and interaction during droplet flattening include the incompressibility condition, the full Navier-Stokes equations for transient, axisymmetric, viscous, incompressible fluid flow, and the transport equation for VOF function. Considering solidification during the flattening, the governing equations are modified on the basis of a two-phase flow continuum model [132] as

$$\nabla \cdot (\Theta \vec{v}) = 0 \quad (22)$$

for continuity,

$$\Theta \frac{\partial \vec{v}}{\partial t} + \nabla \cdot (\Theta \vec{v} \vec{v}) = -\frac{\Theta}{\rho} \nabla p + \frac{\Theta}{\rho} \nabla \cdot \tau + \Theta \vec{g} + \Theta \vec{F}_b \quad (23)$$

for momentum transport, and

$$\frac{\partial}{\partial t} (\Theta F) + \nabla \cdot (\Theta F \vec{v}) = 0 \quad (24)$$

for VOF transport. In this continuum model, the flow is modeled as a special case of two-phase flow by introducing a volume fraction  $\Theta$ , which is a continuous average quantity defined to be unity in any cell fully occupied by fluid, zero in any cell fully occupied by solid, and between zero and unity in any cell containing the solid/liquid interface

$$\Theta = \begin{cases} 1, & \text{fluid cell} \\ > 0, < 1, & \text{interface - containing cell} \\ 0, & \text{solid cell} \end{cases} \quad (25)$$

In order to calculate  $\Theta$ , the solid/liquid interface position at any time is determined by employing the 2-domain method [135]. The thickness of the solidified layer in a splat is estimated here using the 1-D solution of the Stefan problem of solidification, given by [135-137]

$$Y = U \sqrt{a_s(t - t_i)} \quad (26)$$

with the freezing constant  $U$  [135-137]

$$U = \frac{2}{\sqrt{\pi}} \left\{ \frac{T_s^*}{\left[ \operatorname{erf} \frac{U}{2} \right] \exp \left( \frac{U^4}{4} \right)} - \frac{T_l^* \sqrt{\frac{(k\varphi)_l}{(k\varphi)_s}}}{\operatorname{erfc} \left[ \frac{U}{2} \sqrt{\frac{a_s}{a_l}} \right] \exp \left( - \frac{U^2 a_s}{4 a_l} \right)} \right\} \quad (27)$$

where  $T_s^*$  and  $T_l^*$  are defined as [135-137]

$$T_s^* = \frac{k_s(T_m - T_s)}{a_s \rho_s \Delta h}, \quad T_l^* = \frac{k_s(T_l - T_m)}{a_s \rho_s \Delta h} \quad (28)$$

The governing equations, Eqs. (20) - (22), in primitive variables are solved on an Eulerian, rectangular, staggered mesh in cylindrical geometry with the extended SOLA-VOF method [138]. At the bottom boundary and the solid/liquid interface, a no-slip boundary condition is imposed, whereas at other boundaries and at the symmetry axis, a free-slip boundary condition is employed. The splat temperatures at the substrate surface, at the solid/liquid interface and in the liquid phase are assumed to equal the substrate temperature, the melting temperature of droplet materials, and the initial droplet temperature, respectively. Free surfaces are determined with the data of the VOF function on the mesh and surface tension at free surfaces is simulated using a continuum surface force model [138]. The solid/liquid interface is tracked using Eqs. (23) - (26). The numerical computations are performed by modifying a program called RIPPLE [138] on a DEC 3000/400 AXP workstation. The details of numerical schemes and solution techniques have been completely documented in [138] and will not be repeated herein.

In order to quantitatively investigate the effects of processing parameters on the formation of micro-pores, micro-porosity is calculated using the data of the VOF function. The micro-porosity is defined as the volume fraction of the micro-voids which are entrapped into the splat during deformation and eventually contained within the solidified layer due to rapid solidification. The micro-porosity is calculated using the following equation (Figure 26)

$$\text{Porosity} = \frac{\sum_{i=1,N} \sum_{t=t_i, t_s} [z_s(i, t + dt) - z_s(i, t)] \pi [r(i+1)^2 - r(i)^2] (1 - F(i, t))}{\sum_{i=1,N} z_s(i, t_s) \pi [r(i+1)^2 - r(i)^2]} \quad (29)$$

The calculation is conducted at each time step for the annular volume  $i$  in the cell where the solidified layer thickness has increased from  $z_s(i, t)$  to  $z_s(i, t+dt)$  within the time step  $dt$ . This calculation is complete when the solidification front reaches the top of volume  $i$ . The corresponding solidification time and solidified layer thickness in volume  $i$  is  $t_s$  and  $z_s(i, t_s)$ . Such calculation is conducted for each annular volume ( $i = 1, 2, 3, \dots, NA$ ) once solidification starts in that volume. When the entire splat is solidified, the calculated volume of voids in each annular volume is added together ( $i = 1, NA$ ) to get the total volume of voids in the entire splat. This total volume of voids is then divided by the total volume of the splat. The result is the micro-porosity of the splat.

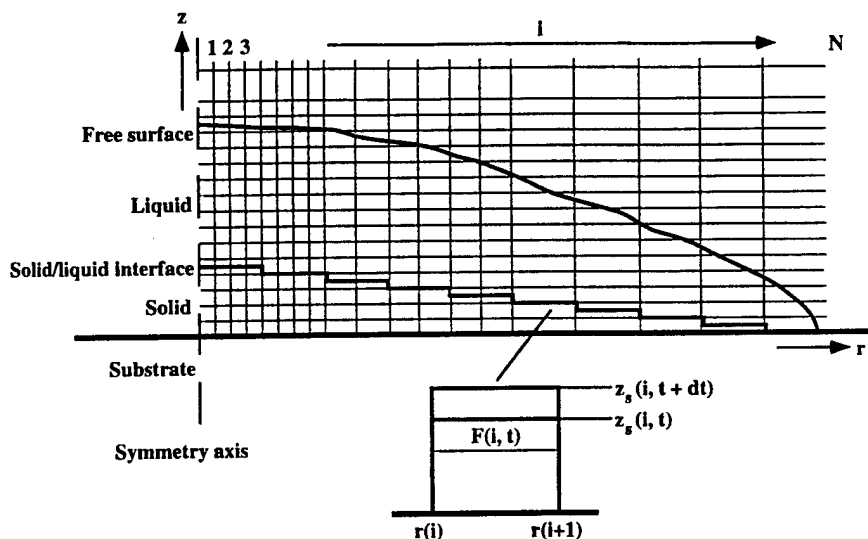


Figure 26. Schematic showing computation method of micro-porosity.

## 5.2. Results and Discussion

The processing parameters are chosen to cover a large range of operation conditions in plasma spray processes. Droplets of initial diameter 30  $\mu\text{m}$  with impact velocities of 100, 400 and 900 m/s, respectively, are taken into consideration. Two droplet temperatures, i.e., 3650 and 3750 K, and different substrate temperatures, ranging from 1000, 1500, 2000, 2900 to 3400 K, are employed since in typical LPPS procedures the plasma torch is used to clean the substrate prior to deposition, thus significantly heating the substrate. The physical properties of liquid and solid W, as well as the temperature-dependence of the freezing constant U are given in [132]. In the following, the numerical results will be presented and discussed in detail.

### 5.2.1. Formation of Micro-Pores During Deformation of A Single Droplet on Flat Surface

The calculated deformation and solidification sequence of a single W droplet impinging onto a flat substrate is shown in Figure 27. The solid/liquid interface is indicated by the dark line and the splat contour is represented by the thin line. As observed in Figure 27, the droplet does not splash upwards during impact, but instead spreads uniformly in the radial direction. With increasing time, the splat height decreases and its diameter increases. Finally, it solidifies into a very thin splat at about 0.21  $\mu\text{s}$  after impact. At  $t = 0.045 \mu\text{s}$ , the edge of the splat separates from the solid/liquid interface. In the present study, we refer to this phenomenon as separation phenomenon. This phenomenon, as schematically depicted in Figure 28, will lead to the formation of voids near the splat edge which may develop into micro-pores in as-sprayed materials. Hence, in the present paper, the voids which are entrapped into the splat during separation are considered as a type of micro-porosity and quantitatively calculated using Eq. (27).

### 5.2.2. Effects of Droplet and Substrate Temperatures On Formation of Micro-Pores

The calculated micro-porosity within a solidified splat vs. the substrate temperature is summarized in Figure 29. Also shown are the effects of the droplet temperature. The initial droplet diameter and velocity are maintained constant. The results shown in Figure 29 reveal that for a constant droplet temperature the micro-porosity decreases with increasing substrate temperature; and for a constant substrate temperature the micro-porosity decreases with increasing

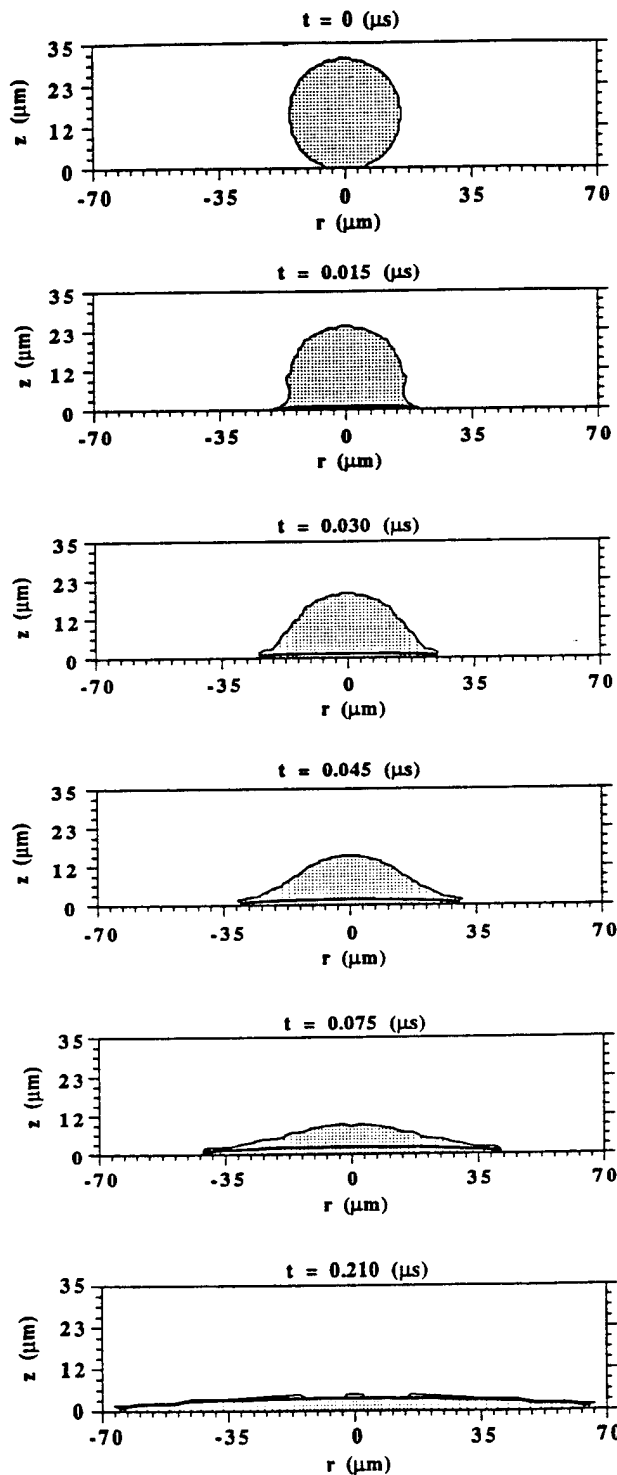


Figure 27. Deformation and solidification sequence of a single W droplet;  $d_0 = 30 \text{ } \mu\text{m}$ ,  $u_0 = 400 \text{ m/s}$ ,  $T_l = 3750 \text{ K}$ ,  $T_s = 1500 \text{ K}$ .

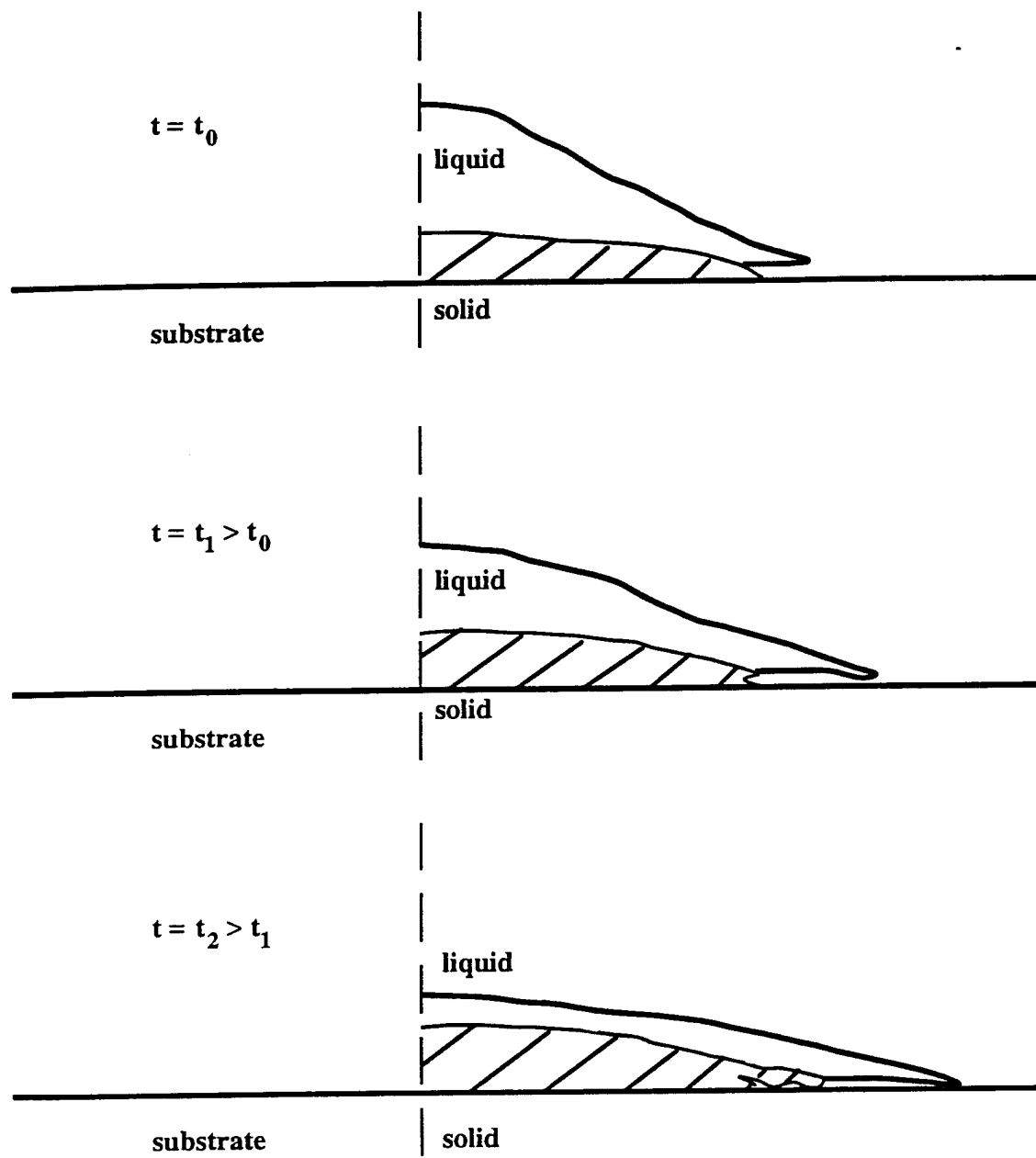


Figure 28. Schematic diagram showing formation mechanism of micro-pores.

droplet temperature. However, there exists a clear transition in the variations of the micro-porosity with temperature. For example, at a droplet temperature of 3650 K and a substrate temperature lower than 2000 K (or at a droplet temperature of 3750 K and a substrate temperature lower than 1500 K), the micro-porosity decreases with decreasing substrate temperature. This observation suggests that there may be two opposite factors influencing the formation of micro-pores. In order to determine the nature of these factors, the initial rising velocity of the solid/liquid interface and the time corresponding to the separation, are plotted vs. the substrate temperature in Figures 30 and 31, respectively.

The rising velocity of the solid/liquid interface is defined as the derivative of the thickness of the solidified layer with time and is calculated using Eq. (24). The results in Figure 30 indicate that the initial rising velocity of the solid/liquid interface at 0.015  $\mu$ s after impact is indeed very high, and it increases rapidly with decreasing substrate temperature, especially for the lower droplet temperature (comparing the solid line to the dash line in Figure 30). The results in Figure 31 show that for a constant droplet temperature, the time, at which the separation begins, decreases with decreasing substrate temperature; and for a constant substrate temperature, the separation time decreases with decreasing droplet temperature. This trend is a direct result of the increase in the solid/liquid interface rising velocity with decreasing substrate temperature and/or decreasing droplet temperature. Accordingly, the faster the rising velocity of the solid/liquid interface, the earlier the separation occurs. On the basis of these results, the influence of the droplet and substrate temperatures on the formation of micro-pores may be then rationalized.

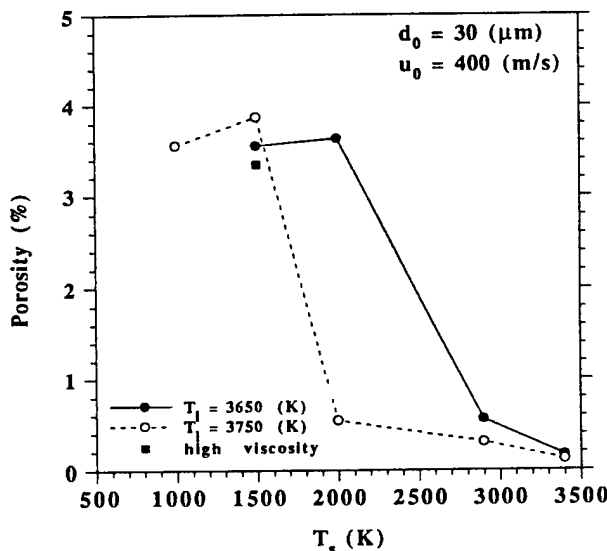


Figure 29. Micro-porosity formed during droplet deformation and solidification and its dependence on substrate temperature and droplet temperature ( $d_0 = 30 \mu\text{m}$ ,  $u_0 = 400 \text{ m/s}$ ).

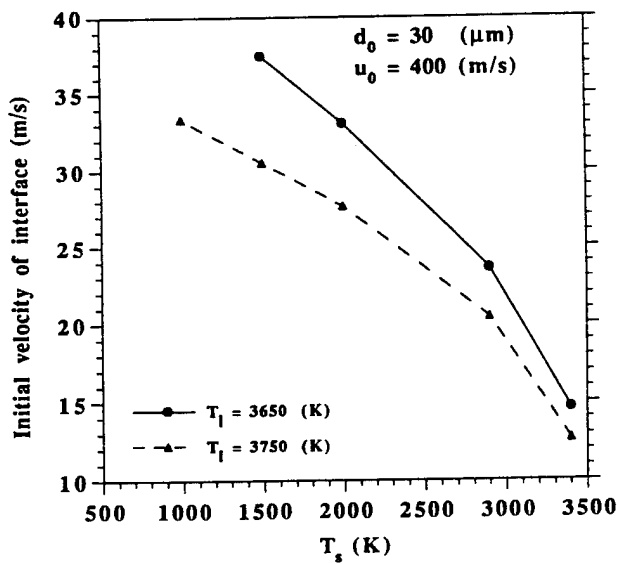


Figure 30. Initial rising velocity of solid/liquid interface as a function of substrate temperature and droplet temperature.

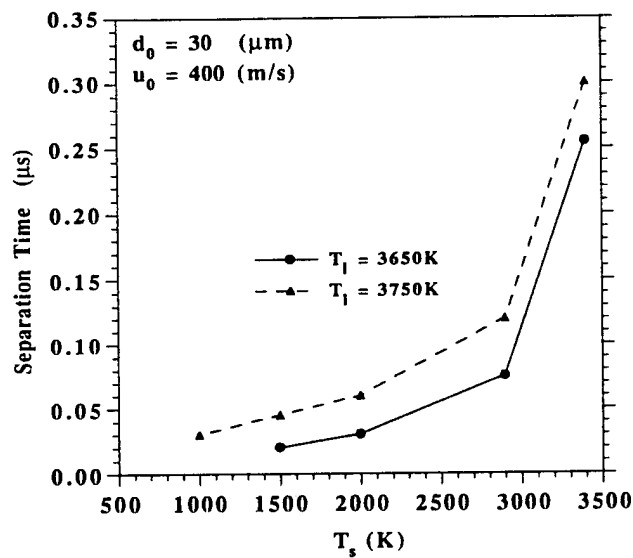


Figure 31. Separation time as a function of substrate temperature and droplet temperature.

For higher substrate temperatures, the rising velocity of the interface is still not very high and the separation occurs at a later time. This implies that fewer voids are formed as a result of later separation, and the droplet experiences extensive deformation before significant solidification occurs. Hence, the voids formed during deformation are filled in by the molten metal before they are fixed by solidification. In contrast, for lower substrate temperatures, two mechanisms may act. First, solidification is more rapid than deformation, so that the molten metal is solidified before voids are generated. Alternatively, fewer voids are contained in the solidified layer as a result of the decreased total solidification time with decreasing substrate temperature [132]. This is the reason why the micro-porosity turns to decrease when the substrate temperature decreases from 2000 to 1500 K for  $T_l=3650$  K and from 1500 to 1000 K for  $T_l=3750$  K.

At the transition temperature ( $T_s=2000$  K for  $T_l=3650$  K and  $T_s=1500$  K for  $T_l=3750$  K), the solid/liquid interface grows rapidly upwards, and simultaneously, deformation also occurs rapidly. Accordingly, the large radial velocities of the remaining liquid above the interface lead to a rapid spreading of the fringe of the splat, while the underlying solidified portion of the splat is fixed on the substrate. As a result of the separation of the liquid from the interface, voids are formed and fixed within the solidified layer due to its rapid growth. This suggestion is supported by the result that more pores are found in the fringe region of the splat. Additional support to this suggestion is the nearly identical values of the micro-porosity for the droplet temperatures of 3650 K and 3750 K at a substrate temperature of 3400 K. This interesting phenomenon indicates that droplet deformation is indeed completed before significant solidification occurs due to the relatively low rising velocity of the interface present at this high substrate temperature, regardless of the droplet temperatures.

### 5.2.3. Effect of Droplet Viscosity On Formation of Micro-Pores

In order to examine the effect of viscosity, a larger value of viscosity is assumed, the magnitude of which is two orders higher than that in the liquid state. The micro-porosity calculated under this mushy droplet condition is plotted in Figure 29 (the square symbol). Clearly, the micro-porosity in this case is lower than that at the same droplet temperature (3750 K) and the same substrate temperature (1500 K). This is not unexpected, since the rising velocity of the solid/liquid interface is the same in the two cases (due to the same thermal condition), but the deformation under the mushy droplet condition is slower (due to higher viscous consumption). Moreover, the flattening splat exhibits a negligible edge separation only at 0.045  $\mu$ s after impact, and no violent separation is detected at subsequent time. Nevertheless, under the mushy droplet condition, a high initial impact velocity is absolutely necessary to achieve a large flattening extent.

#### 5.2.4. Effect of Initial Impact Velocity On Formation of Micro-Pores

The calculated micro-porosity within a solidified splat vs. the initial impact velocity is summarized in Figure 32. The initial droplet diameter, droplet temperature and substrate temperature are maintained constant.

The calculated results reveal that the violent extent of the separation and hence the formation of micro-pores is critically influenced by the initial impact velocity, as evident from the results shown in Figure 32. The trend in this figure again suggests that the mechanism governing the formation of micro-pores is intimately coupled to the relative magnitudes of the solidification and deformation velocities. Accordingly, at a high initial impact velocity (e.g. 900 m/s), significant flattening takes place before significant solidification has occurred. Hence the micro-porosity is low (see the point on the right hand side in Figure 32). In contrast, at a low initial impact velocity (e.g. 100 m/s), the flattening is slow. The solid/liquid interface moves into the droplet liquid phase which does not contain many voids due to the slow deformation. Consequently, the micro-porosity is also low (see the point on the left hand side in Figure 32). However, it should be noted, that in spite of the low micro-porosity corresponding to the low initial impact velocity, the diameter of the final splat formed at such low initial impact velocity will also be small. A small splat diameter, on the one hand, reduces the contact area between the splat and the substrate, and on the other hand, may lead to the formation of macro-pores between adjacent droplets. Therefore, a high initial impact

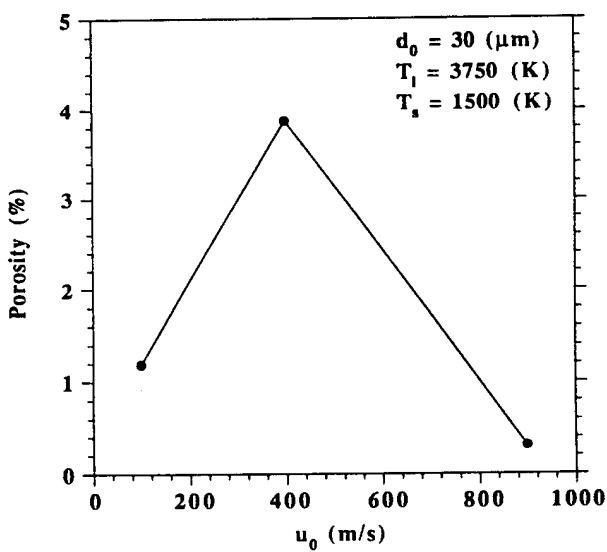


Figure 32. Micro-porosity formed during droplet deformation and solidification and its dependence on the initial impact velocity;  $d_0 = 30 \mu\text{m}$ ,  $T_l = 3750 \text{ K}$ ,  $T_s = 1500 \text{ K}$ .

velocity should be preferred, when a small porosity is desired. However, an initial impact velocity of 400 m/s leads to the highest micro-porosity among the velocities considered under the thermal conditions of  $T_l=3750$  K and  $T_s=1500$  K (see the point in the middle of Figure 32). In this case, the deformation and solidification velocities are comparable. As a result, a large portion of the voids generated during droplet flattening are contained within the solidified layer, leading to the high micro-porosity.

#### 5.2.5. Formation of Micro-Pores During Interaction of Multiple Droplets On Flat Surface

The calculated sequence of collision, interaction and solidification of two droplets in tandem is shown in Figure 33. As illustrated in Figure 33, when the second droplet impinges the flattening splat beneath it ( $t = 0.120 \mu\text{s}$  after impact), its interaction with the radial sheet jet of the first droplet produces upward and outward ejection. With increasing time, e.g., from  $t = 0.120$  to  $0.255 \mu\text{s}$  after impact, the outward ejection enlarges itself gradually. As a result of solidification, the ejection is largely depressed relative to that in a fully liquid case. Therefore, a mushy surface condition should be preferred in order to reduce ejection and improve adhesion between droplets and/or splats. Moreover, it is also clear in the figure, the interaction between the two droplets intensifies the separation, leading to an increase in the micro-porosity.

The calculated sequence of collision, interaction and solidification of an axisymmetric toroidal ring impinging onto the splat of an earlier droplet is plotted in Figure 34. As shown in Figure 34, when the ring impinges the flattening splat below it, the outside fringe of the ring spreads outwards, while the interaction between the inside fringe of the ring and the radial sheet jet of the earlier droplet causes inward and upward bounce of the liquid in the interaction region. This phenomenon results from the opposite flow directions of the splat liquid (outwards) and the ring liquid (inwards). This interaction leads to the formation of voids at the locations of vortices within the liquid ( $t = 0.165$  to  $0.255 \mu\text{s}$  after impact). Under the present computation conditions, however, some of such voids are filled in by the remaining liquid during the subsequent deformation, since the rising velocity of the solid/liquid interface reduces with increasing time, and hence, is not as rapid so to freeze these voids within the solidified layer. At the same time, some new voids form during the subsequent vortex movement. In addition, the inwards flow of the ring liquid contributes to fill in the voids in the fringe region of the earlier splat, leading to a decrease in the micro-porosity.

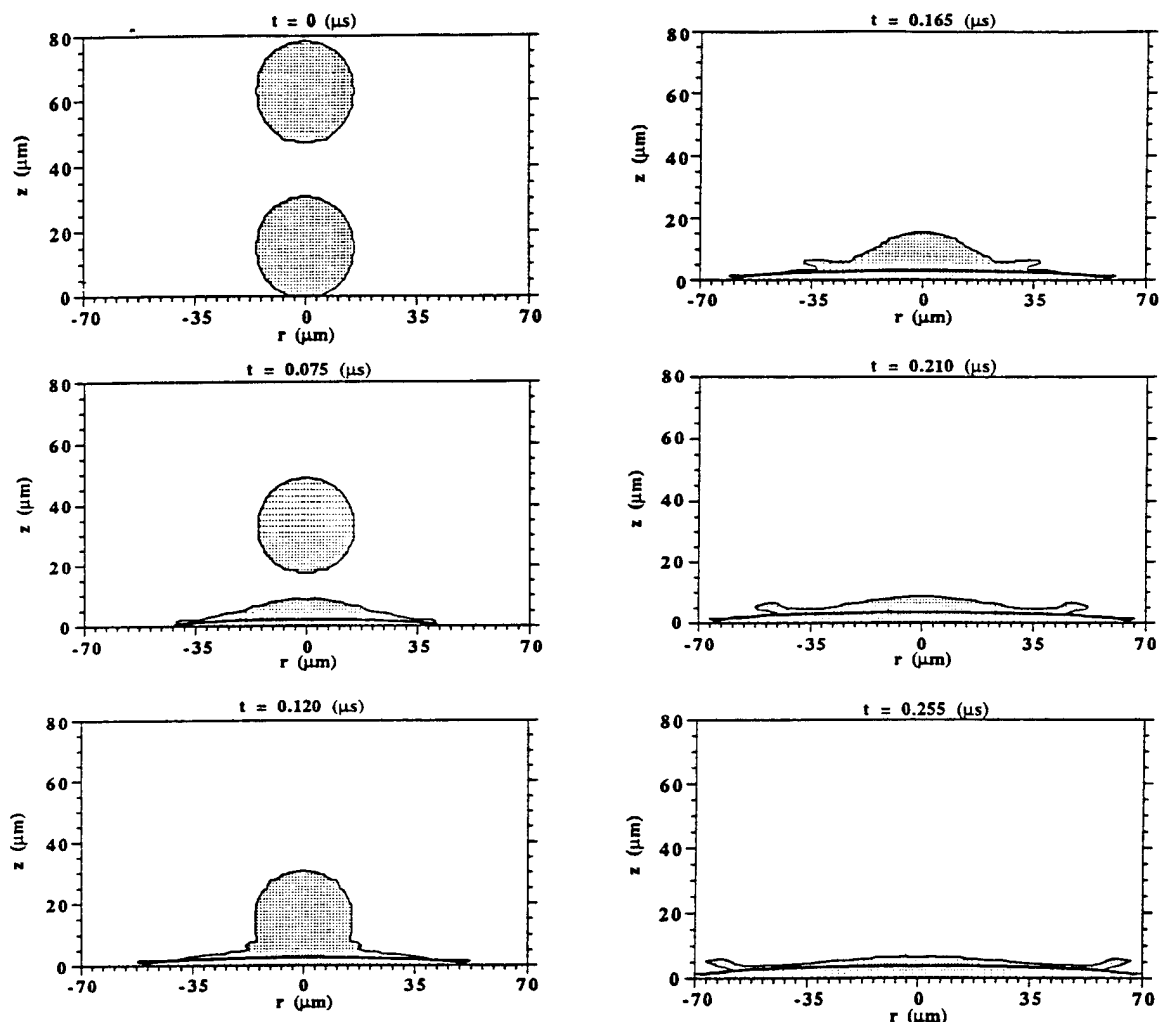


Figure 33 Deformation and solidification sequence during interaction of two droplets in tandem;  $d_0 = 30 \mu\text{m}$ ,  $u_0 = 400 \text{ m/s}$ ,  $T_l = 3750 \text{ K}$ ,  $T_s = 1500 \text{ K}$ .

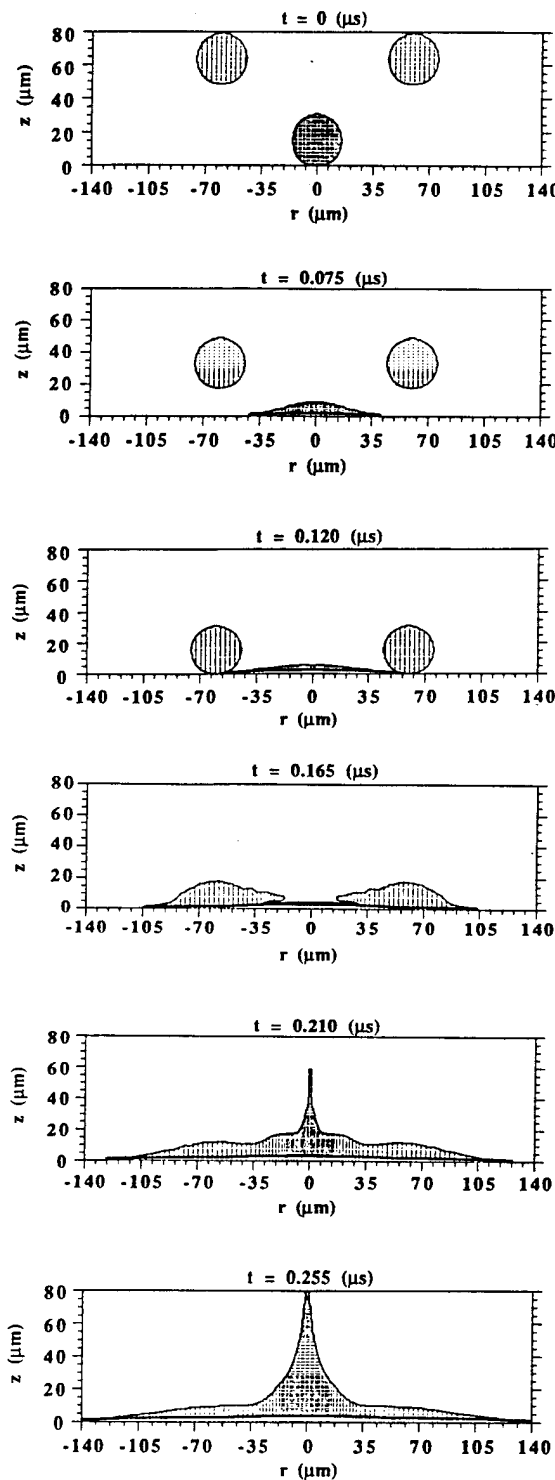


Figure 34. Deformation and solidification sequence during interaction of an axisymmetric toroidal ring and a droplet beneath it;  $d_0 = 30 \mu\text{m}$ ,  $u_0 = 400 \text{ m/s}$ ,  $T_l = 3750 \text{ K}$ ,  $T_s = 1500 \text{ K}$ .

### 5.2.6. Formation of Macro- and Micro-Pores During Deformation of Droplets On Non-Flat Surface

Figure 35 shows the deformation sequence of a single droplet impinging onto a solid particle on a substrate. As observed from Figure 35, the droplet liquid flows in good contact with the upper hemisphere of the particle upon impact, and separates from the lower hemisphere of the particle when  $t > 0.060 \mu\text{sec}$ . Beyond this time point, break-up of the liquid occurs. When the liquid impacts onto the substrate surface (for example at  $t > 0.120 \mu\text{sec}$ ), it forms two lateral sheet jets, one rushes outwards and the other inwards toward the symmetry axis ( $t = 0.210 \mu\text{sec}$ ). The inwards flowing liquid consumes most of its kinetic energy due to the viscous shear stress and wall adhesion forces when it reaches the corner between the particle and the substrate ( $t \geq 0.21 \mu\text{sec}$ ). The flow then changes its direction due to stagnation at the corner. However, it is evident that this corner will never be completely filled by the liquid as a result of the reduced kinetic energy and the further break-up of the liquid (compare  $t = 0.210 \mu\text{sec}$  to  $t = 0.345 \mu\text{sec}$ ). In addition, the numerical simulation of the heat transfer and solidification phenomena [132] revealed that solidification of a liquid splat is completed within a time of  $0.23 \mu\text{sec}$  at an initial impact velocity of  $400 \text{ m/sec}$ . Therefore, solidification will further prevent the voids in the corner from being filled by the liquid. The voids eventually develop into large pores, which reduce density and deteriorate bonding among as-sprayed deposits or coatings. In view of the size scale of these pores with respect to the droplet size, we refer to them hereafter as macro-pores, in order to distinguish these from the micro-pores which develop as a result of the separation phenomenon and the interactions of vortices described above.

Figure 36 shows the deformation sequence of an axisymmetric toroidal liquid ring impinging onto a substrate with a solid particle. The ring liquid spreads uniformly in the radial direction upon impact onto the substrate ( $t > 0.060$  to  $t = 0.120 \mu\text{sec}$ ). When the inwards flowing liquid reaches the particle surface, a portion of liquid rebounds upwards and breaks up subsequently, while the remaining liquid fills in the corner between the particle and the substrate during the spreading of the ring splat ( $t = 0.120$  to  $t = 0.210 \mu\text{sec}$ ). At this impact velocity, no macro-voids will form in the corner between the particle and the substrate. A comparison of this result to that in Figure 35 suggests that increasing the fraction of liquid droplets in the spray is of critical importance for reducing the macro-porosity.

Figure 37 shows the deformation sequence of an axisymmetric toroidal liquid ring, co-existing in the same space level with a droplet at the symmetry axis, and impinging onto a solid particle on a substrate. At  $t < 0.060 \mu\text{sec}$ , the spreading behavior is essentially same as those illustrated in Figures 35 and 36. From  $t \geq 0.120 \mu\text{sec}$ , the interactions between the downwards flowing droplet liquid and the inwards flowing ring liquid, as well as the upwards rebounding ring liquid, cause

the formation of ring-like vortices. The rebounding liquid breaks up subsequently ( $t = 0.210 \mu\text{sec}$ ). If solidification occurs at  $t \geq 0.210 \mu\text{sec}$ , some micro-pores may form as a result of this type of interactions among multiple droplets.

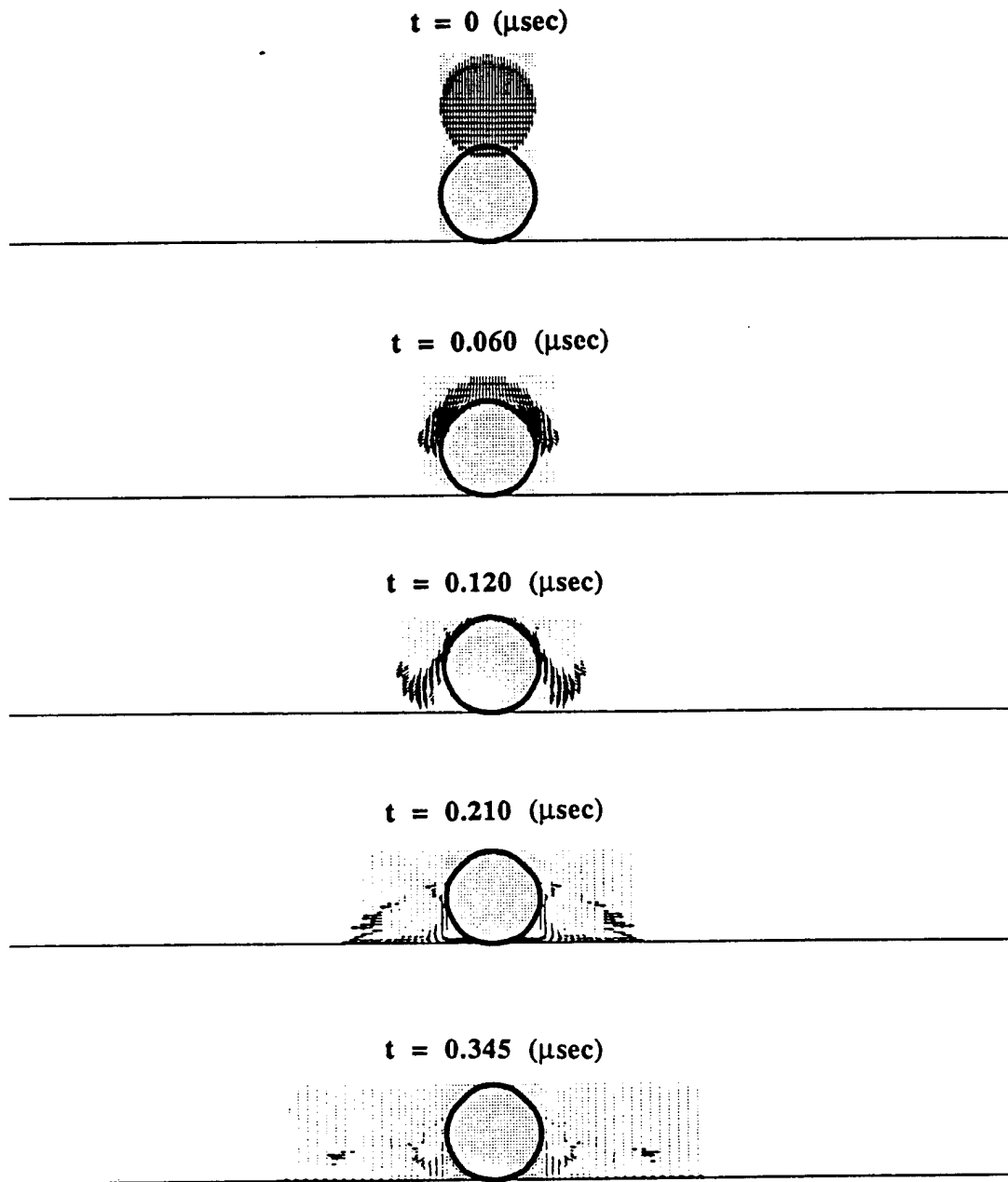


Figure 35. Deformation sequence of a single droplet impinging onto a solid particle on a substrate( $d_0=30 \mu\text{m}$ ;  $u_0=400 \text{ m/sec}$ ;  $\text{Re}=76229$ ;  $\text{We}=33897$ ).

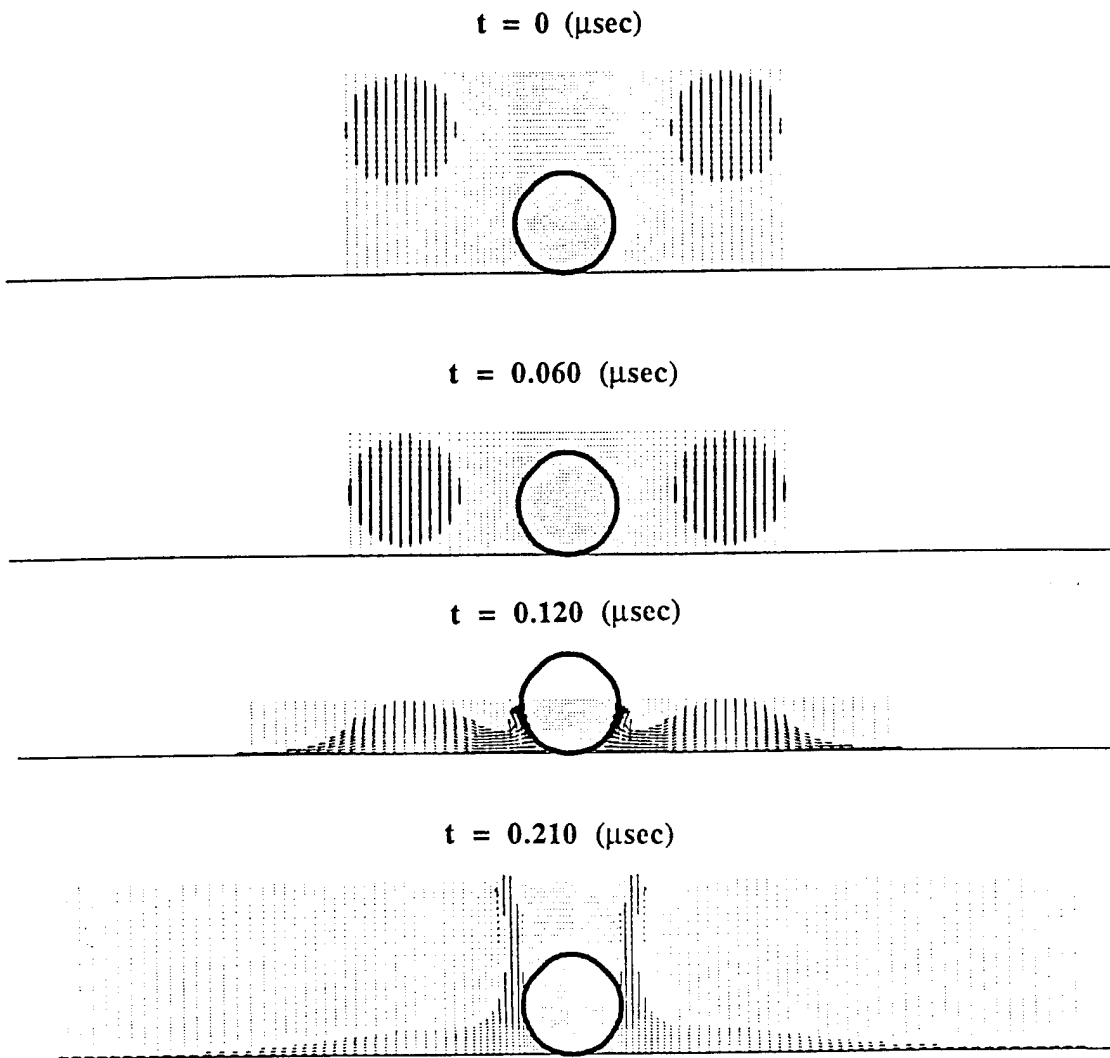


Figure 36. Deformation sequence of an axisymmetric toroidal liquid ring impinging onto a solid particle on a substrate ( $d_0=30\text{ }\mu\text{m}$ ;  $u_0=400\text{ m/sec}$ ;  $\text{Re}=76229$ ;  $\text{We}=33897$ ).

Figure 38 shows the deformation sequence of an axisymmetric toroidal liquid ring, co-existing in the same space level with a droplet at the symmetry axis, and impinging onto a solid particle ring on a substrate. During impingement, the break-up of the liquid occurs at an earlier time ( $t = 0.060\text{ }\mu\text{sec}$ ). The subsequent interactions between the droplet and the ring liquid lead to the formation of inner micro-pores when  $t \geq 0.120\text{ }\mu\text{sec}$ . Under this surface condition, it is also difficult to avoid the formation of the macro-pores as a result of the increased fraction of solid particles in the spray (more solid particles arrive on the substrate surface). These results reveal that the fraction of unmelted particles in plasma spraying or solidified particles in spray deposition processing is a significant factor influencing the spreading behavior of droplets and the formation of micro- and

macro-porosity among deposits. Since these solid particles essentially do not deform or flatten only to a small extent during impact, they will effectively increase porosity and reduce bonding among deposits or between coatings and substrate. These results are consistent with related experiments. Jackson, et al. [32], for example, note that incomplete melting of coarse W powders leads to excessive porosity in plasma sprayed W. It should be indicated that the flow patterns shown at the top in this figure result from the limit of the calculation domain, where the liquid flow reaches the top boundary and hence changes its direction from vertical upwards to lateral outwards due to the free-slip condition. Therefore, the flow patterns in this region are not representative of any physical processes during thermal spraying.

The surface conditions used in the above-described calculations represent some extreme cases where solid particles do not deform at all upon impact. Microstructural studies on sprayed deposits (for example in [139, 140]) demonstrate that in spray deposition processing, particularly in plasma

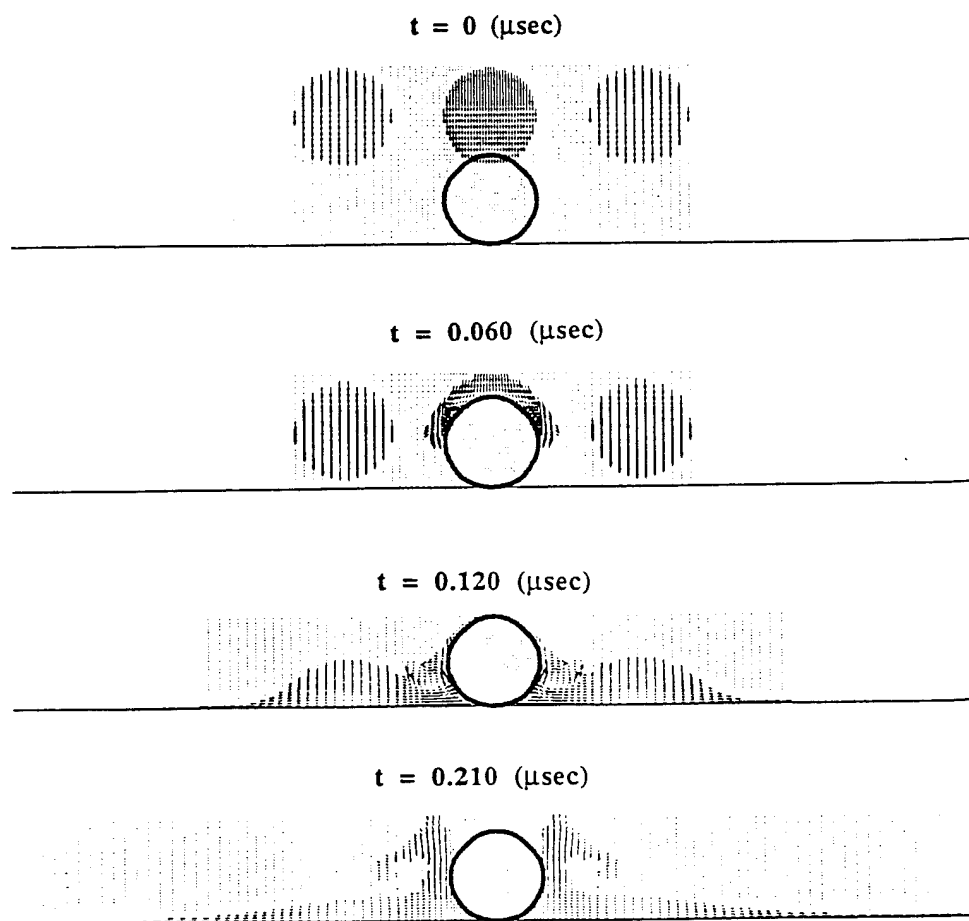


Figure 37. Deformation sequence of an axisymmetric toroidal liquid ring, co-existing in the same space level with a droplet at the symmetry axis, and impinging onto a solid particle on a substrate ( $d_0=30 \mu\text{m}$ ;  $u_0=400 \text{ m/sec}$ ;  $\text{Re}=76229$ ;  $\text{We}=33897$ ).

spraying, the deposition surface generally exhibits a non-flat, rough morphology in a microscopic scale, typified of a wave-like geometry, which may be characterized with a sinusoidal form surface pattern. In the following, we present and discuss the calculated results for this type of surface geometry condition.

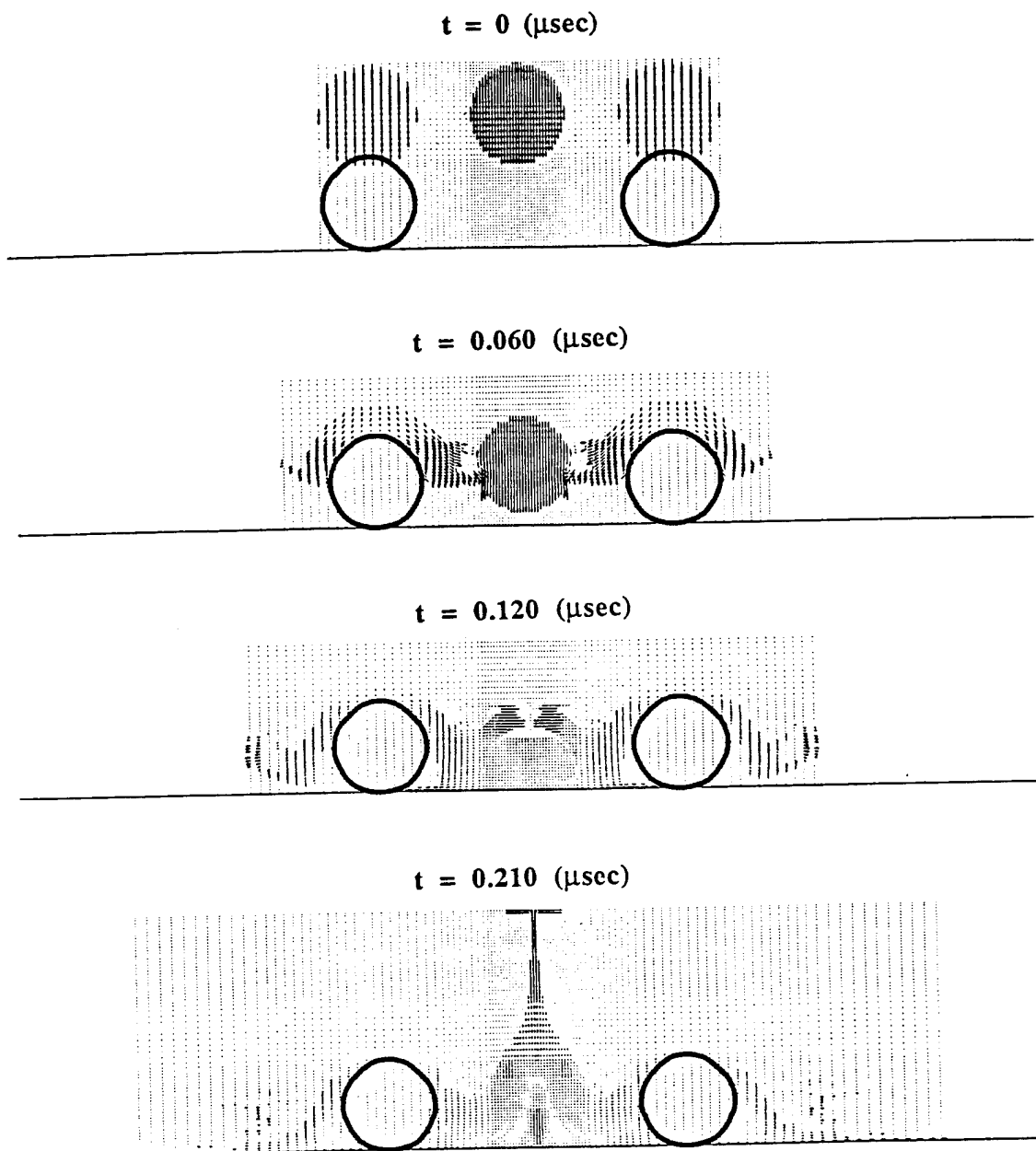


Figure 38. Deformation sequence of an axisymmetric toroidal liquid ring, co-existing in the same space level with a droplet at the symmetry axis, and impinging onto two solid particles on a substrate ( $d_0=30 \mu\text{m}$ ;  $u_0=400 \text{ m/sec}$ ;  $\text{Re}=76229$ ;  $\text{We}=33897$ ).

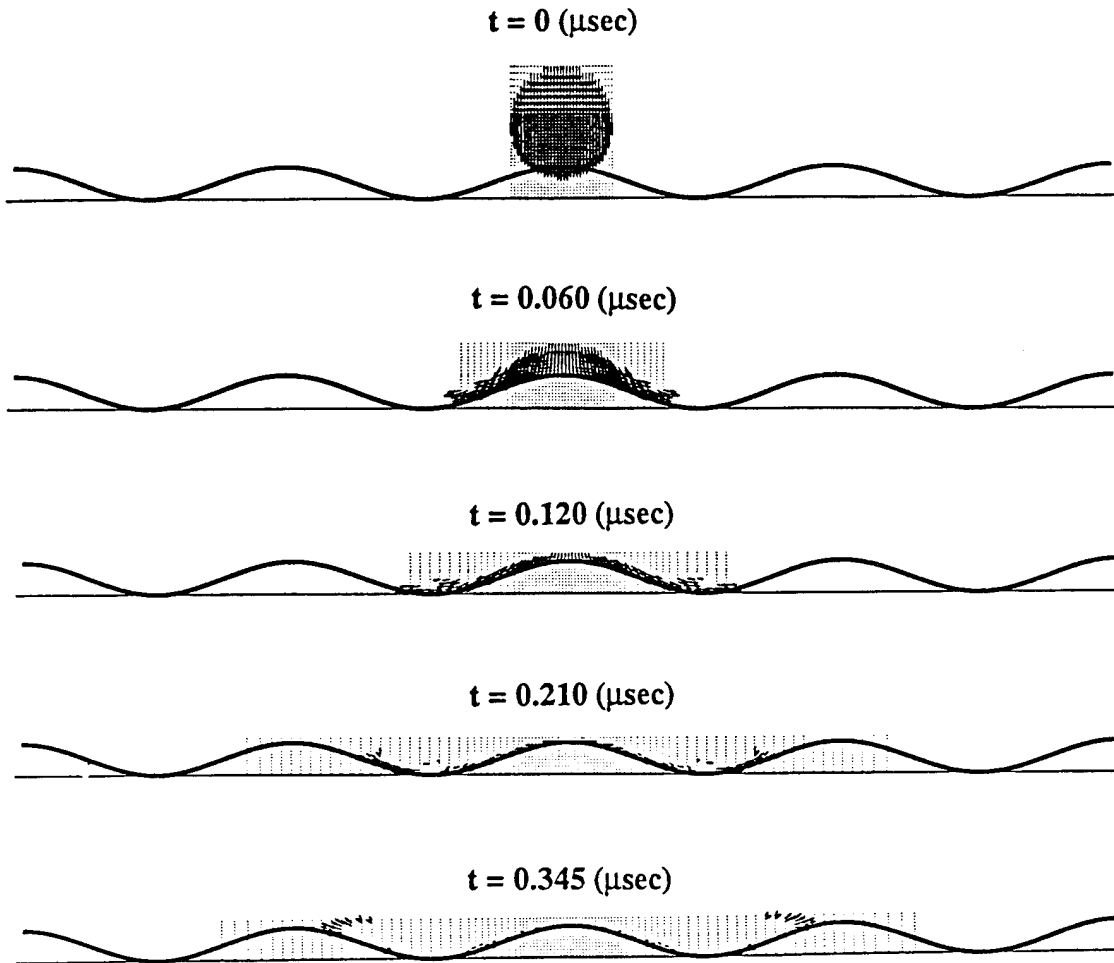


Figure 39. Deformation sequence of a single droplet impinging onto a solid, waved surface layer on a substrate ( $d_0=30\text{ }\mu\text{m}$ ;  $u_0=400\text{ m/sec}$ ;  $\text{Re}=76229$ ;  $\text{We}=33897$ ;  $\varepsilon/d_0=0.33$ ;  $\lambda/d_0=2.8$ ).

Figure 39 shows the deformation sequence of a single droplet impinging onto a solid, waved surface layer on a substrate. The spreading behavior is distinctly different from that on a solid flat substrate or on a solid particle discussed above. The droplet does not splash upwards at impact, but instead spreads in the radial direction and in a relatively good contact with the waved surface. With increasing time, the splat height decreases and its diameter increases. Eventually, it becomes a very thin, non-flat splat. The break-up of the liquid begins at  $t = 0.060\text{ }\mu\text{sec}$ , and becomes significant only at  $t = 0.345\text{ }\mu\text{sec}$ . At this time, solidification is expected to be completed according to the numerical studies on the heat transfer and solidification in [132]. Therefore, no macro-pores form during the spreading of a droplet on this type of waved surface. This deformation behavior suggests that a better adhesion between the splat and the surface may be

obtained, in the sense of the even distribution of the liquid sheet (no macro-pores) and the good contact, if the roughness of the solid surface at impact is not as large as in Figure 35, and significant solidification begins after complete deformation. From this viewpoint, the waved surface condition is favorable relative to those involving some undeformed solid particles. These results further demonstrate the importance of the extent of droplet flattening to the ultimate microstructure and quality of spray processed materials.

Figure 40 shows the deformation sequence of an axisymmetric toroidal liquid ring, co-existing in the same space level with a droplet at the symmetry axis, and impinging onto a solid, waved surface layer on a substrate. Significant break-up of the liquid occurs at  $t \geq 0.120 \mu\text{sec}$ . Since the voids between the surface and the ejected liquid (in the fringe region,  $t = 0.120 \mu\text{sec}$ ) are still open to the flow of the liquid (not closed by solid or solidified materials), no macro-pores will be generated in this case. A comparison of the results under this surface condition to those in Figure 38 reveals that an improvement of the surface condition is helpful for reducing the porosity.

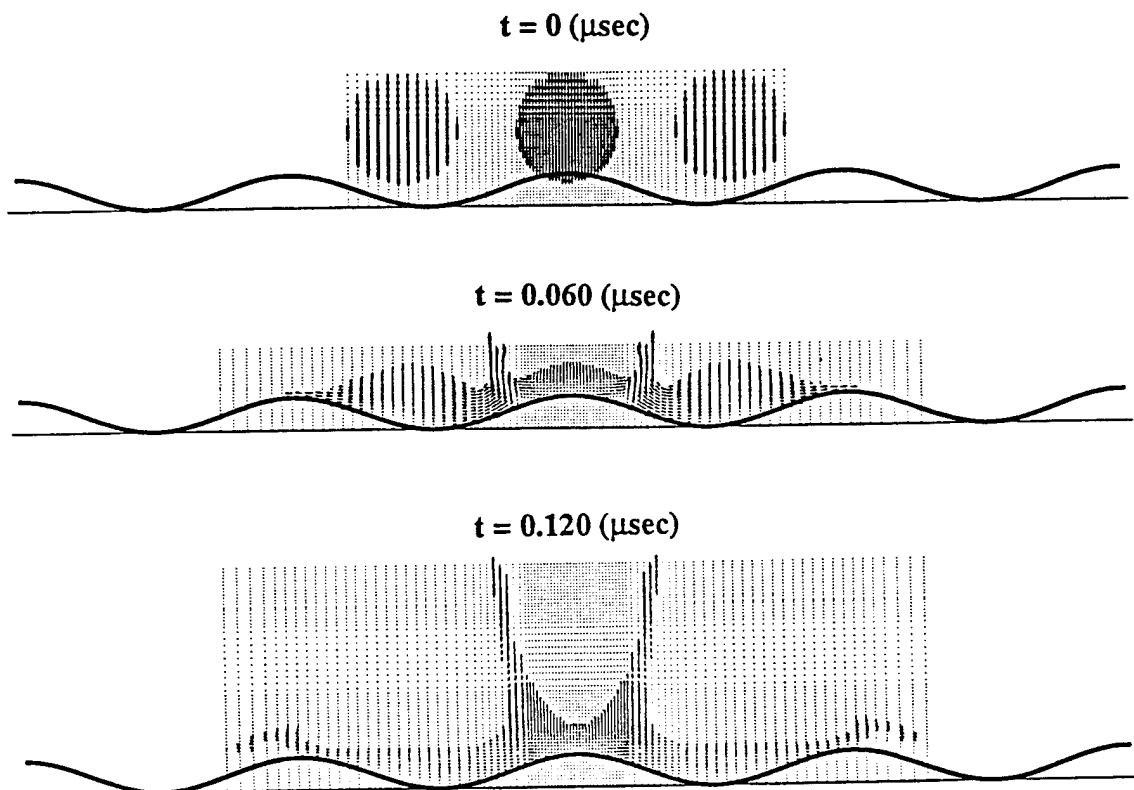


Figure 40. Deformation sequence of an axisymmetric toroidal liquid ring, co-existing in the same space level with a droplet at the symmetry axis, and impinging onto a solid, waved surface layer on a substrate ( $d_0=30 \mu\text{m}$ ;  $u_0=400 \text{ m/sec}$ ;  $\text{Re}=76229$ ;  $\text{We}=33897$ ;  $\varepsilon/d_0=0.33$ ;  $\lambda/d_0=2.8$ ).

Figure 41 shows the deformation sequence of a single droplet impinging onto a solid, waved surface layer on a substrate at an impact velocity lower than that in Figure 39. Comparing Figure 41 to Figure 39 reveals that the deformation behavior at the two impact velocities is essentially similar. As expected, the spreading of the droplet is slower at the lower impact velocity and the break-up of the liquid occurs at a later time.

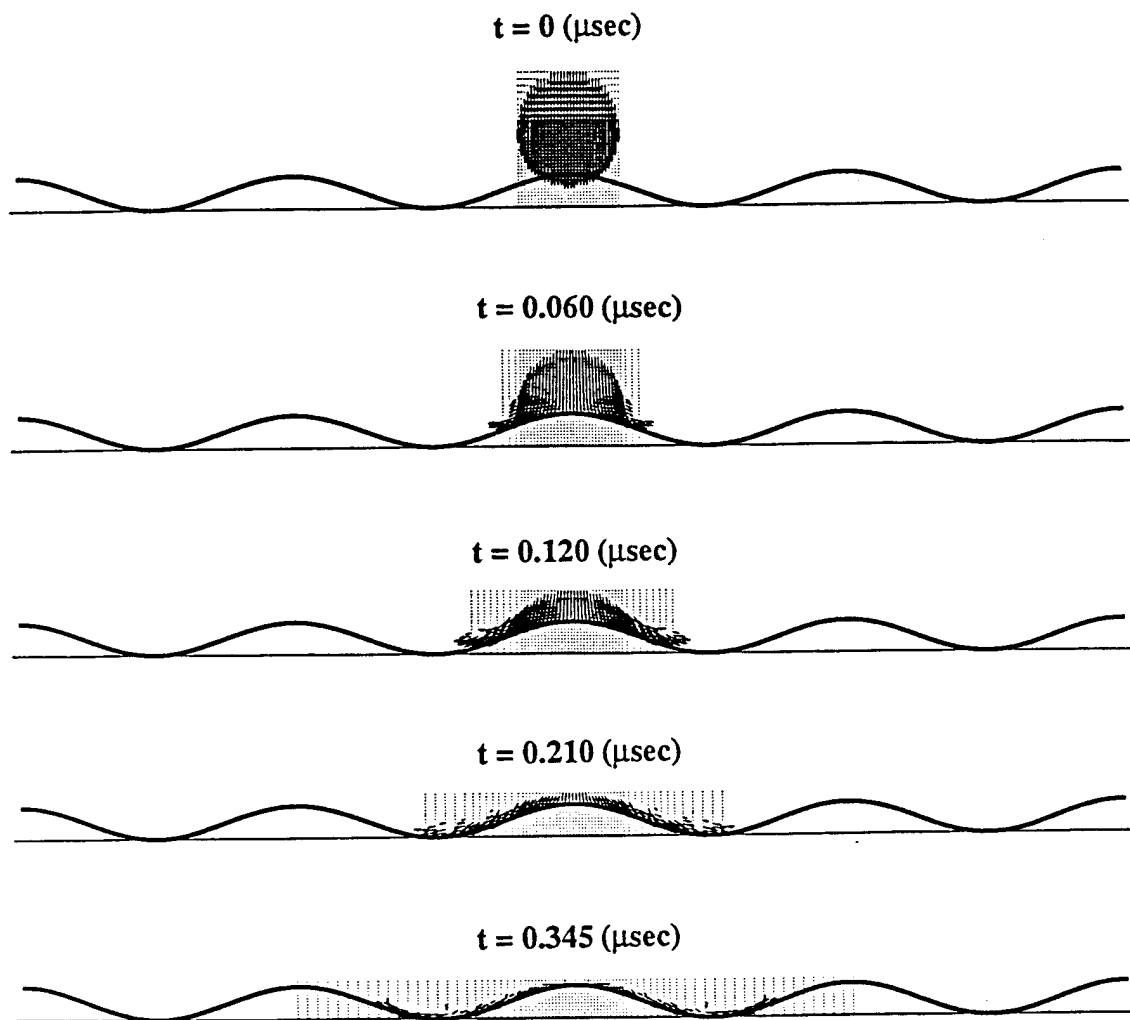


Figure 41. Deformation sequence of a single droplet impinging onto a solid, waved surface layer on a substrate ( $d_0=30 \mu\text{m}$ ;  $u_0=200 \text{ m/sec}$ ;  $\text{Re}=38115$ ;  $\text{We}=8474$ ;  $\epsilon/d_0=0.33$ ;  $\lambda/d_0=2.8$ ).

Figures 42 and 43 show the deformation sequence of a single droplet impinging onto a solid, waved surface layer on a substrate with a dimensionless roughness height of 0.66 and 1, respectively. Other calculation conditions are the same as those used for the results shown in

Figure 41. A comparison of the results shown in Figures 41, 42 and 43 indicates that the dimensionless roughness height critically influences the deformation behavior of droplets. An increase in the dimensionless roughness height leads to a decrease in the lateral projected diameter of the splat. In Figure 41, no voids exist in the vicinity of the surface; while in Figures 42 and 43, voids in the liquid above the surface are evident ( $t \geq 0.210 \mu\text{sec}$ ). These voids result from the break-up of the liquid and the concomitant entrapment of gas. The voids are surrounded by the liquid and will be closed to the flow when solidification occurs. Therefore, they may eventually develop into micro-pores. These results demonstrate the tendency that the extent of void formation increases with increasing dimensionless roughness height.

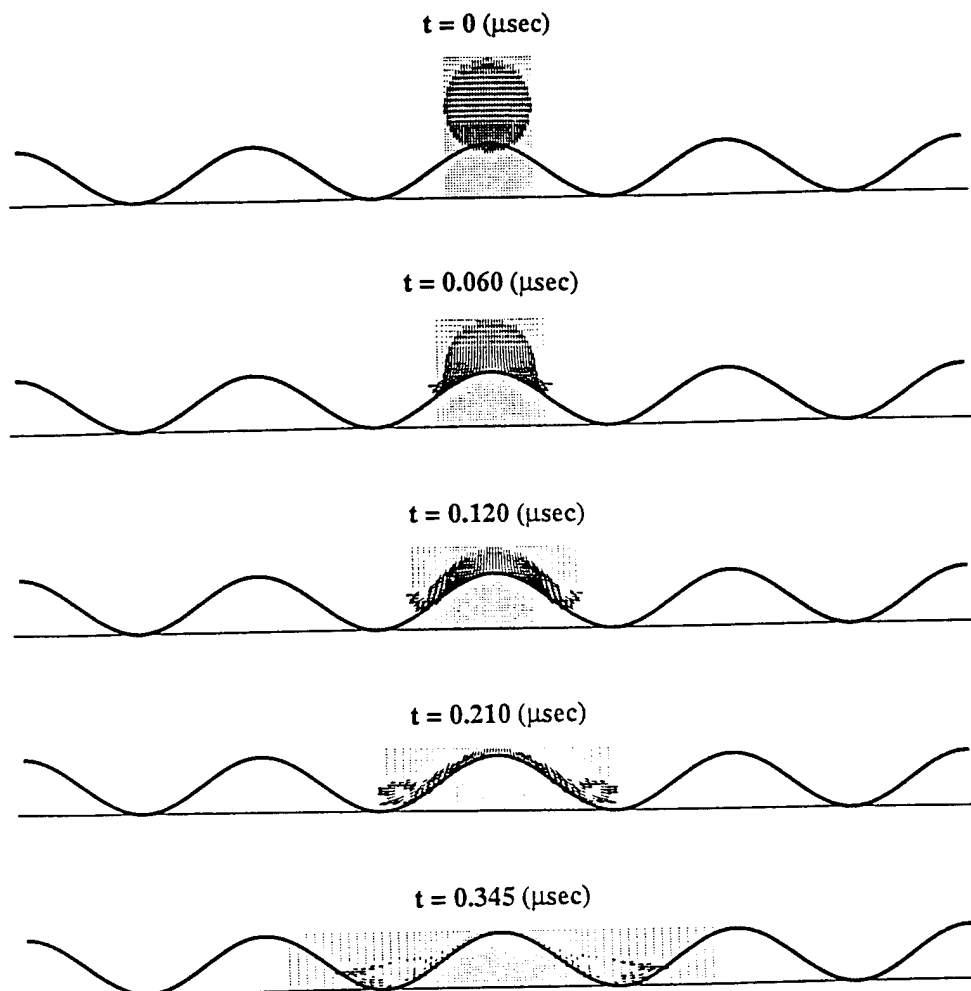


Figure 42. Deformation sequence of a single droplet impinging onto a solid, waved surface layer on a substrate ( $d_0=30 \mu\text{m}$ ;  $u_0=200 \text{ m/sec}$ ;  $\text{Re}=38115$ ;  $\text{We}=8474$ ;  $\varepsilon/d_0=0.66$ ;  $\lambda/d_0=2.8$ ).

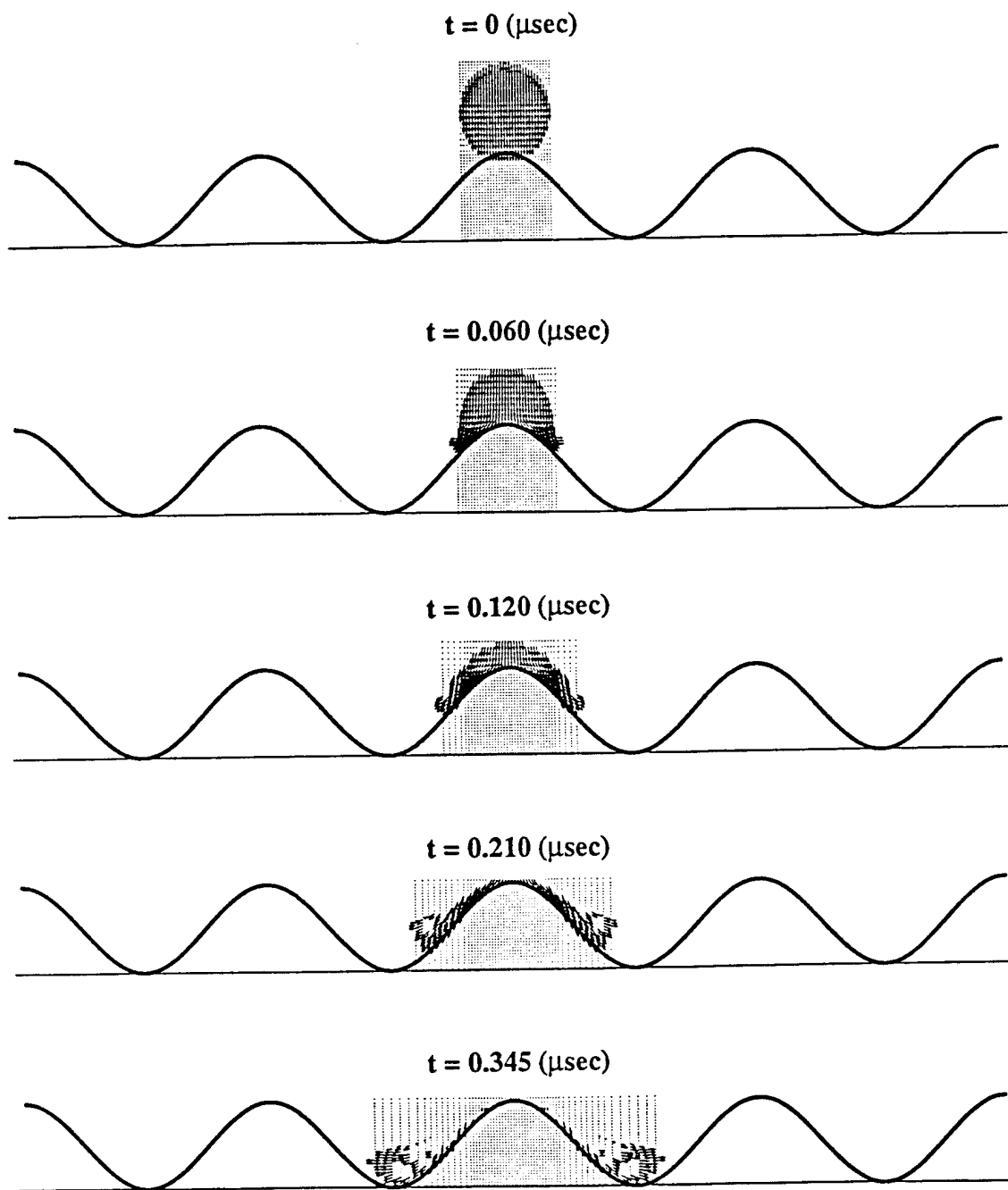


Figure 43. Deformation sequence of a single droplet impinging onto a solid, waved surface layer on a substrate ( $d_0=30 \mu\text{m}$ ;  $u_0=200 \text{ m/sec}$ ;  $\text{Re}=38115$ ;  $\text{We}=8474$ ;  $\varepsilon/d_0=1$ ;  $\lambda/d_0=2.8$ ).

## VI. MICROSTRUCTURE AND BEHAVIOR OF LOW PRESSURE PLASMA DEPOSITED SiC- REINFORCED MoSi<sub>2</sub>

### 6.1. Experimental Procedures

#### 6.1.1. Low Pressure Plasma Deposition of SiC- Reinforced MoSi<sub>2</sub>

The experimental procedure used in the investigation is described as follows. First, 15 µm SiC particles were premixed with MoSi<sub>2</sub> powders, ranging in size from 10 µm to 44 µm, in a V-shaped blender for approximately 60 minutes with a target composition of 20 vol.% SiC/MoSi<sub>2</sub>. Second, LPPS processing experiments were conducted at Electro-Plasma Inc. (Irvine, CA) using an EPI-LPPSTM system, capable of spraying a wide variety of materials under high deposition rates. A summary of the primary processing parameters used is shown in Table 10. A stainless steel plate with the following dimensions: 3.2 x 100 x 100 mm was used as the target substrate. The resultant LPPS SiC/MoSi<sub>2</sub> material, referred to hereafter simply as SiC/MoSi<sub>2</sub>, exhibited a discoidal geometry of approximately 10 mm in thickness. Third, the SiC/MoSi<sub>2</sub> material was sectioned and prepared for microstructural and mechanical characterization studies following established procedures.

Table 10. LPPS Processing Parameters Used to Prepare the SiC/MoSi<sub>2</sub> Composites

Plasma Unit	EPI-LPPS System
Plasma Gun	EPI-03CP
Voltage (Volts)	52
Current (Amps)	1400
Arc Gas Flow Rate - Ar (SLPM)	118
Second Gas - H <sub>2</sub> (SLPM)	12
Powder Gas Flow Rate - Ar (SLPM)	5
Powder Feed Rate (g/min)	30
Spray Distance (mm)	200
Atmosphere (Pa)	3x10 <sup>4</sup>

Optical microscopy was conducted on polished and etched SiC/MoSi<sub>2</sub>. The samples were etched with: 2 parts HNO<sub>3</sub>, 1 part HF, and 4 parts H<sub>2</sub>O. The density of the material was determined on as-spray-deposited samples utilizing Archimedes' principle. This procedure involved weighing a polished cube using a Fisher Scientific Balance with an accuracy of ± 0.0001 g, and using Ethylene glycol as the fluid.

### 6.1.3. Fracture Toughness

Microhardness indentation measurements were conducted on a Buehler Micromet® Digital Microhardness Tester with a load of 9.8 N. The room temperature fracture toughness was determined on the basis of the indentation fracture toughness technique as described in detail elsewhere [141, 142].

### 6.1.4. Creep Testing

The specimens used in this investigation were rectangular parallelepipeds with a ratio of height to width of approximately 2:1 with dimensions of a typical sample being 3.0 x 3.0 x 6.0 mm. The specimens were tested in a temperature range from 1100 to 1500°C under compression in air. The load was applied parallel to the spray direction (SD). Steady-state creep rates were measured at stresses ranging from approximately 10 to 100 MPa. In addition, some samples were deformed with the load applied perpendicular to the spray direction (PSD). After deformation, samples were cooled rapidly under load to preserve the structure developed during creep. The microstructure of the deformed samples was examined using optical microscopy.

## 6.2. Results and Discussion

### 6.2.1. Density and Porosity of Low Pressure Plasma Deposited SiC- Reinforced MoSi<sub>2</sub>

Table 11 shows the results obtained from the density and porosity measurements. Interestingly, the density of the plasma-sprayed SiC/MoSi<sub>2</sub> (5.79 g/cm<sup>3</sup>) is apparently higher than the theoretical density corresponding to a 20 vol.% SiC-reinforced MoSi<sub>2</sub> composite (5.69 g/cm<sup>3</sup>). It is well established that SiC is readily vaporized by a thermal plasma, and moreover SiC particles, due to their low density, are readily dragged by the plasma stream. These two factors lead to a significant loss of SiC during plasma spraying, and therefore are thought to be responsible for the observed density difference. The theoretical density of the plasma sprayed material was determined based on the assumption that only MoSi<sub>2</sub> (6.31 g/cm<sup>3</sup>), SiC (3.21 g/cm<sup>3</sup>), and porosity are present in the composite, and that no oxides, such as MoO<sub>3</sub> (4.69 g/cm<sup>3</sup>) and SiO<sub>2</sub> (2.27~2.65 g/cm<sup>3</sup>) are formed. Under these assumptions, the theoretical density of the plasma-sprayed SiC/MoSi<sub>2</sub> is 6.04 g/cm<sup>3</sup> and thus, the amount of SiC present in the composite is 8.71 vol.%. The latter result is consistent with the previous suggestion that a significant amount of SiC was lost

Table 11. Density Characteristics

As-Sprayed Specimen Density	5.787 g/cm <sup>3</sup>
Open Porosity	3.55%
Closed Porosity	0.66%
Total Porosity	4.21%
Theoretical Density of 20 vol.% SiC/MoSi <sub>2</sub>	5.690 g/cm <sup>3</sup>

during plasma spraying, since the initial target composition was 20 vol.%. The loss of SiC may be minimized by utilizing multiple plasma guns.

#### 6.2.2. Microstructure of Low Pressure Plasma Deposited SiC- Reinforced MoSi<sub>2</sub>

The microstructure of the plasma-sprayed SiC/MoSi<sub>2</sub> composite is shown in Figures 44(a) and (b), in the longitudinal and transverse directions, respectively. Some of the pores that are evident in this micrograph may be attributed to SiC pullout during polishing. The wavy microstructure shown in Fig. 44(b) is representative of the transverse direction (perpendicular to spray direction), and suggests that the molten SiC/MoSi<sub>2</sub> droplets arrived at the deposition surface in a fully liquid condition, eventually spreading in the transverse direction. The presence of well-defined inter-particle interfaces suggests that the plasma sprayed droplets did not experience re-melting after deposition, consistent with the findings of Castro et al. [40]. Moreover, the relatively equiaxed morphology of the SiC particles that are observed in the sprayed microstructure suggests that these particles were partially re-melted during spraying. Besides MoSi<sub>2</sub> and SiC, no other phases were detected by optical microscopy.

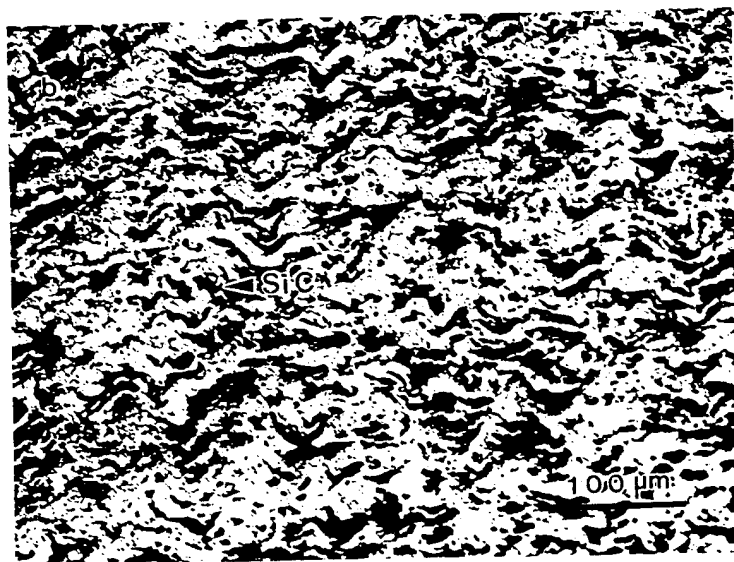
#### 6.2.3. Fracture Toughness of Low Pressure Plasma Deposited SiC- Reinforced MoSi<sub>2</sub>

The Vickers microhardness measurements were conducted at room temperature, and the corresponding fracture toughnesses were determined according to the following procedure. First, ten indentations were made in both the longitudinal direction and transverse directions. Second, the crack length and impression diagonal were measured and converted into fracture toughness, K<sub>C</sub>, on the basis of the following equation [141, 142]:

$$K_C = C_V^R (E/H)^{1/2} (P/c_o)^{3/2} \quad (30)$$



(a)



(b)

Figure 44. Microstructure of the plasma-sprayed SiC/MoSi<sub>2</sub> composite; (a) longitudinal direction (parallel to spray direction), and (b) transverse direction (perpendicular to spray direction).

where  $C_V^R$  is a material-independent constant for Vickers-produced radial cracks. E is Young's modulus, H is hardness, P is peak load, and  $c_0$  is the crack dimension. The results of these measurements, summarized in Table 12, revealed a significant improvement in the fracture toughness of the plasma-sprayed SiC/MoSi<sub>2</sub> composite (4.39 MPam<sup>1/2</sup>) relative to that generally reported for monolithic MoSi<sub>2</sub> (2.58 MPam<sup>1/2</sup>, [[143]]). The higher fracture toughness of the SiC/MoSi<sub>2</sub> may be attributed to a SiC toughening mechanism, since it is well-known that crack deflection plays an important role in the toughening of SiC/MoSi<sub>2</sub> [37]. The values of fracture toughness obtained, however, are lower than those reported by Gac and Petrovic [34] for 20 vol.% SiCwhisker/MoSi<sub>2</sub> composites processed by powder metallurgy (8.2 MPam<sup>1/2</sup>). The observed difference between the fracture toughness values observed herein, and those reported by Gac and Petrovic [34] may be attributed to the lower volume fraction of SiC in the LPPS composite and the difference in particle morphology (particulate vs. whisker).

Table 12. Microhardness and Fracture Toughness for the Plasma-Sprayed SiC/MoSi<sub>2</sub> Composites

Test Condition	Average Hardness (VHN)	Average Fracture Toughness, MPam <sup>1/2</sup>
Longitudinal Direction	1158±72	4.60
Transverse Direction	1140±82	4.17

It is worth noting that, unlike the results from earlier studies on plasma-sprayed Ta<sub>particle</sub>/MoSi<sub>2</sub> in which preferential cracking was observed through splat interfaces [40] no preferential cracking was evident in the plasma-sprayed SiC/MoSi<sub>2</sub>. Moreover, the observed small difference in fracture toughness between the longitudinal and transverse orientations (4.17 vs. 4.60) provides further support to the suggestion that the plasma sprayed particles were well bonded. In comparison, Castro et al. [40] reported a difference of about 2.5 MPam<sup>1/2</sup> between the longitudinal and transverse orientations for plasma-sprayed Ta/MoSi<sub>2</sub>.

#### 6.2.4. Creep Behavior of Low Pressure Plasma Deposited SiC- Reinforced MoSi<sub>2</sub>

The dependence of the steady-state creep rate,  $\dot{\epsilon}$ , on the applied stress,  $\sigma$ , for the plasma-sprayed SiC-reinforced MoSi<sub>2</sub> at five temperatures (1100, 1200, 1300, 1400 and 1500°C) is shown in Figure 45. The data in Figure 45 are plotted as logarithm of steady-state creep rate versus logarithm of true stress. The slope of the curves is the stress exponent, n. From Figure 45 it can be observed that the stress exponent decreases with increasing temperature. The relationship

between the stress exponent and testing temperature is shown in Figure 46. A drop in the stress exponent is observed in the vicinity of 1300°C;  $n \sim 2.6$  at 1100°C and  $n \sim 1.4$  at 1500°C. At high temperatures the stress exponent  $n \sim 1.5$  combined with the microstructural observations of no change in grain shape suggested grain boundary sliding as the dominant deformation mechanism in this region. The presence of an amorphous silica phase can help grain boundary sliding by acting as a lubricant to assist intergranular or interfacial sliding or as a high diffusivity path. Examination of the Si-O phase diagram indicates that melting can occur at temperatures lower than 1400°C [144]. In the low temperature region ( $T < 1300^\circ\text{C}$ ) the stress exponent ( $n \sim 2.6$ ) is in good agreement with the values ( $n \sim 2.6$  to 3.2) observed for powder metallurgy (PM) fabricated SiC-reinforced MoSi<sub>2</sub> tested in a similar temperature range (1100-1300°C) [145-150]. A stress exponent of 3 is typically associated with creep controlled by a dislocation mechanism [151-153].

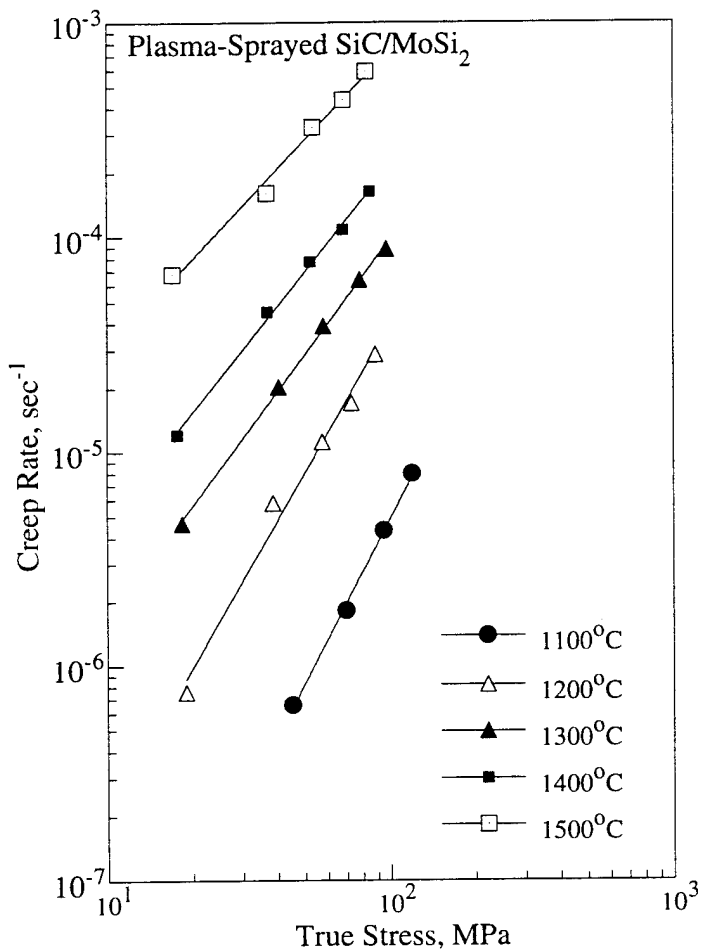


Figure 45. Steady-state creep rate vs. true stress for plasma-sprayed SiC/MoSi<sub>2</sub> at various temperatures

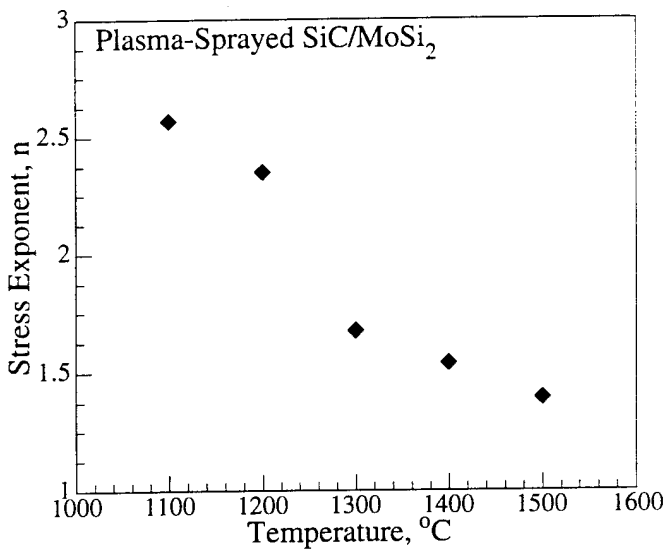


Figure 46. Temperature dependence of the stress exponent.

The activation energy for creep,  $Q$ , in the low temperature ( $T < 1300^\circ\text{C}$ ) and high stress exponent region ( $n \sim 2.4$  to 2.6) and high temperature ( $T > 1300^\circ\text{C}$ ) and low stress exponent region ( $n \sim 1.4$  to 1.6) was determined from a plot of logarithm steady-state creep rate versus inverse temperature at constant stress. Figure 47 is such a plot at different stress levels. The activation energy for creep from the slope of the straight lines is equal to  $300 \text{ kJmol}^{-1}$  ( $T < 1300^\circ\text{C}$ ) and  $190 \text{ kJmol}^{-1}$  ( $T > 1300^\circ\text{C}$ ). The activation energy for creep in both regions is essentially independent of stress. The change in the activation energy for creep at  $T \sim 1300^\circ\text{C}$  implies a change in the rate-controlling process. The higher value of the activation energy for creep of  $300 \text{ kJmol}^{-1}$  for the plasma-sprayed  $\text{SiC}/\text{MoSi}_2$  is at the low end of values reported ( $300$ – $600 \text{ kJmol}^{-1}$ ) for PM  $\text{MoSi}_2$  and PM  $\text{SiC}/\text{MoSi}_2$  in a similar temperature ( $1100$ – $1300^\circ\text{C}$ ) and stress exponent ( $n \sim 3$ ) range [145–150]. The lower value of the activation energy for creep of  $190 \text{ kJmol}^{-1}$  when compared to the higher value and with other values ( $300$ – $600 \text{ kJmol}^{-1}$ ) would suggest that this activation energy value is related to the activation energy for grain boundary diffusion, most likely as a result of high diffusivity path in the amorphous silica phase along the  $\text{MoSi}_2$  grain boundaries. The results of Figs. 45, 46 and 47 confirm that a change in the rate-controlling creep mechanism occurs in plasma-sprayed  $\text{SiC}/\text{MoSi}_2$  as the testing temperature is varied. At  $T < 1300^\circ\text{C}$ , the activation energy for creep of approximately  $300 \text{ kJmol}^{-1}$  and stress exponent of 2.5 is most likely due to dislocation motion controlled by lattice diffusion whereas at  $T > 1300^\circ\text{C}$  the activation energy for creep of  $190 \text{ kJmol}^{-1}$  and stress exponent of 1.5 are related to grain boundary sliding controlled by

grain boundary diffusion. The change in the rate-controlling process may be related to the softening or melting of an amorphous intergranular silica phase at temperatures about 1300°C. This suggestion is further verified by an examination of the microstructure of the deformed samples at  $T < 1300^\circ\text{C}$  and  $T > 1300^\circ\text{C}$  as shown in Figure 48. Figure 48a is for a specimen tested at 1200°C ( $n \sim 2.4$ ), whereas Figure 48b is for a specimen tested at 1500°C ( $n \sim 1.4$ ). From Figure 48a it is observed that severe grain boundary cracking has occurred, whereas in Figure 48b no grain boundary cracks are observed. At high temperatures ( $T > 1300^\circ\text{C}$ , Figure 48a) the amorphous silica grain boundary phase can flow to accommodate the deformation. At low temperatures ( $T < 1300^\circ\text{C}$ , Figure 48b) the glass phase is too rigid to help accommodate the deformation and thus, grain boundary fracture occurs.

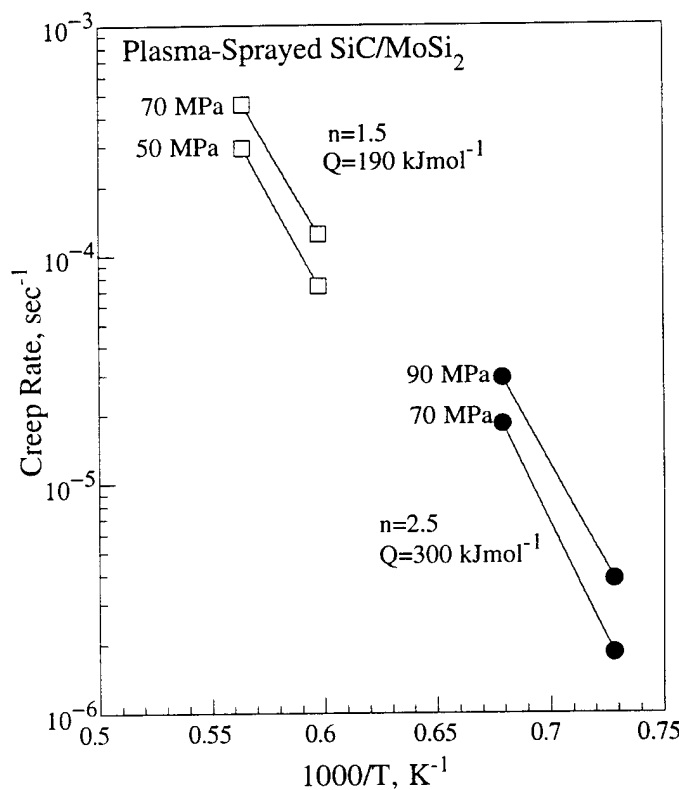


Figure 47. Creep rate versus reciprocal absolute temperature for plasma-sprayed  $\text{SiC}/\text{MoSi}_2$ .

The effect of orientation on the creep behavior of plasma-sprayed  $\text{SiC}/\text{MoSi}_2$  was also studied in the low temperature ( $T < 1300^\circ\text{C}$ ) and high temperature ( $T > 1300^\circ\text{C}$ ) regions. The results are shown in Fig. 49. From Fig. 49 two important points are noted. First, a decrease in the stress

exponent occurs for the PSD (perpendicular to the spray direction) material from 1.4 to 2.3 as the testing temperature is decreased from 1500 to 1200°C. This trend is in good agreement with the results shown in Fig. 45 and Fig. 46 for the SD (spray direction) material. The stress exponents for both the PSD and SD materials are the same at 1200°C ( $n \sim 2.3$  to 2.4) and 1500°C ( $n \sim 1.4$ ). Second, the creep rates at a given value of applied stress are in excellent agreement at 1500°C and within a factor of 1.5 at 1200°C for the two orientations. The absence of an orientation effect on the creep rate in the high temperature region ( $n \sim 1.5$ ) is in agreement with a grain boundary sliding mechanism. The orientation dependence of the creep rate in the low temperature region ( $n \sim 2.5$ ) is consistent with creep controlled by intragranular dislocation motion.

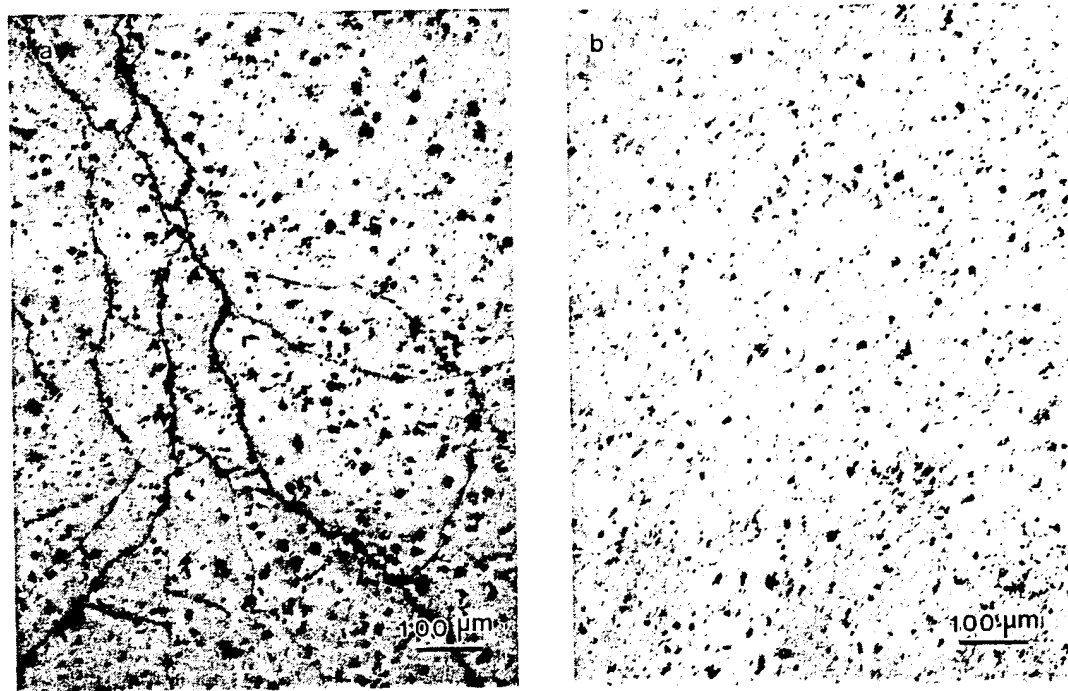


Figure 48. Microstructure of plasma-sprayed SiC/MoSi<sub>2</sub> after creep testing at (a) 1200°C and (b) 1500°C.

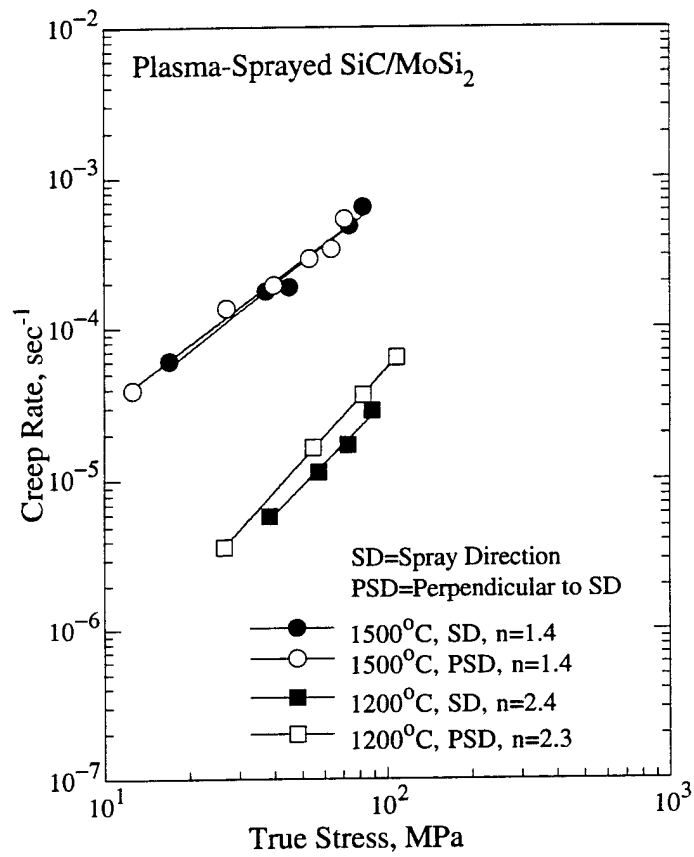


Figure 49. Creep behavior as a function of orientation at 1200°C and 1500°C.

## VII. HIGH TEMPERATURE DEFORMATION BEHAVIOR OF 6061 ALUMINUM ALLOY AND SiC<sub>p</sub> PARTICULATE REINFORCED 6061 ALUMINUM ALLOY

### 7.1. Experimental Procedures

The materials used in this investigation were 6061 aluminum and 30 vol% SiC<sub>p</sub>-6061 aluminum composite. Both materials, which were supplied by Army Materials Technology Laboratory (AMTL), were prepared by powder metallurgy techniques and was received in the extruded condition. The 6061 aluminum alloy contained the following elements: 1 wt% Mg, 0.6 wt% Si, 0.28 wt% Cu, 0.2 wt% Cr, and the Balance is Al.

Double-shear specimens [154] of shape and dimension described elsewhere [155] were machined from PM 6061 Al and SiC<sub>p</sub>-6061 Al. The advantages of using the double shear configuration were given elsewhere [155-157]. Prior to testing, the specimens were solutionized at 723k in argon for 4h, water quenched, and left at room temperature for a minimum of 1 week. The spatial grain size, d, was measured at  $15\pm4 \mu\text{m}$  by using  $d=1.74 \bar{L}$ , where  $\bar{L}$  is a mean linear intercept grain size. The sections perpendicular to the extrusion axis were examined metallographically by using a mixture of HF and H<sub>2</sub>O(HF:H<sub>2</sub>O=10 ml: 90 ml).

The creep tests were conducted on a suitably designed creep-testing machine operating at a constant load. The tests were conducted in air at 648 and 678K using a three-zone furnace in which the temperature was monitored and maintained constant to within  $\pm 2\text{K}$ . Steady-state creep rates were measured in the range of  $10^{-7} - 10^{-1} \text{ s}^{-1}$ . The strain during creep was measured with a linear variable differential transformer (LVDT) and amplifier, and monitored directly on a strip chart recorder.

### 7.2. Results and Discussions

#### 7.2.1. Creep Curves of SiC<sub>p</sub>-6061 Al and 6061 Al

Figure 50 represents typical creep curves for the composite and the alloy. The creep curves of both materials show a normal primary stage, where  $d\dot{\gamma}/dt < 0$ , a secondary stage, where  $d\dot{\gamma}/dt = 0$ , and a tertiary stage, where  $d\dot{\gamma}/dt > 0$ . Despite this similarity in the shape of creep curve, the total strain to failure in the alloy is found to be larger than that in the composite. It should be noted

that the steady-state stage in the creep curves of both materials, unlike those reported for Al based solid-solution alloys [156], is of short duration and, in most cases, does not exceed 8 % strain.

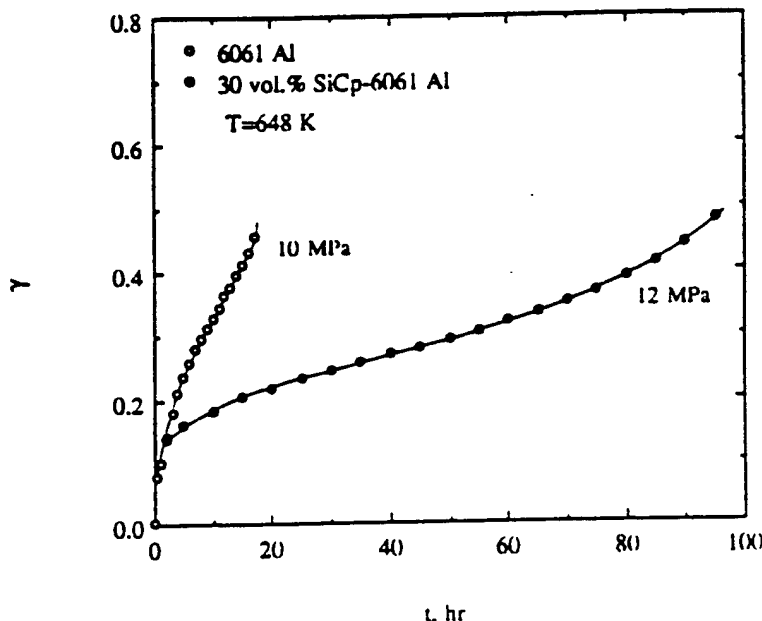


Figure 50. Example of creep curve for 30 vol.% SiC<sub>p</sub>-6061 Al and 6061 Al.

The creep data of 30 vol% SiC<sub>p</sub>-6061 Al and 6061 Al at 678 K are shown in Figure 51, where the steady-state (or minimum) creep rate,  $\dot{\gamma}$ , is plotted against the applied stress,  $\tau$ , on a logarithmic scale. As demonstrated by the figure, the composite exhibits better creep resistance than the alloy over the entire stress range used; a similar finding is noted for 648 K. However, as depicted in Figure 52, the stress dependence of creep rate for both materials is similar in trend; the apparent stress exponent,  $n_a$  ( $n_a = (\partial \ln \dot{\gamma} / \partial \ln \tau)_T$ ) inferred from Figure 51 is high and increases with decreasing applied stresses. In this context, the results of a very recent study[158] on the creep behavior of unreinforced 2219 Al and 2219 Al/TiC/15 P have also shown that the stress exponents for creep in both materials are essentially identical;  $n = 7.9-13.3$ .

#### 7.2.2. Activation Energy for Creep and Stress Dependence of the Steady-State Creep Rate

Activation energy for 30 vol% SiC-6061 Al and 6061 Al, reveal, as shown in Figure 53, that the apparent activation energies,  $Q_a$  ( $Q_a = -R [\partial \ln \dot{\gamma} / \partial (1/T)]_\tau$ ), for creep in both materials resemble in trend those reported for the dispersion strengthened (DS) alloys [159-161] ( $Q_a > Q_D$ , where  $Q_D$  is the activation energy for self diffusion) and that  $Q_a$  for the composite is higher than that for the alloy in the entire stress range.

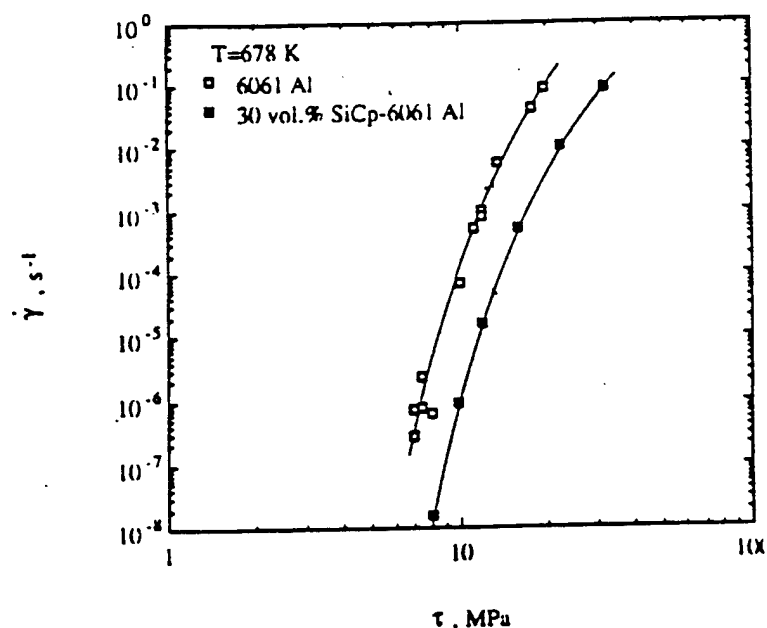


Figure 51. Steady-state creep rate as a function of the applied stress (logarithmic scale)

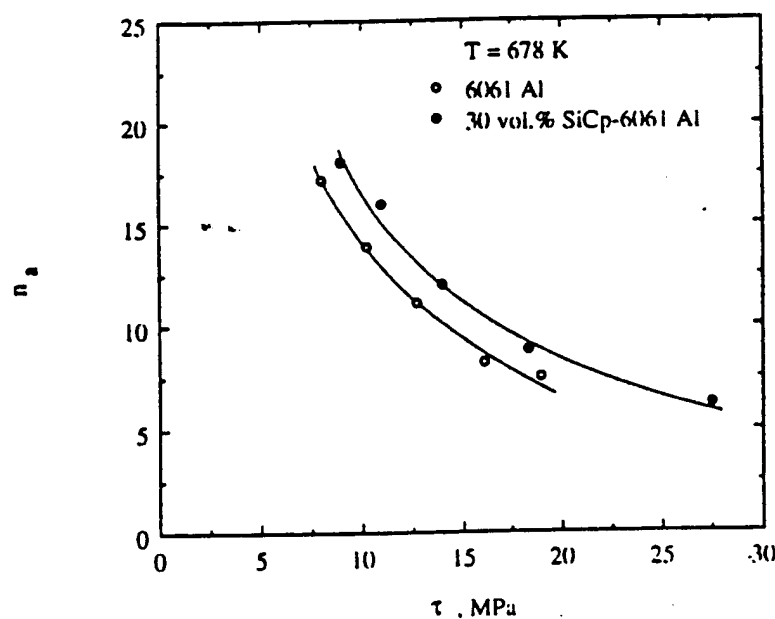


Figure 52. The variation in the apparent stress exponent with the applied stress for 30 vol% SiCp-6061 Al and 6061 Al.

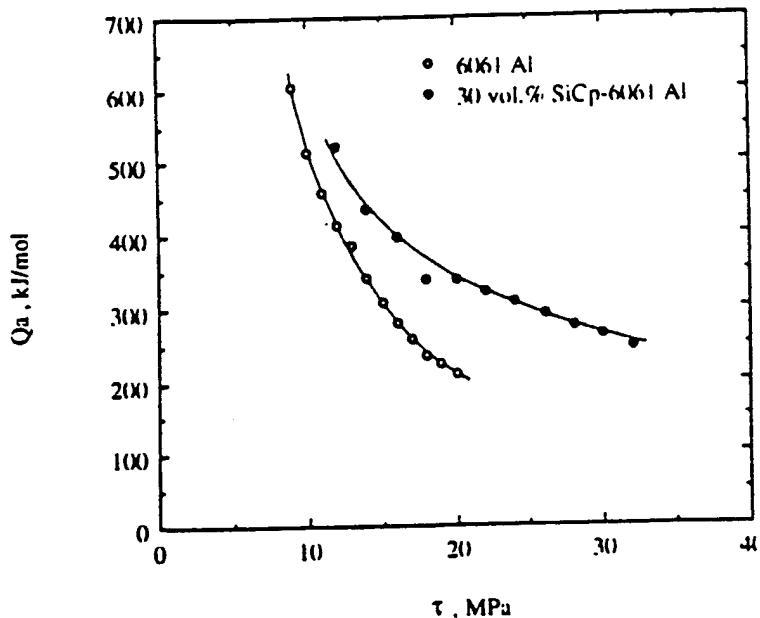


Figure 53. The variation of the apparent activation energy with the applied stress for 30 vol.% SiC<sub>p</sub>-6061 Al and 6061 Al.

In previous studies [162-164], the anomalous stress dependence of creep rate for 30 vol% SiC-6061 Al and 6061 Al was explained in terms of the existence of a strong temperature-dependent threshold stress,  $\tau_0$ . For this case, creep in the composite and the alloy obeys a modified power creep law of

$$\dot{\gamma} = A \left( \frac{\tau - \tau_0}{G} \right)^n \exp \left( -\frac{Q_c}{RT} \right) \quad (31)$$

where A is a constant depending on the microstructure, n is the true stress exponent, G is the shear modulus,  $Q_c$  is the activation energy for creep, R is the gas constant, and T is the absolute temperature. As described below, a plot of  $\dot{\gamma}^{1/n}$  versus  $\tau$  on a double linear scale [165] provides valuable information regarding the value of the true stress exponent, n, the characteristics of the threshold stress,  $\tau_0$ , and the consistency of measurements associated with the activation energy for creep.

First, under the assumption that  $\tau_0$  is constant for each test temperature, a linearity of the plot of  $\dot{\gamma}^{1/n}$  versus  $\tau$  is an indication that the correct value of the true stress exponent, n, has been used. The linearity shown in Figure 54(a) and (b), where the creep data of the composite and the

alloy are plotted with  $n=5$ , justifies that the true stress exponent for creep in both materials is close to 5; it has been shown [163, 164] that the data do not fit a straight line if  $n$  is taken as 3 or 8. This value for  $n$  ( $= 5$ ) is one of the characteristics of dislocation climb-controlled creep [166-168]. Very recently, Gonzalez-Doncel and Sherby [169] have concluded that  $n = 8$ , not  $n = 5$ , provides a better description for the creep data on discontinuous SiC-Al composites. This conclusion has been reached as a result of their detailed analysis of earlier data on several discontinuous SiC-Al composites and their consideration of the results of two recent studies [170, 171]. The first study, conducted by Mishra and Pandey [170], involved an examination of the data of several composites and has led to the suggestion that the creep of Al-SiC composites is controlled by a creep power law which was originally developed by Sherby et al. [172] to describe lattice diffusion creep under constant structure ( $n = 8$ ) and which incorporates a threshold stress. The second study, performed by Pandey et al. [171], focused on the effect of volume fraction and size of SiC on the creep behavior of several SiC-Al composites and adopted the above suggestion made by Mishra and Pandey [170]. While the validity of the conclusion reported by Gonzalez-Doncel and Sherby [169] needs to be examined in systematic investigations that involve studying both creep behavior and microstructure in discontinuous SiC-Al composites, there are several issues which are worth mentioning. First, according to a very recent analysis by Mohamed et al. [163], the finding of Mishra and Pandey [170] that using  $n = 8$  in the plot of the data on SiC-Al composites as  $\dot{\gamma}^{1/n}$  versus  $\tau$  results in a straight line is not conclusive, since the same data can be equally fitted by straight lines when  $n$  is taken as 5 or 7. Second, although Pandey et al. [171] and Gonzalez-Doncel and Sherby [169] adopted the suggestion of Mishra and Pandey [170] that lattice diffusion under the condition of constant structure controls the creep behavior of SiC-Al composites, there is a significant discrepancy between their findings regarding the temperature dependence of the threshold stress. Pandey et al. [171] reported that the threshold stress is independent of temperature whereas Gonzalez-Doncel and Sherby [169] concluded that the threshold stress linearly depends on temperature. Third, in analyzing the creep data of SiC<sub>p</sub>-Al composites in terms of a threshold stress, Gonzalez-Doncel and Sherby [169] apparently disregarded the high stress creep data of Park et al. on 30 vol.% SiC-6061 Al [162] and only used the low stress data for extrapolation to determine the threshold stress. Gonzalez-Doncel and Sherby [169] have justified such an approach on the basis that the high stress data are associated with the development of a creep substructure within the matrix materials which would result in  $n = 5$  (typical of pure metals). However, this approach seems to be questionable since the high stress data of Park et al. [162] on 30 vol.% SiC-6061 Al were essentially obtained under similar conditions (stress and temperature) to those reported for 20 vol.% SiC<sub>p</sub>-2024 Al that were also used by Gonzalez-Doncel and Sherby [169] to determine the threshold stress.

Second, the extrapolation of the resultant straight line in the plot of  $\dot{\gamma}^{1/n}$  versus  $\tau$  to zero strain rate gives the value of  $\tau_0$  at a single temperature. The values of  $\tau_0$  for the composite and the alloy obtained from Figures 54 (a) and (b) are listed in Table 13. Along with Figures 54 (a), 54 (b) and Table 13, Figure 55, where the shear modulus compensated threshold stress,  $\tau_0/G$ , is plotted as a function of the inverse of temperature,  $1/T$ , clearly shows that the values of  $\tau_0$  for both materials are essentially identical and that the temperature dependence of  $\tau_0$  is stronger than that of the shear modulus. As shown in Figure 55, the temperature dependence of  $\tau_0$  can be best-described by:

$$\frac{\tau_0}{G} = B_0 \exp\left(\frac{Q_0}{RT}\right) \quad (32)$$

where  $B_0$  is a constant and  $Q_0$  is an energy term. This strong temperature dependence contrasts with the results of Pandey et al. [171] which, as mentioned earlier, yield a temperature independent threshold stress. Although the origin of  $\tau_0$  is not clearly known, a possible explanation was presented elsewhere [163, 164]. Another approach to obtain the values of the true stress exponent and the threshold stress is available in creep literature [168]. When Eq. 31 controls the creep behavior of the materials, the relation between the apparent stress exponent,  $n_a$ , the true stress exponent,  $n$ , the applied stress,  $\tau$ , and the threshold stress,  $\tau_0$ , is given by

$$n_a = \frac{n}{1 - \frac{\tau_0}{\tau}} \quad (33)$$

Applying Eq. 33 to the data of Figure 52 for the composite at 678 K (for example,  $n_a=7.5$  at  $\tau=22.5$  MPa and  $n_a=18$  at  $\tau=10$  MPa) leads to  $n=5$  and  $\tau_0=7.1$  MPa which are consistent with those estimated from the plot of  $\dot{\gamma}^{1/n}$  versus.

Table 13. The Values of  $\tau_0$  Obtained from the Plot of  $\dot{\gamma}^{1/5}$  vs.  $\tau$  For 30 vol.% SiC<sub>p</sub>-6061 Al and 6061 Al.

T, K	6061 Al	30 vol.% SiC <sub>p</sub> -6061 Al
618	--	10.64
648	8.21	8.56
678	6.28	7.27

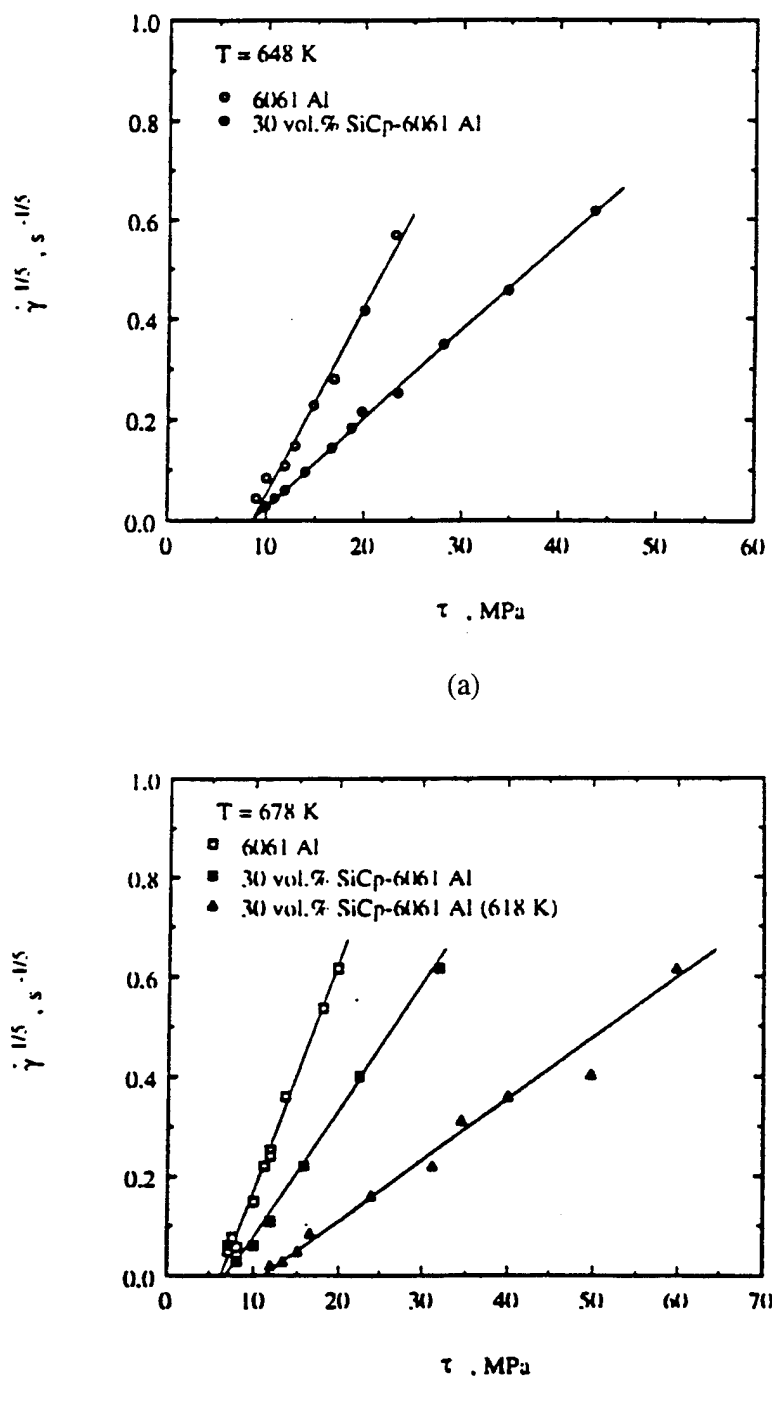


Figure 54. A plot of  $\dot{\gamma}^{1/5}$  vs.  $\tau$  for 30 vol.% SiCp-6061 Al and 6061 Al. (a) 648 K, and (b) 678 K

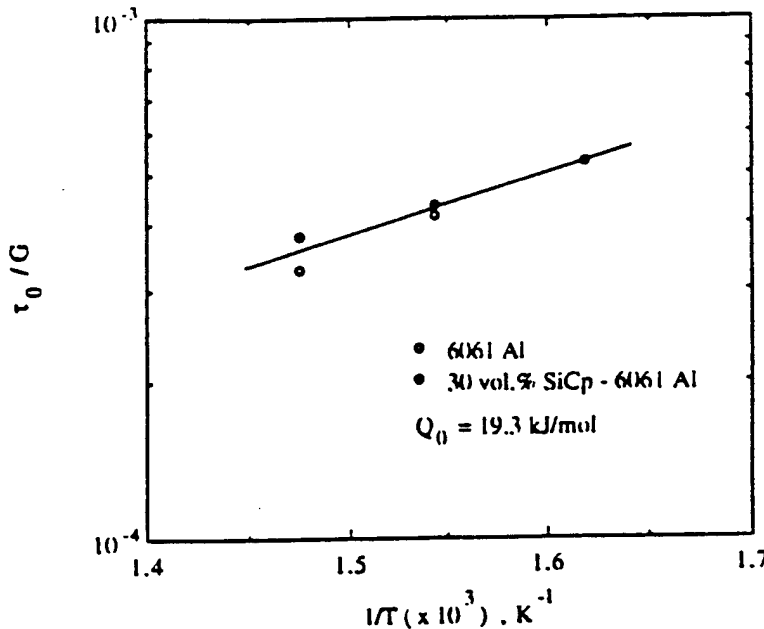


Figure 55. A plot of logarithm of  $(\tau_0/G)$  vs.  $1/T$  for 30 vol.% SiC<sub>p</sub>-6061 Al and 6061 Al.

Third, an estimation of the true activation energy for creep,  $Q_c$ , can be inferred from the slope of the lines in the plot of  $\dot{\gamma}^{1/n}$  vs.  $\tau$ . From Eq. 31,

$$\dot{\gamma}^{1/n} = \frac{A^{1/n}}{G} (\tau - \tau_0) \exp\left(-\frac{Q_c}{nRT}\right) \quad (34)$$

Then, the slope of the line,  $S$ , is

$$S = \left(\frac{A^{1/n}}{G}\right) \exp\left(-\frac{Q_c}{nRT}\right) \quad (35a)$$

and  $Q_c$  is given by

$$Q_c = -nR \frac{\partial \ln(SG)}{\partial \left(\frac{1}{T}\right)} \quad (35b)$$

Using  $n=5$  and  $G=3 \times 10^4 - 16T$  (MPa) which has been reported for pure Al [173], Eq. 35(b) yields  $Q_c=160$  kJ/mol for the alloy which is slightly higher than that for self-diffusion,  $Q_D$ , in aluminum [173] (142 kJ/mol). Very recently, Park et al. [164] have shown that the variation in  $Q_a$  with the

applied stress during the creep of 6061 Al, as given in Figure 53, can be attributed to the temperature dependence of  $\tau_0$  as represented by Eq. 32. Similarly,  $Q_c$  for the composite has been estimated as 222 kJ/mol which is in excellent agreement with that reported earlier using a different procedure, 225 kJ/mol [163]. The discrepancy in the value of  $Q_c$  between the alloy and the composite will be discussed later.

### 7.2.3. Analysis of Creep Behaviors of SiC-6061 Al and 6061 Al

The preceding discussion indicates that the creep characteristics of 30 vol.%  $\text{SiC}_p$ -6061 Al and 6061 Al are similar in regard to: (a) the trend of the variation in both the apparent stress exponent and the apparent activation energy for creep with the applied stress, (b) the value of the true stress exponent ( $n=5$ ), (c) the interpretation of creep in terms of a threshold stress, (d) the values of the threshold stress for creep, and (e) the temperature dependence of the threshold stress. These similarities in behavior between the composite and the unreinforced alloys lead to two important implications: (a) deformation in the matrix, 6061 Al, controls the creep of the composite, 30 vol.%  $\text{SiC}_p$ -6061 Al; and (b) the origin of the threshold stress, which provides an explanation for the high values of the apparent stress exponent, is most probably not related to the presence of SiC particulates. These implications are consistent in part with the finding reported by Krajewski et al. [158] for the creep behavior of unreinforced 2219 Al and 2219 Al/TiC/15 P that creep in both materials is controlled by the same mechanism and that the high stress exponent for creep in the TiC-reinforced alloy is not caused by the introduction of the reinforcement.

Despite the above similarities and their implications, the comparison in Section 7.2.2 shows that the true activation energy in 30 vol.%  $\text{SiC}_p$ -6061 Al, 225 kJ/mol, is higher than that in 6061 Al, 160 kJ/mol, and that the creep rates of the composite material are more than one order of magnitude slower than those of the alloy. A review of creep literature [169, 174-176] indicates the availability of several suggestions that may provide explanations for the higher creep resistance associated with the composites. These suggestions include: (a) load transfer from the matrix to the reinforcement [175]; (b) the development of large triaxial stresses in the matrix near the center of the reinforcement phase [174]; (c) the enhanced dislocation densities in the composite as a result of the presence of large thermal stresses that are caused by large differences in thermal expansion between the matrix and the reinforcement [177]; and (d) the presence of the stress fields around the reinforcement which may lead to an effective interparticle spacing that is finer than the microscopic spacing for the particulate composites [169]. While it is recognized that more than one factor may be responsible for the higher creep strength of the composite, the analysis of this paper will focus on load transfer from the creeping matrix to the rigid reinforcement.

The present analysis regarding load transfer is based on three primary considerations. First, the microstructure of 6061 Al (the unreinforced alloy) is the same as that of the matrix in 30 vol% SiC-6061 Al (the composite); no well-documented evidence is presently available to demonstrate that, under creep conditions, the microstructure of the matrix of the composite is different from that of the reinforced alloy. This consideration, when combined with the observation that the low-stress creep of simple materials (for example, metals and alloys) obeys power law creep, leads to the following expression which relates the creep behavior of the matrix (m) to the unreinforced alloy (alloy).

$$\frac{\dot{\varepsilon}_m}{\dot{\varepsilon}_{all\ oy}} = \left( \frac{\sigma_m}{\sigma_{all\ oy}} \right)^n \quad \text{Tension} \quad (36a)$$

$$\frac{\dot{\gamma}_m}{\dot{\gamma}_{all\ oy}} = \left( \frac{\tau_m}{\tau_{all\ oy}} \right)^n \quad \text{Shear} \quad (36b)$$

Second, as mentioned earlier, the creep behavior of the composite is dominated by the behavior of the matrix. As a result, the above equation, under shear conditions, is rewritten in the form:

$$\frac{\dot{\gamma}_{com}}{\dot{\gamma}_{all\ oy}} = \left( \frac{\tau_{com}}{\tau_{all\ oy}} \right)^n \quad (37)$$

where the subscript "com" refers to the composite. Third, experimental evidence shows that the creep behavior of both 6061 Al and 30 vol.% SiC<sub>p</sub>-6061 Al is characterized by the presence of a threshold stress. This finding requires that Eq. 37 be modified as

$$\left( \frac{\dot{\gamma}_{com}}{\dot{\gamma}_{all\ oy}} \right) = \left( \frac{\tau_{com}^{eff}}{\tau_{all\ oy}^{eff}} \right)^n \quad (38)$$

where the superscript "eff" refers to the effective stress.

In the present analysis, the amount of load transfer,  $\tau_{LT}$ , was estimated, to a first approximation, by adopting the following procedure. The values of  $\dot{\gamma}_{com}$ ,  $\dot{\gamma}_{all\ oy}$  and  $\tau_{all\ oy}^{eff}$  ( $=\tau_{alloy}-\tau_{0,alloy}$ ) inferred from Figure 51 and Table 13 were substituted in Eq. 38;  $\dot{\gamma}_{com}$  was taken at the same applied stress for the alloy. The estimated values of  $\tau_{com}^{eff}$  are considered to be

equivalent to the effective stresses that drive the deformation of only the matrix in the composite. Then,

$$\tau_{LT} = (\tau_{com} - \tau_{0,com}) - \tau_{com}^{eff} \quad (39)$$

where  $\tau_{com}$  and  $\tau_{0,com}$  are the applied stress and the threshold stress for the composite.  $(\tau_{com} - \tau_{0,com})$  is actually equivalent to  $\tau_{all\,alloy}^{eff}$  since  $\tau_{com}$  represents the applied stress and  $\tau_{0,com}$  is, according to the experimental evidence given in Section 7.2.1 and 7.2.2, essentially identical with  $\tau_{0,alloy}$ . The above procedure was applied over the entire stress range for 678 K and 648 K using  $n=5$ . The resultant  $\tau_{LT}$  is plotted as a function of  $(\tau_{com}-\tau_{0,com})$  in Figure 56, which shows that the datum points fit a single straight line for each test temperature;  $\tau_{LT}$  is linearly proportional to  $(\tau_{com}-\tau_{0,com})$ . The slope of this line represents the load transfer coefficient,  $\alpha$ , i.e.,  $\tau_{LT}=\alpha(\tau_{com}-\tau_{0,com})$  and in turn,  $\tau_{com}^{eff}=(1-\alpha)(\tau_{com}-\tau_{0,com})$ . Also, inspection of Figure 56 demonstrates that  $\alpha$  appears to increase with decreasing test temperature from 678 K to 648 K. In order to examine this trend (the variation in  $\alpha$  with temperature), two additional tests were performed for 6061 Al at 618 K and low stresses; for 618 K,  $\tau_{0,alloy}$  is taken as  $\tau_{0,com}$  due to insufficient data. The value of  $\alpha$  inferred from the data for 618 K (Table 14) confirms that load transfer is sensitive to temperature. However, additional data at other temperatures are needed to establish unambiguously the functional dependence of  $\alpha$  on temperature.

#### 7.2.4. Power Law Creep for the Composite

When simple materials are crept at low and intermediate stresses, usually  $\tau < 10^{-3}$  G and at high temperature,  $T > 0.4 T_m$  where  $T_m$  is the melting temperature, the creep behavior of these materials obeys power law creep [166, 173] that may be expressed in the form of

$$\dot{\gamma} = A \left( \frac{\tau}{G} \right)^n \exp \left( - \frac{Q_c}{RT} \right) \quad (40)$$

In applying Eq. 40 to the description of creep in a discontinuous MMC, two factors need to be considered: (a) during creep, reinforcements remain as undeformable second phase, and (b) a portion of the applied stress is borne by these reinforcements. Factor (a) implies that the creep rate of the composite is dominated by that of the matrix. Factor (b) indicates that creep is driven by  $(1-\alpha)\tau$  rather than  $\tau$ . Incorporation of factor (b) in Eq. 40 leads to the following modified expression:

$$\dot{\gamma} = A \left[ \frac{(1-\alpha)\tau}{G} \right]^n \exp \left( - \frac{Q_c}{RT} \right) \quad (41)$$

Table 14. Values of The Load Transfer Coefficient,  $\alpha$ , in 30 vol.% SiC<sub>p</sub>-6061 Al

T, K	experimental	Equation 10a <sup>a</sup>	Equation 10 <sup>b</sup>
618	0.55		
648	0.48	0.26	0.39
678	0.45		

a the original shear lag model [175].

b the modified shear lag model [178].

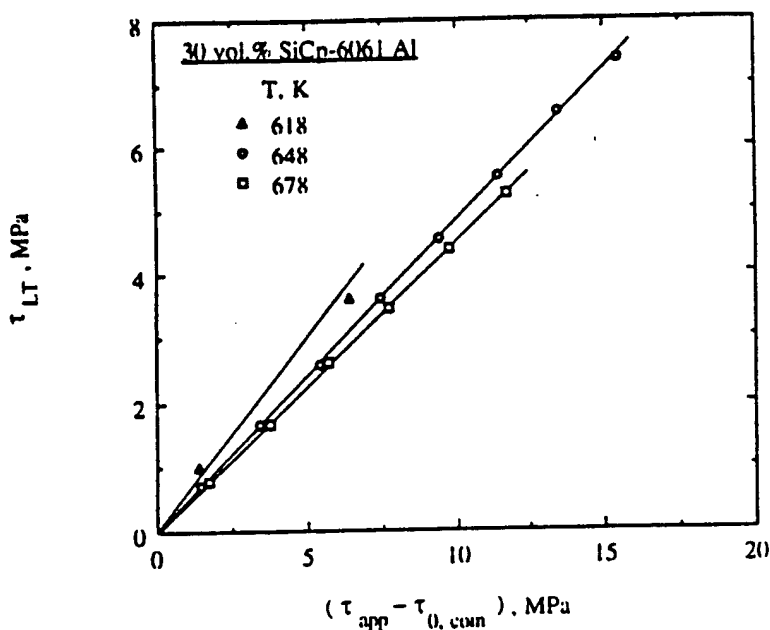


Figure 56. Determination of the load transfer coefficient,  $\alpha$ , by plotting  $\tau_{LT}$  as a function of  $(\tau_{com} - \tau_{0, com})$  for 30 vol.% SiC<sub>p</sub>-6061 Al.

According to the results of the analysis in Section 7.2.3, the load transfer coefficient,  $\alpha$ , is independent of stress (Figure 56). Consequently, the introduction of  $\alpha$  in Eq. 41 does not affect the value of the stress exponent but reduces the creep rate (see Figure 57a). This result, which implies that the load transfer is not responsible for the origin of the threshold stress, is consistent with the results of the numerical analysis performed by other investigators [174, 175]. In addition, if a threshold stress for creep in a SiC-Al composite exists, Eq. 41 needs to be modified to reflect the effect of such a stress, as shown by Eq. 31. This modification leads to two interesting cases. In the first case, a large portion of the load is initially borne by SiC reinforcements and as a result, the effective stress that drives creep deformation in the matrix may be given by

$$\tau_{\text{eff}} = (1 - \alpha)\tau - \tau_0 \quad (42a)$$

and the rate controlling equation becomes

$$\dot{\gamma} = A \left[ \frac{(1 - \alpha)\tau - \tau_0}{G} \right]^n \exp \left( -\frac{Q_c}{RT} \right) \quad (42b)$$

In the second case, creep deformation in the matrix is assumed to start when  $\tau$  exceeds  $\tau_0$ , and then load transfer to the reinforcement occurs as a result of the interaction between the creeping matrix under the steady-state condition and the rigid reinforcements. For this case, the rate-controlling equation is given by

$$\dot{\gamma} = A \left[ \frac{(1 - \alpha)(\tau - \tau_0)}{G} \right]^n \exp \left( -\frac{Q_c}{RT} \right) \quad (43)$$

Consideration of several factors suggests that Eq. 43 is more appropriate than Eq. 42b in describing the creep rate of the composite. First, experimental evidence indicate that, under steady-state creep, matrix deformation, driven by  $(\tau - \tau_0)$ , controls overall composite deformation. Second, as mentioned earlier, the results of Park et al. [162] have revealed that the values of the threshold stress in 30 vol.% SiC-6061 Al are essentially equal to those in 6061 Al. This finding implies that the origin of the threshold stress is the same in both materials and is not related to the presence of SiC particulates; the effect of SiC is mainly reflected in the coefficient  $\alpha$ . Finally, Eq. 43 is in harmony with the original load transfer analysis of Kelly and Street [175] who postulated that the opposition between the creeping matrix and the rigid reinforcement in the vicinity of the reinforcement-matrix interface produces a shearing force whose value determines the load transferred to, and borne by, the reinforcement. Figure 57b schematically describes the above case represented by Eq. 43.

In addition, the consistency between Eq. 43 and the results of Park [162] can be examined by considering the following three items: (a) the ratio between the creep rates of 6061 Al and those of 30 vol.% SiC-6061 Al, (b) the slope of the straight line in the plot of  $\dot{\gamma}^{1/n}$  vs.  $\tau$  on a double linear scale (Figure 54a and b), and (c) the activation energy for creep in the composite.

Consideration of Eq. 31, which describes the creep behavior of 6061 Al, and Eq. 43, which, according to the present analysis, represents the creep behavior of 30 vol.% SiC-6061 Al indicates that when the creep data are plotted in terms of an effective stress, the ratio between the creep rates of the alloy to those of the composite,  $r$ , is equal to  $(1 - \alpha)^{-n}$ . Taking  $n=5$  and using the estimated

values of  $\alpha$  for the three temperatures, 678 K, 648 K, and 618 K (Table 14), the values of  $r$  are calculated as: 20, 26.5, and 54, respectively. These values are in excellent agreement with 19, 25, and 60 that were inferred from the actual creep rates of the alloy and the composite when plotted as a function of the effective stress.

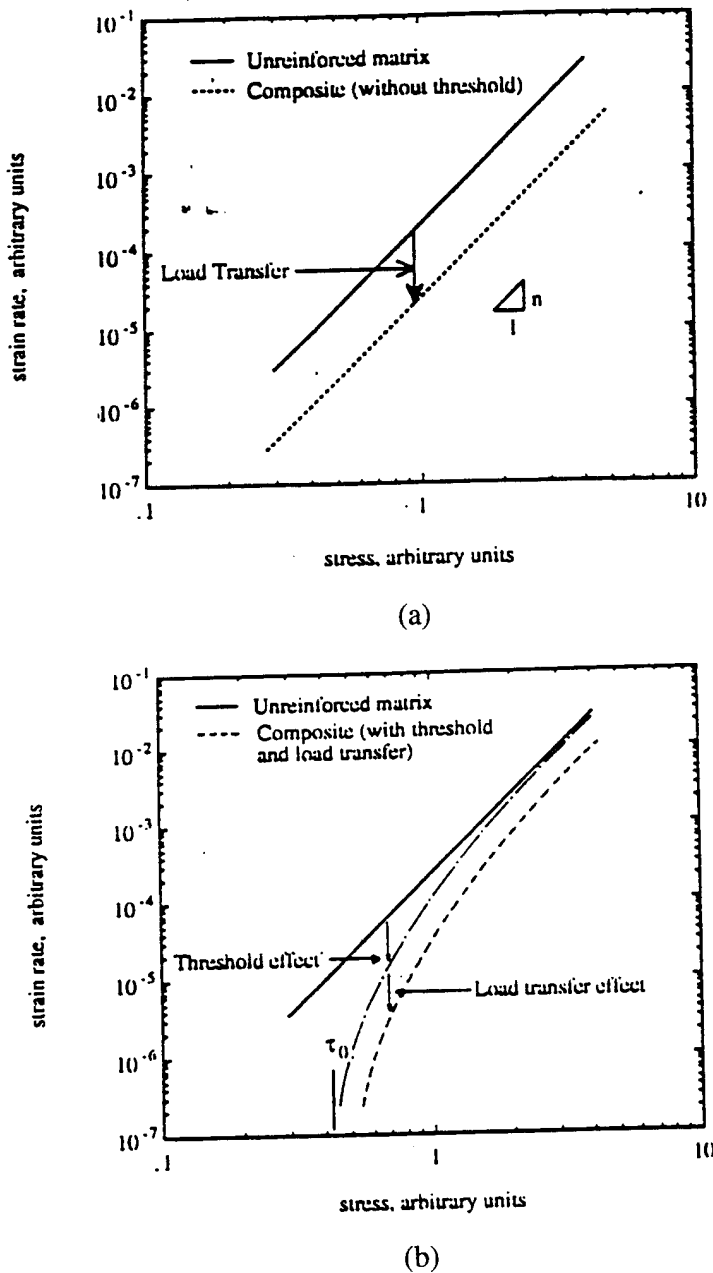


Figure 57. Schematic representation of the (modified) power creep law in conjunction with the effect of load transfer and the threshold stress. (a) without the threshold stress, (b) with the threshold stress.

Consideration of Eq. 35a along with Eqs. 31 and 43 leads to the prediction that, for constant temperature, the slope of the straight line in the plot of  $\dot{\gamma}^{1/n}$  vs.  $\tau$  in case of the alloy would be higher than that in case of the composite by a factor of  $(1-\alpha)$ . Inspection of Figure 54 and using the values of  $\alpha$  listed in Table 14 demonstrates the validity of this prediction.

In an earlier study [163], it has been demonstrated that, by accounting for the temperature dependence of the shear modulus and the threshold stress, the expression of the true activation energy for creep in 30 vol.% SiC-6061 Al may be represented by the following form:

$$Q_c = Q_a + \frac{nRT^2}{G} \frac{\partial G}{\partial T} \left[ 1 + \frac{1}{\frac{\tau}{\tau_0} - 1} \right] - \frac{nQ_0}{\frac{\tau}{\tau_0} - 1} \quad (44)$$

When the appropriate values of various parameters in Eq. 44 ( $n$ ,  $G$ ,  $Q_0$ , etc.) are substituted, an average value of 225 kJ/mol is obtained for  $Q_c$  [163]. This value for the true activation energy for creep in the composite is higher than that for creep in the unreinforced alloy, 6061 Al (160 kJ/mole). On the basis of the present analysis, a probable reason for this discrepancy in the value of  $Q_c$  between the composite and the alloy is that Eq. 44 does not take into account the temperature dependence of the load transfer coefficient,  $\alpha$ . A straightforward treatment of Eq. 43 that is based on the definition of  $Q_a$  ( $= -R(\partial \ln \dot{\gamma} / \partial \ln(1/T))$ ) along with the temperature dependence of  $\tau_0$  and  $\alpha$  yields the following expression for the true activation energy for creep in the composite:

$$Q_c = Q_a + \frac{nRT^2}{G} \frac{\partial G}{\partial T} \left[ 1 + \frac{1}{\frac{\tau}{\tau_0} - 1} \right] - \frac{nQ_0}{\frac{\tau}{\tau_0} - 1} + \frac{nRT^2}{1-\alpha} \left( \frac{\partial \alpha}{\partial T} \right) \quad (45)$$

Eq. 45 was applied to the experimental data using  $n = 5$ ,  $T = 648$  K (average testing temperature),  $\alpha = 0.48$ ,  $\tau_0 = 8.6$  MPa,  $Q_0 = 19.3$  kJ/mol, an average of  $(\partial \alpha / \partial T) \approx (\Delta \alpha / \Delta T) \approx 1.8 \times 10^{-3} \text{ K}^{-1}$ , and Figure 53 which gives  $Q_a$  as a function of the applied stress. In performing the above calculations, low values of the applied stress that approach  $\tau_0$  were not used since  $nQ_0/(\tau/\tau_0 - 1)$  becomes very large. It is noted that the last term in Eq. 45, which account for the contribution of the temperature dependence of load transfer to the activation energy, is insensitive to the stress. The value of that term at 648 K is approximately 60 kJ/mole and reduces the average  $Q_c$  for the composite to 165 kJ/mole which agrees well with that for creep in 6061 Al, 160 kJ/mol. A comparison between the creep rates corrected for load transfer and temperature for both materials was conducted by plotting the normalized strain rate,  $\dot{\gamma}/(1-\alpha)^n \exp(-Q_c/RT)$  against the normalized effective stress,  $(\tau - \tau_0)/G$  in Figure 58;  $\alpha=0$  for the alloy. As shown by the figure, the normalized strain rates of the composite are very close to those of the alloy. The line representing pure Al is

also included in Figure 58 and its position is in good agreement with the normalized creep rates for 6061 Al.

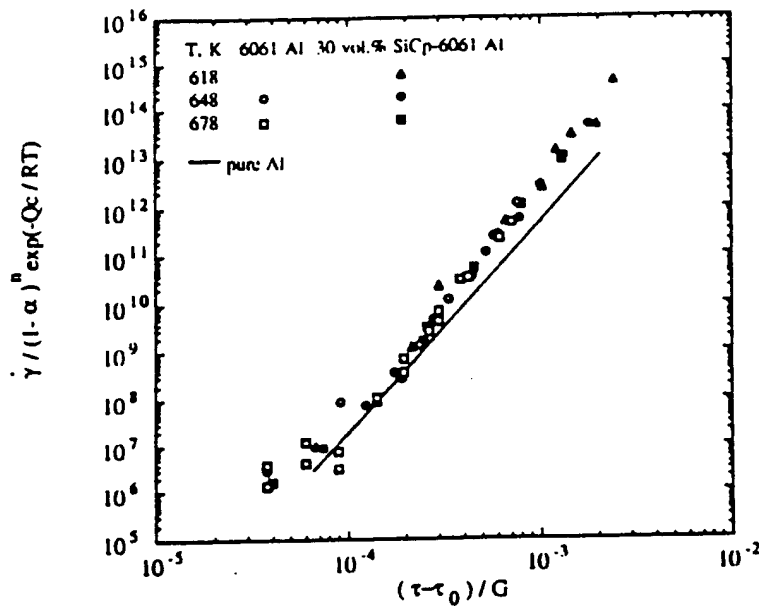


Figure 58. A plot of the normalized strain rate vs. the normalized effective stress for 30 vol.% SiC<sub>p</sub>-6061 Al and 6061 Al for  $n = 5$ . The strain rates of the composite are corrected by considering the effect of load transfer and the true activation energy. The data for pure Al ( $n = 4.5$ ) is taken from ref. [173].

#### 7.2.5. Correlation Between the Present Results and Various Analytical Treatments

Kelly and Street [175] proposed a shear-lag approach that predicts the tensile creep behavior of discontinuous fiber reinforced composites. Such an approach has several basic features including: (a) the composite consists of aligned short fibers that are embedded in the creeping matrix, (b) the load is transferred from the matrix to the fiber by shear loading at the fiber-matrix interface, (c) load transfer to the fibers via direct stresses across their ends is negligible, and (d) the matrix creep rate is described by a creep power law. The above shear lag approach was subsequently modified by other investigators to include the contribution of friction and mean stresses [179], the effect of the transfer of tensile load at the short fiber end [180] and the occurrence of debonding at the interface [181, 182]. Despite the significance of these modifications, the analysis based on the assumptions of the original approach of Kelly and Street [175] is easy to perform and, as pointed out by other investigators [179-182], provides the upper

bound on the creep of the composite. Nevertheless, It should be recognized that such an approach is simplistic, especially in view of the assumption of the alignment of the reinforcements; in discontinuous SiC-Al composites, alignment of SiC particulates or whiskers is, in general, random and misoriented.

By combining the equation that partitions the total tensile stress in a discontinuous reinforced matrix,  $\sigma_c$ , into the matrix and reinforcement (the rule of mixture) and Eqs. 36, the original analysis of Kelly and Street [175] leads to the following expression that gives the ratio between the average stress in the reinforcement and the total stress:

$$\left(\frac{\bar{\sigma}_f}{\sigma_c}\right) = \frac{\Phi\left(\frac{L}{d}\right)^{\frac{n+1}{n}} V_f}{\Phi\left(\frac{L}{d}\right)^{\frac{n+1}{n}} V_f + (1 - V_f)} = \text{constant} \quad (46a)$$

where  $\Phi$  is given by

$$\Phi = \left(\frac{2}{3}\right)^{\frac{1}{n}} \left(\frac{n}{n+1}\right) \left\{ \left( \frac{2\sqrt{3}}{\pi} V_f \right)^{\frac{1}{2}} - 1 \right\}^{-\frac{1}{n}} \quad (46b)$$

$V_f$  is the volume fraction of the reinforcement and  $(L/d)$  is the aspect ratio of the reinforcement.

This ratio only depends on geometrical factors, and is therefore constant. Recently, Nardone and Prewo [180] suggested a modified shear-lag model by considering the load transfer effect at the end of short fiber. Their analysis [180] also provides a similar result that may be written as

$$\left(\frac{\bar{\sigma}_f}{\sigma_c}\right) = \frac{\left\{ \frac{1}{2} \left(\frac{L}{d}\right) + 1 \right\} V_f}{\left\{ \frac{1}{2} \left(\frac{L}{d}\right) + 1 \right\} V_f + V_m} = \text{constant} \quad (47)$$

Since  $\sigma_c$  and  $\bar{\sigma}_f$  are equivalent to the applied stress,  $\sigma_{app}$ , and the amount of the load transfer,  $\sigma_{LT}$ , respectively, Eqs. 46a and 47 can be rewritten as

$\sigma_{LT} = \alpha \sigma_{app}$	Tension	(48)
$\tau_{LT} = \alpha \tau_{app}$	Shear	

where  $\alpha$ , termed earlier as the "load transfer coefficient", is a constant that takes on the value between 0 (no-load transfer) and 1 (full-load transfer). The values of  $\alpha$  predicted from the original shear-lag model [175] and from the modified shear-lag model [180] using  $(L/d) = 1$  for particulate are also included in Table 14. While  $\alpha$  from the modified shear-lag model [180] is in reasonable agreement with the experimental values of  $\alpha$  inferred from the present analysis, the original shear-lag model underestimates  $\alpha$ . This underestimation may arise from the fact that the original shear-lag model does not take account of load transfer at the end of reinforcement, a factor which could be significant in case of the small aspect ratio exhibited by SiC particulates. However, one cannot rule out the possibility that the present analysis may lead to an overestimation of  $\alpha$  since other strengthening factors which may contribute to the composite strengthening were not considered. Very recently, an analysis based on continuum plasticity was conducted by Bao et al. [176] to study the role of non-deforming particles in ductile matrix materials. On the basis of the results of the analysis [176], Rösler et. al. [178] introduced a strengthening coefficient,  $\lambda$ , which is equivalent to  $(1-\alpha)^{-1}$ , and which is given in case of platelet by

$$\lambda = 1 + \left( 5 + \frac{L}{d} \right) V_f^{3/2} \quad (49)$$

For the present composite, 30 vol.% SiC-6061 Al, Eq. 49 leads to  $\lambda=1.98$ , a value which is equivalent to  $\alpha=0.49$ ; this value of  $\alpha$  agrees with the range of  $\alpha$  estimated in the present analysis (Table 14).

Despite the above apparent agreement, the value of  $\alpha$  estimated in the present analysis, unlike those predicted from Eqs. 46a, 47 and 49, seems to vary with temperature. While shear lag approaches [156, 175] and other treatments [176] do not consider the temperature dependence of load transfer, the results of several recent investigations [178, 183-185] indicate the possibility that such a temperature dependence may exist. According to theoretical treatments, conducted by Srolovitz et al. [183-185], for the interaction between dislocation and second phase particle at high temperature, the deviatoric and hydrostatic components of stress in the vicinity of a particle may be relaxed by interfacial diffusion and bulk diffusion, respectively, which lead to an attractive interaction between dislocations and incoherent second phase particles; the stress field around the particle results from three effects: (a) the force on the dislocation, (b) a stress concentration, and (c) an elastic interaction between the dislocation and the particle. In addition to the diffusional stress relaxation, interface sliding [186], if it occurred, may help the relaxation process. Although no attempt has been made to relate the temperature dependence of load transfer to stress relaxation by diffusion or interface sliding, it is quite possible that a considerable amount of the stress

participating in load transfer process can be relaxed by either mechanism and, consequently, load transfer becomes less significant by increasing temperature. This qualitative prediction is in harmony with the observation in the present analysis.

### VIII. SUMMARY

On the basis of the experimental and theoretical results obtained in this research program, some concluding remarks may be summarized as following:

- (1) The numerical analysis of spray atomization and deposition of Ta-2.5W revealed that the axial gas velocity decays exponentially along the spray axis, while the gas flow diameter increases in the axial direction. The radial profiles of axial gas velocities exhibit a shape akin to a Gaussian probability distribution. The gas flow is predominantly in the axial direction as a result of the axisymmetric assumption. The axial and radial droplet velocities increase initially along the axial direction and attain rapidly their maximum values. With increasing axial distance, the radial profiles of the axial droplet velocities become wider and approach rapidly the profiles of gas velocities. At any axial distance, the droplet velocity, temperature, cooling rate and solidification rate all exhibit a maximum at the spray axis, and decrease to a minimum at the periphery of the spray cone, except for the radial locations where solidification occurs. Accordingly, for a given droplet diameter, the achievable undercooling is smaller, the flight time required to reach a given axial distance is longer, and the secondary dendrite arm spacing formed during post-recrystallization solidification of the droplets is larger in the periphery region of the spray cone than elsewhere in the radial direction. Hence, the droplets in the periphery region of the spray cone solidify within a shorter flight distance relative to those at the spray axis due to the longer flight time in the periphery. With decreasing droplet size, the flight distance required to attain the maximum droplet velocities decreases and the flight time required for any given flight distance also decreases. Compared to a large droplet, a small droplet exhibits a large axial velocity, a low temperature, a high cooling rate and a large solid fraction at any radial distance, except for the locations where solidification takes place and the fringe region where the relative velocity between the gas and small droplets is low. At the same time, a small droplet has a wider radial distribution at any axial distance. Hence, it may be expected that coarse droplets comprise the core whereas the periphery of the spray cone is populated by fine droplets.
- (2) On the basis of the study on LPPS processed W, the following five observations may be made. (a) Microstructure observation on the low pressure plasma sprayed W has revealed that the porosity is approximately 9% to 10%, and that the pore size ranges from 0.1 to 50  $\mu\text{m}$ . The formation of porosity is attributed to the presence of partially melted particles, interactions between droplets and deposition surfaces, gas entrapment, solidification

shrinkage, and presence of the pores in the as-received powder particles. (b) A relative large amount of partially melted particles were observed in the as-sprayed W, which should contribute a significant proportion of the porosity in the plasma sprayed W. The formation of porosity is mainly due to the interactions between partially melted particles, and the interactions between partially melted particles and deposition surfaces. (c) The interactions between deformation and solidification of droplets play an important role in the formation of porosity. Moreover, the interactions between melted particles and deposition surfaces also result in the formation of porosity. (d) The contribution of the oxygen and nitrogen entrapment to the formation of porosity is insignificant. (e) Since the presence of partially melted or unmelted particles in the deposit, the porosity in the as-received powders contributes a finite proportion of porosity observed in the experiments.

- (3) The formation of porosity during low pressure plasma spraying has been numerically analyzed. During impingement on a flat substrate, a single droplet spreads uniformly in the radial direction and eventually solidifies into a thin splat. Accompanying the flattening and solidification, the splat edge may separate from the solid/liquid interface depending on processing parameters. The separation phenomenon causes the formation of micro-pores primarily in the fringe region of the splat. The rising velocity of the solid/liquid interfaces in the deposit and the deformation velocity of the droplet are two critical factors that influence the formation of micro-porosity in the deposit. The initial impact velocity of the droplet, droplet temperature and substrate temperature, which are major influencing factors on these two velocities, become critical to the formation of the porosity. When the initial impact velocity or the substrate temperature is sufficiently high so that significant deformation occurs prior to significant solidification, the separation takes place to a less violent extent, or occurs at a later time. Hence the micro-porosity is low. When the initial impact velocity or the substrate temperature is sufficiently low that significant solidification is completed prior to significant deformation, the micro-porosity is also relatively low. This is attributable to the decreased amount of voids or to the decreased total solidification time, despite the fact that the separation occurs at an earlier time for a lower substrate temperature. At low impact velocities or low temperatures, the contact and eventual adhesion of the splat with the substrate may be worse as a result of the small flattening extent. When the initial impact velocity or the substrate temperature is between these two extremes, the deformation velocity and the solidification velocity become comparable and most of the voids formed due to the separation phenomenon are fixed in the solidified layer. As a result, the micro-porosity becomes large. A droplet with a high viscosity impinging onto a solid, flat substrate leads to a relatively small micro-porosity, but may

produce macro-pores as a result of the small flattening extent. A fully liquid droplet impinging onto a flattening, solidifying splat produces relatively large micro-porosity, while multiple fully liquid droplets colliding with a flattening, solidifying splat cause a relatively small micro-porosity and at the same time the formation of vortices. The ejection and bounce of the liquid may be largely suppressed by solidification. A fully liquid droplet impinging onto a solid particle on a flat substrate leads to the formation of macro-pores between the particle boundary and the substrate; multiple fully liquid droplets striking onto a solid particle on a flat substrate substantially eliminate the macro-pores, but simultaneously produce vortices within the liquid, as well as ejection and break-up of the liquid; multiple fully liquid droplets striking onto multiple solid particles on a flat substrate, not only lead to vortices and ejection of the liquid, but also to the formation of the macro-pores. Decreasing the roughness height of the deposition surface and increasing the roughness spacing may improve the extent of droplet flattening and reduce the break-up of liquid and micro-porosity.

- (4) Low-pressure plasma deposition can be used to produce dense SiC-reinforced MoSi<sub>2</sub> composites. The fracture toughness for the plasma-sprayed composite was higher than that for PM MoSi<sub>2</sub> but lower than that for PM SiC/MoSi<sub>2</sub>. The observed difference in fracture toughness is attributed to a higher volume fraction of SiC (20 vol.% vs. 8.7 vol.%), and the morphology of the particles (whiskers vs. particle) in the PM composite. The creep resistance at 1350°C for the plasma-sprayed SiC/MoSi<sub>2</sub> was lower than that for both PM MoSi<sub>2</sub> and SiC/MoSi<sub>2</sub>. The lower creep resistance can be attributed to the melting or softening of an amorphous intergranular phase which assists grain boundary sliding. The amorphous phase is likely a silica phase formed along the MoSi<sub>2</sub> grain boundaries or SiC/MoSi<sub>2</sub> interfaces during plasma deposition. Although the fracture toughness and the creep resistance for the plasma-sprayed SiC/MoSi<sub>2</sub> are lower than that for PM SiC/MoSi<sub>2</sub>, the preliminary results are encouraging since plasma-spraying involves fewer processing steps than those required by PM, rendering the former process more economical than the latter.
- (5) The creep behavior of plasma-sprayed SiC/MoSi<sub>2</sub> as a function of temperature was investigated. A change in the rate-controlling creep mechanism as a function of temperature was observed. At T<1300°C, the stress exponent of approximately 2.5 and activation energy for creep of 300 kJmol<sup>-1</sup> is associated with dislocation motion controlled by lattice diffusion. The creep rate was higher for the material tested parallel to the spray direction (SD) than perpendicular to the spray direction (PSD). Examination of the microstructure

after deformation revealed grain boundary cracking for  $T < 1300^{\circ}\text{C}$ . At  $T > 1300^{\circ}\text{C}$ , the stress exponent of approximately 1.5 and activation energy of  $190 \text{ kJmol}^{-1}$  is associated with grain boundary sliding controlled by grain boundary diffusion. The creep rate was independent of orientation in the grain boundary sliding region. No grain boundary cracks were observed after deformation in this temperature region. These results confirm the suggestion in related studies that a change in the rate-controlling creep mechanism occurs at approximately  $1300^{\circ}\text{C}$ . It is believed that this change is a result of melting or softening of amorphous grain boundary phase. The amorphous phase is likely silica formed along  $\text{MoSi}_2$  grain boundaries during plasma deposition.

- (6) A comparison between the creep characteristics of 30 vol.% SiC particulate reinforced 6061 Al and unreinforced 6061 Al under identical experimental conditions shows that creep strengthening in the composite arises mainly from two independent mechanisms: (a) the existence of a temperature dependent threshold stress that results in high and variable apparent stress exponents, and (b) a temperature dependent load transfer that is linearly proportional to the applied stress and that leads to the higher creep resistance of the composite over the entire stress range considered in the present analysis. When the contribution of load transfer is incorporated in the description of the creep behavior of the composite, the rate equation that governs such behavior is given by

$$\dot{\gamma} = A \left[ \frac{(1 - \alpha)(\tau - \tau_0)}{G} \right]^n \exp\left(-\frac{Q_c}{RT}\right)$$

where  $\alpha$  is the load transfer coefficient. The high apparent activation energies for creep in the composite are reduced to a value close to the true activation energy for creep in the alloy by considering the temperature dependence of the shear modulus, the threshold stress for creep, and the load transfer coefficient,  $\alpha$ .

## NOMENCLATURE

$\epsilon$	amplitude of sinusoidal wave function for deposition surface shape. $\epsilon/d_0$ is dimensionless roughness height of deposition surface.
$\bar{v}_g$	average gas velocity along axis line of spray cone, (m/s)
$\vec{F}_b$	body force;
$\kappa$	Boltzmann's constant, (J/K)
$\dot{T}$	cooling rate, (K/s)
$\epsilon_E$	emissivity of surface
$\Delta h$	enthalpy of fusion;
$\vec{g}$	gravitational acceleration vector;
$\sigma_m$	solid/liquid interfacial energy, (J/m <sup>2</sup> )
$\gamma$	specific heat ratio of gas
$\sigma$	Stephen-Boltzmann's constant, (W/m <sup>2</sup> K <sup>4</sup> )
$\vec{v}$	velocity vector;
$\tau$	viscous stress tensor;
$\Theta$	volume fraction of liquid.
$\lambda$	wavelength of sinusoidal wave function for deposition surface shape. $\lambda/d_0$ is dimensionless roughness spacing of deposition surface.
$\rho, \rho_s$	density of liquid and solid, respectively;
$\rho_d, \rho_g$	density of droplet and atomization gas, respectively, (kg/m <sup>3</sup> )
$\rho_{g0}$	density of atomization gas at 0 K, (kg/m <sup>3</sup> )
$a$	atomic diameter, (m)
$a_l, a_s$	thermal diffusivity of liquid and solid, respectively;
$C$	constant related to local gas flow width
$c$	constant in equation for $\mu_g$
$C/A$	Aspect ratio of particulates
$C_{drag}$	drag coefficient, $C_{drag} = F_{drag}/[\frac{1}{2} \rho_g U_r^2 \pi (\frac{d}{2})^2]$
$c_l, c_s$	heat capacity of liquid and solid, respectively;
$c_{pd}, c_{pg}$	thermal capacity of droplet and atomization gas, respectively, (J/kg K)
$c_{pl}, c_{ps}$	thermal capacity of liquid and solid alloy, respectively, (J/kg K)
$D$	initial half-width of gas flow, (m)
$d$	droplet diameter, (m)
$d_0$	initial droplet diameter;

$d_{50}$	Mean powder particle size
$D_{lm}$	self-diffusivity in melt, ( $m^2/s$ )
$d_m$	effective molecular diameter, (m)
$d_o$	Nozzle diameter
$\Delta T$	Temperature Gradient
F	volume of fluid function;
$\phi$	Injection angle
$F_{drag}$	drag force
$F_{e\phi}$	Particulate injection
$f_s$	solid fraction of droplet
$g$	gravity acceleration, ( $m/s^2$ )
h	Heat transfer coefficient
I	nucleation rate, (/ $m^3 s$ )
i	subscript denoting annular volumes;
J	mechanical equivalent of heat, ( $m \ kg/J$ )
$J_{Fe}$	Mass flow rate of particulates
$J_g$	Gas flow rate
$J_m$	Metal flow rate
K	Thermal conductivity
$k_e$	equilibrium partition coefficient
$K_g$	thermal conductivity of atomization gas, ( $W/m K$ )
$K_{g0}$	thermal conductivity of atomization gas at 0 K, ( $W/m K$ )
$k_l, k_s$	thermal conductivity of liquid and solid, respectively;
$K_m$	solid/liquid interface mobility, ( $m/sK$ )
M	molar weight of melt, ( $kg/mol$ )
m	Power index
Ma	Mach number, $Ma = \frac{\bar{v}_g}{v_s}$
$\mu_m$	Viscosity of melt
N	Avogadro's constant, (atoms/mol)
n	Power index in equation for $K_g$
NA	total number of annular volumes within solidified splat;
p	scalar pressure;
Pr	Prandtl number, $P_r = \frac{\mu g c_p}{K_g}$
$Q_c$	Heat of conduction

$Q_h$	Heat of convection
$Q_R$	Heat of radiation
R	gas constant, (J/K mol)
r	radial coordinate, (m)
Re	Reynolds number, $Re = \frac{d_0 u_0}{\nu}$ .
$r_e$	recovery factor
$\rho_m$	Density of melt
s	solid fraction of droplet during recalescence
SDAS	secondary dendrite arm spacing, ( $\mu\text{m}$ )
T	Temperature of particulates
t	time, (s)
$T'$	film temperature, (K)
$T_d, T_g$	temperature of droplet and atomization gas, respectively, (K)
$T_{d0}$	initial temperature of droplet, (K)
$t_i$	time that solidification begins at some radial position r;
$T_l^*, T_s^*$	dimensionless temperature of droplet and substrate, respectively;
$T_l, T_m, T_s$	droplet temperature, melting temperature and substrate temperature, respectively;
$T_n$	nucleation temperature, (K)
$t_s$	time that solidification terminates at some radial position r;
U	freezing constant;
$u_0$	initial impact velocity of droplet in axial direction;
$u_d, u_g$	radial velocity of droplet and atomization gas, respectively, $u_d = \frac{dr}{dt}$ , (m/s)
$u_o$	free stream velocity defined originally in [108] and taken in the present computations as relative velocity between droplet and atomization gas, (m/s)
$U_r$	relative speed between gas and droplet, $U_r = \left[ (v_g - v_d)^2 + (u_g - u_d)^2 \right]^{\frac{1}{2}}$ , (m/s)
$v_d, v_g$	axial velocity of droplet and atomization gas, respectively, $v_d = \frac{dz}{dt}$ , (m/s)
$v_{d0}, v_{g0}$	initial axial velocity of droplet and atomization gas, respectively, (m/s)
$V_{Fe}$	Exit velocity of particulates
$V_g$	Exit velocity of gas
$V_m$	molar volume of melt, ( $\text{m}^3/\text{mol}$ )
$v_s$	sound speed of gas at 220 K, $v_s = \sqrt{\gamma RT}$ , (m/s)
We	Weber number, $We = \frac{d_0 u_0^2 \rho}{\sigma}$ .

Y	thickness of the solidified layer at any real time t after impact;
Z	Flight distance
$z, z_i, z_s$	axial coordinate, constants related to the atomizer geometry and atomization parameters, respectively, (m)
$Z_i$	Injection distance
$z_s(i,t)$	axial coordinate of solid-liquid interface in annular volume i at time t;
$\mu_g$	kinematic viscosity of atomization gas, (kg/m s)
$\mu_{g0}$	kinematic viscosity of atomization gas at 0 K, (kg/m s)
$\Delta H_m$	latent heat of fusion, (J/kg)
$\Delta T$	undercooling, $\Delta T = T_l - T_n$

## REFERENCES

- [1] P. Kumar, *J. Met.*, Vol. 10, 1988, p. 24.
- [2] R. W. Balliett, M. Coscia and F. J. Hunkler, *J. Met.*, Vol. 9, 1986, p. 25.
- [3] W. A. Spitzig, C. V. Owen and T. E. Scott, *Metall. Trans. A*, Vol. 17, 1986, p. 527.
- [4] K. K. Schulze, H. A. Jehn and G. Horz, *J. Met.*, Vol. 10, 1988, p. 25.
- [5] B. H. Rabin, A. Bose and R. M. German, *Int. J. Powder Metall.*, Vol. 25, 1989, p. 21.
- [6] R. G. O'Donnell and R. L. Woodward, *Metall. Trans. A*, Vol. 21, 1990, p. 744.
- [7] S. J. Cimpoeru and R. L. Woodward, *J. Mater. Sci. Lett.*, Vol. 9, 1990, p. 187.
- [8] C. A. Acosta, M. d. Viola and J. C. Pedregosa, *J. Mater. Sci. Lett.*, Vol. 10, 1991, p. 251.
- [9] E. Hechtl, H. R. Yang, C. H. Wu and W. Eckstein, *J. Nucl. Mater.*, Vol. 176-177, 1990, p. 874.
- [10] A. Bose and R. M. German, *Metall. Trans. A*, Vol. 19, 1988, p. 2467.
- [11] A. Bose, G. Jerman and R. M. German, *Powder Metall. Int.*, Vol. 21, 1989, p. 9.
- [12] A. Bose and R. M. German, *Metall. Trans. A*, Vol. 21, 1990, p. 1325.
- [13] S. C. Yang and R. M. German, *Metall. Trans. A*, Vol. 22, 1991, p. 786.
- [14] M. Naka, M. Miyake and I. Okamoto, *J. Non-Cryst. Solids*, Vol. 117-118, 1989, p. 658.
- [15] K. N. Ramakrishnan and G. S. Upadhyaya, *J. Mater. Sci. Lett.*, Vol. 9, 1990, p. 456.
- [16] F. Kostrubiec and M. Walczak, *Trans. ASME, J. Eng. Mater. Technol.*, Vol. 113, 1991, p. 130.
- [17] J. Dutkiewicz and G. Kostorz, *Acta Metall. Mater.*, Vol. 38, 1990, p. 2283.
- [18] B. A. Gnesin, V. G. Glebovskii, M. I. Karpov, V. V. Kireyko and A. A. Snegirev, *J. Less-Common Met.*, Vol. 167, 1990, p. 11.
- [19] D. Han and J. J. Mecholsky, *J. Mater. Sci.*, Vol. 25, 1990, p. 4949.
- [20] R. M. German, *Scr. Metall.*, Vol. 14, 1980, p. 955.
- [21] R. M. German, L. L. Bourguignon and B. H. Rabin, *J. Met.*, Vol. 37, 1985, p. 36.
- [22] A. A. Sadek, M. Ushio and F. Matsuda, *Metall. Trans. A*, Vol. 21, 1990, p. 3221.
- [23] S.-C. Yang, S. S. Mani and R. M. German, *JOM*, Vol. 42, 1990, p. 16.
- [24] S. M. Cardonne, P. Kumar, C. A. Michaluk and H. D. Schwartz, *Adv. Mater. Proc.*, Vol. 142, 1992, p. 16.
- [25] D. Apelian, M. Paliwal, R. W. Smith and W. F. Schilling, *Int. Mater. Rev.*, Vol. 28, 1983, p. 271.
- [26] D. Apelian, R. W. Smith and D. Wei, *Powder Metall. Int.*, Vol. 20, 1988, p. 7.

- [27] R. Tiwari, H. Herman, S. Sampath and B. Gudmundsson, *Mater. Sci. Eng.*, Vol. A144, 1991, p. 127.
- [28] S. Sampath and H. Herman, *JOM*, Vol. 45, 1993, p. 42.
- [29] A. R. Moss and W. J. Young, *Powder Metall.*, Vol. 17, 1964, p. 261.
- [30] A. Sickinger and E. Muehlberger, *Powder Metall. Int.*, Vol. 24, 1992, p. 91.
- [31] Z. Z. Mutasim and R. W. Smith, in *Tungsten and Tungsten Alloys- Recent Advances*, edited by A. Crowson and E. S. Chen, TMS, Warrendale, PA, 1991, p. 69.
- [32] M. R. Jackson, P. A. Siemers, S. F. Rutkowski and G. Frind, *Int. J. Refract. Hard Met.*, Vol. 8, 1989, p. 196.
- [33] J. Schlichting, *High Temp. - High Press.*, Vol. 10, 1978, p. 241.
- [34] F. D. Gac and J. J. Petrovic, *J. Am. Ceram. Soc.*, Vol. 68, 1985, p. C200.
- [35] D. H. Carter, J. J. Petrovic, R. E. Honnoll and W. S. Gibbs, *Ceram. Eng. Sci. Proc.*, Vol. 10, 1989, p. 1121.
- [36] W. S. Gibbs, J. J. Petrovic and R. E. Honnoll, *Ceram. Eng. Sci. Proc.*, Vol. 8, 1987, p. 645.
- [37] D. H. Carter and G. F. Hurley, *J. Am. Ceram. Soc.*, Vol. 70, 1987, p. C79.
- [38] A. K. Bhattacharya and J. J. Petrovic, *J. Am. Ceram. Soc.*, Vol. 74, 1991, p. 2700.
- [39] G. T. Gray III and R. G. Castro, in *TMS Annual Meeting, San Diego*, 1992.
- [40] R. G. Castro, R. W. Smith, A. D. Rollett and P. W. Stanek, *Scripta Metall. et Mater.*, Vol. 26, 1992, p. 207.
- [41] A. Bose, D. Sims and R. M. German, *Metall. Trans. A*, Vol. 19, 1988, p. 487.
- [42] A. Bose and R. M. German, *Metall. Trans. A*, Vol. 19, 1988, p. 3100.
- [43] S. P. Murarka, *J. Vacuum Sci. Technol.*, Vol. 17, 1980, p. 775.
- [44] B. K. Bhattacharyya, D. M. Bylander and L. Kleinman, *Phys. Rev. B*, Vol. 31, 1985, p. 2049.
- [45] M. Azizan, R. Baptist, T. A. Nguyen Tan and J. Y. Veuillen, *Appl. Surf. Sci.*, Vol. 38, 1989, p. 117.
- [46] A. Climent, J. Perriere, A. Laurent, B. Lavernhe, R. Perez-Casero and J. M. Martinez-Duart, *Appl. Surf. Sci.*, Vol. 38, 1989, p. 125.
- [47] A. K. Vasudevan and J. J. Petrovic, *Mater. Sci. Eng. A*, Vol. 155, 1992, p. 1.
- [48] T. C. Lu, A. G. Evans, R. J. Hecht and R. Mehrabian, *Acta Metall. Mater.*, Vol. 39, 1991, p. 1853.
- [49] T. C. Lu, Y. G. Deng, C. G. Levi and R. Mehrabian, *Mater. Sci. Eng. A*, Vol. 155, 1992, p. 11.
- [50] P. J. Meschter and D. S. Schwartz, *JOM*, Vol. 41, 1989, p. 52.
- [51] J. D. Cotton, Y. S. Kim and M. J. Kaufman, *Mater. Sci. Eng. A*, Vol. 144, 1991, p. 287.

- [52] M. J. Maloney and R. J. Hecht, *Mater. Sci. Eng. A*, Vol. 155, 1991, p. 19.
- [53] Y. Umakoshi, T. Sakagami, T. Yamane and T. Hirano, *Philos. Mag. Lett.*, Vol. 59, 1989, p. 159.
- [54] Y. Umakoshi, T. Hirano, T. Sakagami and T. Yamane, *Scr. Metall.*, Vol. 23, 1989, p. 87.
- [55] Y. Umakoshi, T. Sakagami, T. Hirano and T. Yamane, *Acta Metall. Mater.*, Vol. 38, 1990, p. 909.
- [56] O. Unal, J. J. Petrovic, D. H. Carter and T. E. Mitchell, *J. Am. Ceram. Soc.*, Vol. 73, 1990, p. 1752.
- [57] M. Nakamura, S. Matsumoto and T. Hirano, *J Mater Sci*, Vol. 25, 1990, p. 3309.
- [58] T. Hirano, M. Nakamura, K. Kimura and Y. Umakoshi, *Ceram. Eng. Sci. Proc.*, Vol. 12, 1991, p. 1619.
- [59] K. Kimura, M. Nakamura and T. Hirano, *J Mater Sci*, Vol. 25, 1990, p. 2487.
- [60] R. R. Giler, *Metals Engineering Quarterly*, 1973, p. 48.
- [61] V. Bizzari, B. Linder and N. Lindskog, *Metals And Materials*, Vol. 5, 1989, p. 403.
- [62] P. S. Kisly and V. Y. Kodash, *Ceramics Intl.*, Vol. 15, 1989, p. 189.
- [63] A. J. Moulson and J. M. Herbet, in *Electroceramics: Materials, Properties, Application*, Chapman And Hall, New York, NY, 1991, p. 121.
- [64] S. P. Andrew, R. D. Caligiuri and L. E. Eiselstein, in *Tungsten and Tungsten Alloys - Recent Advances*, edited by A. Crowson and E. S. Chen, TMS, Warrendale, PA, 1991, p. 141.
- [65] L. Ekbom, L. Holmberg and A. Persson, in *Tungsten & Tungsten Alloys - 1992*, edited by A. Bose and R. J. Dowding, MPIF, Princeton, NJ, 1992, p. 551.
- [66] T. W. Penrice, in *Progress in Powder Metallurgy*, edited by M. S. Nayar, S. M. Kaufman and K. E. Meiners, MPIF, Princeton, NJ., 1984, p. 507.
- [67] R. J. Dowding, in *P/M in Aerospace, Defense and Demanding Applications*, edited by F. H. Froes, MPIF, Princeton, NJ, Princeton, NJ, 1993, p. 25.
- [68] L. S. Magness and T. G. Farrand, in *Proceedings of The 1990 Army Science Conference*, 1990, p. 465.
- [69] L. S. Magness, in *Tungsten & Tungsten Alloys - 1992*, edited by A. Bose and R. J. Dowding, MPIF, Princeton, NJ., 1992, p. 15.
- [70] T. W. Penrice, in *Proceedings of the Fourth International Tungsten Symposium*, 1987, p. 140.
- [71] R. J. Dowding, in *1991 P/M in Aerospace and Defense Technologies*, edited by F. H. Froes, MPIF, Princeton, NJ., 1991, p. 109.
- [72] M. R. Staker, *Acta Metall.*, Vol. 29, 1981, p. 683.

- [73] D. A. Shockley, in *Metallurgical Applications of Shock-Wave and High-Strain-Rate Phenomena*, edited by L. E. Murr, K. P. Staudhammer and M. A. Meyers, Marcel Dekker Inc., New York, NY, 1986, p. 633.
- [74] J. Karthikeyan, R. Ratnaraj, A. J. Hill and Y. C. Fayman, in *Thermal Plasma Coating: Properties, Processes and Applications*, edited by T. F. Bernecki, ASM International, Materials Park, OH, 1992, p. 497.
- [75] S. A. Jones, J. R. Auhl and T. N. Meyer, in *Thermal Plasma Coating: Properties, Processes and Applications*, edited by T. F. Bernecki, ASM International, Materials Park, OH, 1992, p. 329.
- [76] A. I. Kahveci, C. R. Cook, J. R. Auhl and T. N. Meyers, in *Thermal Plasma Coating: Properties, Processes and Applications*, edited by T. F. Bernecki, ASM International, Materials Park, OH, 1992, p. 357.
- [77] R. Tiwari and H. Herman, in *Thermal Plasma Coating: Properties, Processes and Applications*, edited by T. F. Bernecki, ASM International, Materials Park, OH, 1992, p. 375.
- [78] J. J. Petrovic and R. E. Honnell, *Ceram. Eng. Sci. Proc.*, Vol. 11, 1990, p. 734.
- [79] R. Tiwari, H. Herman and S. Sampath, *Mater. Sci. Eng.*, Vol. A155, 1992, p. 497.
- [80] Y.-L. Jeng, J. Wolfenstine, E. J. Lavernia, D. E. Bailey and A. Sickinger, *Scr. Metall. Mater.*, Vol. 28, 1993, p. 453.
- [81] E. J. Lavernia, *Int. J. Rapid Solidif.*, Vol. 5, 1989, p. 47.
- [82] E. J. Lavernia and N. J. Grant, *Int. J. Rapid Solidif.*, Vol. 2, 1986, p. 93.
- [83] R. H. Bricknell, *Metall. Trans.*, Vol. 17A, 1986, p. 583.
- [84] K. Ogata, E. J. Lavernia, G. Rai and N. J. Grant, *Int. J. Rapid Solidif.*, Vol. 2, 1986, p. 21.
- [85] S. Annavarapu, D. Apelian and A. Lawley, *Metall. Trans. A*, Vol. 19A, 1988, p. 3077.
- [86] P. Bewlay and B. Cantor, in *Rapidly Solidified Materials*, edited by P. Lee and R. Carbonara, ASM International, Materials Park, Ohio, 1986, p. 15.
- [87] E. J. Lavernia, T. Ando and N. J. Grant, in *Rapidly Solidified Materials*, edited by P. Lee and R. Carbonara, ASM International, Materials Park, Ohio, 1986, p. 29.
- [88] V. G. McDonnell, E. J. Lavernia and E. J. Samuels, in *Synthesis and Analysis in Materials Processing: Advances in Characterization and Diagnosis of Ceramic and Metal Particulate Processing*, edited by E. J. Lavernia, H. Henein and I. Anderson, TMS, Warrendale, PA, 1989, p. 29.
- [89] R. W. Smith and Z. Z. Mutasim, in *Thermal Spray Research and Applications*, edited by T. F. Bernecki, ASM International, Materials Park, OH, 1990, p. 369.
- [90] H. Gruner, *Thin Solid Film*, Vol. 118, 1984, p. 409.

- [91] K. Murakami, J. Imazu, Y. Fujii, T. Okamoto, T. Kawai, H. Matsumoto, T. Irisawa, K. Niihara and Y. Miyamoto, *Mater. Sci. Eng. A*, Vol. A174, 1994, p. 85.
- [92] J. McKelliget, J. Szekely, M. Vardelle and P. Fauchais, *Plasma Chem. & Plasma Proc.*, Vol. 2, 1982, p. 316.
- [93] R. W. Smith, D. V. Rigney, J. S. Smith and J. R. Raiden, in *Rapid Solidification Processing Principles and Technologies, III*, edited by R. Mehrabian, 1982, p. 468.
- [94] G. Rudinger, *Fundamentals of gas-particle flow*, Elsevier Scientific Pub. Co., Amsterdam, 1980.
- [95] S. L. Soo, *Multiphase fluid dynamics*, Gower, Aldershot, 1990.
- [96] C. Kittel, *Introduction to Solid State Physics*, Wiley, New York, 1991.
- [97] X. Liang and E. J. Lavernia, *Mater. Sci. Eng. A*, Vol. 161, 1993, p. 221.
- [98] E. A. Brandes, *Smithells Metals Reference Book*, Butterworths, London, 1983.
- [99] B. P. Bewlay and B. Cantor, *Mater. Sci. Eng. A*, Vol. 118, 1989, p. 207.
- [100] B. P. Bewlay and B. Cantor, *Metall. Trans. B*, Vol. 21, 1990, p. 899.
- [101] H. Schlichting, *Boundary-layer theory*, McGraw-Hill, New York, 1968.
- [102] H. Liu, Ph.D, University of Bremen, Bremen, Germany, 1990.
- [103] M. V. George, *Handbook of Chemistry and Physics*, Van Nostrand-Reinhold, 1970.
- [104] D. Liu, *Fundamentals of Thermal Energy Engineering*, Metallurgy Industry Press, Beijing, 1980.
- [105] P. Mathur, D. Apelian and A. Lawley, *Acta Metall.*, Vol. 37, 1989, p. 429.
- [106] E. Gutierrez-Miravete, E. J. Lavernia, G. M. Trapaga, J. Szekely and N. J. Grant, *Metall. Trans. A*, Vol. 20, 1989, p. 71.
- [107] E. J. Lavernia, E. M. Gutierrez, J. Szekely and N. J. Grant, *Int. J. Rapid Solidif.*, Vol. 4, 1988, p. 89.
- [108] H. A. Johnson and M. W. Rubesin, *Trans. ASME, J. Eng. Mater. Technol.*, Vol. 71, 1949, p. 447.
- [109] W. E. Ranz and W. R. Marshall, *Chem. Eng. Prog.*, Vol. 48, 1952, p. 141.
- [110] J. P. Hirth, *Metall. Trans. A*, Vol. 9, 1978, p. 401.
- [111] Y. Wu and E. J. Lavernia, *Metall. Trans. A*, Vol. 23, 1992, p. 2923.
- [112] D. Turnbull and J. C. Fisher, *J. Chem. Phys.*, Vol. 17, 1949, p. 71.
- [113] K. S. Dubey and P. Ramachandraraao, *Acta Metall.*, Vol. 32, 1984, p. 91.
- [114] P. S. Grant, B. Cantor and L. Katgerman, *Acta Metall. Mater.*, Vol. 41, 1993, p. 3097.
- [115] C. G. Levi and R. Mehrabian, *Metall. Trans. A*, Vol. 13, 1982, p. 221.
- [116] G.-X. Wang and E. F. Matthys, *Int. J. Heat Mass Transfer*, Vol. 35, 1992, p. 141.
- [117] T. W. Clyne, *Metall. Trans. B*, Vol. 15, 1984, p. 369.
- [118] X. Zhang and A. Atrens, *Int. J. Rapid Solidification*, Vol. 7, 1992, p. 83.

- [119] T. W. Clyne and W. Kurz, *Metall. Trans. A*, Vol. 12, 1981, p. 965.
- [120] X. Liang, J. C. Earthman and E. J. Lavernia, *Acta Metall. Mater.*, Vol. 40, 1992, p. 3003.
- [121] S. N. Ojha, A. K. Tripathi and S. N. Singh, *Powder Metall. Int.*, Vol. 25, 1993, p. 65.
- [122] M. C. Flemings and Y. Shiohara, *Mater. Sci. Eng.*, Vol. 65, 1984, p. 157.
- [123] P. A. Joly and R. Mehrabian, *J Mater Sci*, Vol. 9, 1974, p. 1446.
- [124] R. W. Smith and D. Apelian, *Pure & Appl. Chem.*, Vol. 62, 1990, p. 1825.
- [125] C. N. R. Rao, M. V. George, J. Mahanty and P. T. Narasimhan, *Handbook of Chemistry and Physics*, Van Nostrand-Reinhold Co., London, 1970.
- [126] J. Shackelford and W. Alexander, *The CRC Materials Science and Engineering Handbook*, CRC Press, Ann Arbor, MI, 1992.
- [127] E. Bourdin, P. Fauchais and M. Boulos, *Int. J. Heat Mass Transfer*, Vol. 26, 1983, p. 567.
- [128] E. Pfender, *Surf. Coating Tech.*, Vol. 34, 1988, p. 1.
- [129] R. Sivakumar, G. S. Sarma and M. P. Srivastava, *High Temp. Technol.*, Vol. 3, 1985, p. 151.
- [130] B. Champagne and S. Dallaire, in *Proceedings of the National Thermal Spray Conference*, edited by D. L. Houck, 1987, p. 25.
- [131] H. Liu, E. J. Lavernia and R. H. Rangel, *Atomization and Sprays*, Vol. 4, 1994, p. 369.
- [132] H. Liu, E. J. Lavernia and R. H. Rangel, *J. Phys. D: Appl. Phys.*, Vol. 26, 1993, p. 1900.
- [133] R. G. Castro, P. W. Stanek, L. A. Jacobson, D. F. Cowgill and L. L. Snead, in *Workshop on Beryllium for Fusion Applications*, 1993.
- [134] P. T. B. Shaffer, *Plenum Press Handbooks of High-Temperature Materials*, Plenum Press, New York, NY, 1964.
- [135] M. Rappaz, *Int. Mater. Rev.*, Vol. 34, 1989, p. 93.
- [136] J. Madejski, *Int. J. Heat Mass Transfer*, Vol. 19, 1976, p. 1009.
- [137] C. S. Marchi, H. Liu, A. Sickinger, E. Mühlberger, E. J. Lavernia and R. H. Rangel, *J. Mater. Sci.*, Vol. 28, 1993, p. 3313.
- [138] D. B. Kothe, R. C. Mjolsness and M. D. Torrey, 1991, *LA-12007-MS, UC-000*.
- [139] A. Itoh, M. Hirata and M. Ayagaki, in *1993 National Thermal Spray Conference*, 1993, p. 593.
- [140] R. A. Neiser, G. R. Smolik, K. J. Hollis and R. D. Watson, *J. Therm. Spray Tech.*, Vol. 2, 1993, p. 393.
- [141] D. B. Marshall, T. Noma and A. G. Evans, *J. Am. Ceram. Soc.*, Vol. 65, 1982, p. C175.
- [142] G. R. Anstis, P. Chantikul, B. R. Lawn and D. B. Marshall, *J. Am. Ceram. Soc.*, Vol. 64, 1981, p. 533.

- [143] J. J. Petrovic and R. E. Honnell, *J Mater Sci*, Vol. 25, 1990, p. 4453.
- [144] E. M. Levin, in *Phase Diagrams for Ceramists*, edited by E. M. Levin, H. F. McMurdie, F. P. Hall, M. K. Reser and H. Insley, The American Ceramic Society, Columbus, OH., 1956-1959, p. 5.
- [145] K. Sadananda, C. R. Feng, H. Jones and J. Petrovic, *Mater. Sci. Eng. A*, Vol. 155, 1991, p. 227.
- [146] K. Sadananda, H. Jones, C. R. Feng and J. Petrovic, *Ceram. Eng. Sci. Proc.*, Vol. 155, 1991, p. 227.
- [147] A. K. Ghosh, A. Basu and H. Kung, in *Intermetallic Matrix Composites II Symposium*, edited by D. B. Miracle, D. L. Anton and J. A. Graves, Mater. Res. Soc, 1992, p. 259.
- [148] S. Paik, P. C. Huang, J. Heberlein and E. Pfender, *Plasma Chem. Plasma Process.*, Vol. 13, 1993, p. 379.
- [149] J. J. Petrovic and A. K. Vasudevan, in *Intermetallic Matrix Composites II Symposium*, edited by D. B. Miracle, D. L. Anton and J. A. Graves, Mater. Res. Soc, 1992, p. 229.
- [150] M. Suzuki, S. R. Nutt and R. M. Aikin, in *Intermetallic Matrix Composites II Symposium*, edited by D. B. Miracle, D. L. Anton and J. A. Graves, MRS, 1992, p. 267.
- [151] W. R. Cannon and T. G. Langdon, *J Mater Sci*, Vol. 23, 1988, p. 1.
- [152] A. H. Chokshi and T. G. Langdon, *Mater. Sci. Technol.*, Vol. 7, 1991, p. 577.
- [153] O. D. Sherby and P. M. Burke, *Prog. Mater. Sci.*, Vol. 13, 1967, p. 325.
- [154] B. Y. Chivouze, D. M. Schwartz and J. E. Dorn, *Trans. Q. Am. Soc. Metals*, Vol. 60, 1967, p. 51.
- [155] F. A. Mohamed, *Metall. Trans. A*, Vol. 9, 1978, p. 1013.
- [156] K.-T. Park, E. J. Lavernia and E. A. Mohamed, *Acta Metall. Mater.*, Vol. 38, 1990, p. 1837.
- [157] M. S. Soliman, T. J. Ginter and F. A. Mohamed, *Phil. Mag.*, Vol. A48, 1983, p. 63.
- [158] P. E. Krajewski, J. E. Allison and J. W. Jones, *Metall. Trans. A*, Vol. 24, 1993, p. 2731.
- [159] R. W. Lund and W. D. Nix, *Acta Metall.*, Vol. 24, 1976, p. 469.
- [160] W. C. Oliver and W. D. Nix, *Acta Metall.*, Vol. 30, 1982, p. 1335.
- [161] R. W. Lund and W. D. Nix, *Metall. Trans. A*, Vol. 6, 1975, p. 1329.
- [162] K.-T. Park, E. J. Lavernia and F. A. Mohamed, *Acta Metall. Mater.*, Vol. 38, 1990, p. 2149.
- [163] F. A. Mohamed, K.-T. Park and E. J. Lavernia, *Mater. Sci. Eng. A*, Vol. 150, 1992, p. 21.
- [164] K.-T. Park, E. J. Lavernia and F. A. Mohamed, *Acta Metall. Mater.*, Vol. 42, 1994, p. 667.
- [165] F. A. Mohamed, *J Mater Sci*, Vol. 18, 1983, p. 582.

- [166] O. D. Sherby and P. M. Burke, *Prog. Mat. Sci.*, Vol. 13, 1968, p. 325.
- [167] F. A. Mohamed and T. G. Langdon, *Acta Metall.*, Vol. 22, 1974, p. 779.
- [168] P. K. Chaudhury and F. A. Mohamed, *Acta Metall. Mater.*, Vol. 36, 1988, p. 1099.
- [169] G. Gonzalez-Doncel and O. D. Sherby, *Acta Metall. Mater.*, Vol. 41, 1993, p. 2797.
- [170] R. S. Mishra and A. B. Pandey, *Metall. Trans. A*, Vol. 21, 1990, p. 2089.
- [171] A. B. Pandey, R. S. Mishra and Y. R. Mahajan, *Acta Metall. Mater.*, Vol. 40, 1992, p. 2045.
- [172] O. D. Sherby, R. H. Klundt and A. K. Miller, *Metall. Trans. A*, Vol. 8, 1977, p. 843.
- [173] A. K. Mukherjee, J. E. Bird and J. E. Dorn, *Trans. ASM*, Vol. 62, 1969, p. 155.
- [174] T. L. Dragone and W. D. Nix, *Acta Metall. Mater.*, Vol. 38, 1990, p. 1941.
- [175] A. Kelly and K. N. Street, *Proc. R. Soc. London*, Vol. 328A, 1972, p. 267.
- [176] G. Bao, J. W. Hutchinson and R. M. McMeeking, *Acta Metall. Mater.*, Vol. 39, 1991, p. 1871.
- [177] R. J. Arsenault and N. Shi, in *Proceedings of the International Conference on Low Energy Dislocation Structures*, 1986, p. 175.
- [178] J. Rosler, G. Bao and A. G. Evans, *Acta Metall. Mater.*, Vol. 39, 1991, p. 2733.
- [179] H. Lilholt, *Comp. Sci. Tech.*, Vol. 22, 1985, p. 277.
- [180] V. C. Nardone and K. M. Prewo, *Scr. Metall.*, Vol. 20, 1986, p. 43.
- [181] S. Goto and M. McLean, *Acta Metall. Mater.*, Vol. 39, 1991, p. 153.
- [182] S. Goto and M. McLean, *Acta Metall. Mater.*, Vol. 39, 1991, p. 165.
- [183] D. J. Srolovitz, R. A. Petkovic-Luton and M. J. Luton, *Philos. Mag. A*, Vol. 48, 1983, p. 795.
- [184] D. J. Srolovitz, R. A. Petkovic-Luton and M. J. Luton, *Acta Metall.*, Vol. 31, 1983, p. 2151.
- [185] D. J. Srolovitz, M. J. Luton, R. Petkovic-Luton, D. M. Barnett and W. D. Nix, *Acta Metall.*, Vol. 32, 1984, p. 1079.
- [186] T. L. Dragone, J. J. Schlautmann and W. D. Nix, *Metall. Trans. A*, Vol. 22, 1991, p. 1029.

## LIST OF PUBLICATIONS

A. Journal Papers

- (1). X. Zeng, H. Liu, M. Chu, and E.J. Lavernia, "An Experimental Investigation of Reactive Spray Atomization and Deposition Processing of Ni<sub>3</sub>Al/Y<sub>2</sub>O<sub>3</sub> Using N<sub>2</sub>-O<sub>2</sub> Atomization," *Metallurgical Transactions A*, Vol. 23A, pp. 3394-3399, 1993.
- (2). M. Gupta, T.S. Srivatsan, F.A. Mohamed and E.J. Lavernia, "Microstructural Evolution and Mechanical Properties of SiC/Al<sub>2</sub>O<sub>3</sub> Particulate Reinforced Spray Deposited Metal Matrix Composites," *Journal of Materials Science*, Vol. 28, pp. 2245-2259, 1993.
- (3). C. San Marchi, H. Liu, E. Muehlberger, A. Sickinger, E.J. Lavernia and R.H. Rangel, "Numerical Analysis of the Deformation and Solidification of a Single Droplet Impinging onto a Flat Substrate," *Journal of Materials Science*, in press, 1993.
- (4). Y.L. Jeng, J. Wolfenstine, D.E. Bailey, A. Sickinger and E.J. Lavernia, "Low Pressure Plasma Deposition of SiC-Reinforced MoSi<sub>2</sub>," *Scripta Metallurgica et Materialia*, Vol. 28, pp. 453-458, 1993.
- (5). H. Liu, X. Zeng and E.J. Lavernia, "Processing Maps for Reactive Atomization and Deposition Processing," *Scripta Metallurgica et Materialia*, Vol. 29, pp. 1341-1344, 1993.
- (6). J. Shyh, J. Wu and E.J. Lavernia, "Coarsening Behavior of Primary Si," *Scripta Metallurgica et Materialia*, Vol. 29, pp. 31-36, 1993.
- (7). Y.L. Jeng, E.J. Lavernia, J. Wolfenstine, D.E. Bailey and A. Sickinger, "Creep Behavior of Plasma Sprayed SiC-Reinforced MoSi<sub>2</sub>," *Scripta Metallurgica et Materialia*, Vol. 29, pp. 107-111, 1993.
- (8). H. Liu, E.J. Lavernia and R.H. Rangel, "Numerical Simulation of Impingement of Molten Ti, Ni and W Droplets on a Flat Substrate," *Journal of Thermal Spray Technology*, Vol. 2, No. 4, pp. 369-378, 1993.
- (9). T.S. Srivatsan and E.J. Lavernia, "Cyclic Strain Resistance of a Spray Atomized and Deposited Cast Aluminum Metal Matrix Composite," *Composites Engineering, an International Journal*, Vol. 4, No. 4, pp. 459-472, 1994.
- (10). Y. Wu , J. Zhang and E.J. Lavernia, "Modeling of the Incorporation of Ceramic Particulates in Metallic Droplets During Spray Atomization and Co-Injection," *Metallurgical Transactions A*, Vol. 25B, pp. 135-147, 1994.
- (11). J.L. Jeng and E.J. Lavernia, "Processing of Molybdenum Disilicide - A Review," *Journal of Materials Science*, Vol. 29, pp. 2557-2571, 1994.
- (12). J.A. Juarez-Islas, R. Perez, P. Lengsfeld, and E.J. Lavernia, "Microstructural and Mechanical Evaluations of Spray-Deposited 7XXX Al Alloys after Conventional Consolidation," *Materials Science and Engineering A*, Vol. A179/A180, pp. 614-618, 1994.

- (13). H. Liu, E.J. Lavernia and R.H. Rangel, "Numerical Investigation of Micro-Pore Formation During Impact of Molten Droplets in Plasma Spray Processes," *Atomization and Sprays*, Vol. 4, No. 4, pp. 369-384, 1994.
- (14). J. Zhang, Y. Wu and E.J. Lavernia, "Kinetics of Ceramic Particulate Penetration into Spray Atomized Metallic Droplets at Variable Penetration Depth," *Acta Metallurgica et Materialia*, Vol. 42, No. 9, pp. 2955-2972, 1994.
- (15). W. Cai, D. Bailey, A. Sickinger, and E.J. Lavernia, "Low Pressure Plasma Deposition of W," *Journal of Thermal Spray Technology*, Vol. 3, No. 2, pp. 135-141, 1994.
- (16). D. Baskin, J. Wolfenstine and E.J. Lavernia, "Elevated Temperature Mechanical Behavior of CoSi and Particulate Reinforced CoSi produced by Spray Atomization and Deposition," *Journal of Materials Research*, Vol.9, No.2, pp. 362-71, 1994.
- (17). R.W. Hayes, Y.L. Jeng, E.J. Lavernia and J. Wolfenstine, "Preliminary Characterization of the Room Temperature Fracture Behavior of Monolithic and Composite Fe-Al<sub>3</sub>-Fe<sub>2</sub>Al<sub>5</sub>," *Scripta Metallurgica et Materialia*, Vol. 32, No. 3, pp. 433-437, 1995.
- (18). X. Zeng and E.J. Lavernia, "Creep Behavior of Dispersion Strengthened Ni<sub>3</sub>Al Intermetallic Processed using Reactive Atomization and Deposition," *Scripta Metallurgica et Materialia*, Vol.32, No.7, pp 991-6, 1995.
- (19). X. Zeng, E.J. Lavernia and J.M. Schoenung, "Solidification Behavior of Spray Atomized Silicon Droplets," *Scripta Metallurgica et Materialia*, Vol.32, No.8, pp1203-8, 1995.
- (20). X. Zeng, S. Nutt and E.J. Lavernia, "Microstructural Characterization of Ni<sub>3</sub>Al Processed by Reactive Atomization and Deposition," *Metallurgical Transactions A*, Vol. 26A, No.4, pp. 817-27, 1995.
- (21). Y.L. Jeng, E.J. Lavernia, R. M. Hayes, and J. Wolfenstine, "Creep Behavior of Al Rich Fe-Al Intermetallics," *Materials Science and Engineering A*, Vol.A192-A193, pp. 240-8, 1995.
- (22). D. Lawrynowicz J. Wolfenstine and E.J. Lavernia, "Reactive Synthesis and Characterization of MoSi<sub>2</sub>/SiC using Low Pressure Plasma Deposition and 100% Methane", *Scripta Metallurgica et Materialia*, Vol.32, No.5, pp.689-93, 1995.
- (23). H. Liu, R.H. Rangel and E.J. Lavernia, "Modeling of Droplet-Gas Interactions in Spray Atomization of Ta-2.5W Alloy," *Materials Science and Engineering A*, Vol.A191, No.1-2), pp.171-84, 1995.
- (24). J. Wolfenstine, Y.L. Jeng and E.J. Lavernia, "Elevated Temperature Behavior of Plasma Sprayed MoSi<sub>2</sub>-SiC<sub>p</sub> Composites," *Materials Science and Engineering A*, Vol.A189, No.1-2, pp.257-66, 1995.
- (25). Y. L. Jeng, E.J. Lavernia, R.M. Hayes and J. Wolfenstine, "Creep Behavior of Al-Rich Fe-Al Intermetallics" *Materials Science and Engineering*, Vol. A192/193, pp. 240-248, 1995.
- (26). Y.L. Jeng, R. Hayes, J. Wolfenstine and E.J. Lavernia, "Powder Metallurgy Processing of Dual Phase Al rich Fe-Al Intermetallics," *International Journal of Powder Metallurgy*, in press, 1995.

- (27). H. Liu, E.J. Lavernia and R.H. Rangel, "An Analysis of Freeze-Up Phenomena During Gas Atomization of Metals," *International Journal of Heat and Mass Transfer*, in press, 1995.
- (28) W.D. Cai, Y. Li, R. Dowding, F. A. Mohamed, and E.J. Lavernia, "A Review of Tungsten Based Alloy as a kinetic energy penetrator materials," *Reviews in Particulate Materials*, in press, 1995.

B. Papers in Conference Proceedings

- (1). K.T. Park, E.J. Lavernia and F.A. Mohamed, "A Comparison of Creep Behavior of 6061 Al and SiC-6061 Al," in conference proceedings, *Symposium on Processing, Fabrication and Performance of Composite Materials II*, T.S. Srivatsan and E.J. Lavernia, eds., American Society of Mechanical Engineers, Winter Annual Meeting, Anaheim, CA, (1992).
- (2). M. Gupta, T.S. Srivatsan, F.A. Mohamed, and E.J. Lavernia, "Influence of Spray Atomization and Co-Deposition on the Microstructure and Mechanical Properties of Al-Cu Based Metal Matrix Composites," in conference proceedings, *Symposium on Processing, Fabrication and Performance of Composite Materials II*, T.S. Srivatsan and E.J. Lavernia, eds., American Society of Mechanical Engineers, Winter Annual Meeting, Anaheim, CA, (1992).
- (3). E.J. Lavernia and Y. Wu, "Synthesis in the Semi-Solid State using Spray Atomization and Co-Deposition," proceedings of symposium *on the Nature and Properties of Semi-solid Materials*, J. A. Sekhar and J.A. Dantzig, eds., Annual 1992 TMS meeting, San Diego, CA, The Metallurgical Society, Warrendale, PA, pp. 201-230, 1992.
- (4). E.J. Lavernia, "Recent Development in the Synthesis of Particulate Reinforced Metal Matrix Composites using Spray Atomization and Co-Deposition," *Indian Defense Journal, Special Issue on Materials Science and Engineering*, iVol. 43, Number 4, October 1993, pp. 301-323.
- (5). K.T. Park, E.J. Lavernia and F.A. Mohamed, "High Temperature Deformation of 6061-Al Produced by Powder Metallurgy," in conference proceedings, *Advanced Synthesis of Engineered Structural Materials*, American Society for Metals, J. Moore, E.J. Lavernia, and F. Froes, eds., August 30-September 2, San Francisco, CA, (1992).
- (6). H. Liu, R.H. Rangel, E.J. Lavernia, E. Muehlberger, and A. Sickinger, "Deformation and Interaction Behavior of Molten Tungsten Droplets Impinging on A flat Substrate In Plasma Spray Process," in conference proceedings, ASM International, National Thermal Spray Conference, Anaheim, CA, (1993).
- (7). Y. L. Jeng, E.J. Lavernia, and J. Wolfenstine, "Processing and Mechanical Behavior of Plasma Sprayed SiC Reinforced MoSi<sub>2</sub>," *Processing and Fabrication of Advanced Materials III*, T.S. Srivatsan and J. Moore, eds., TMS 1993 Fall Meeting, Pittsburgh, PA, (1993).
- (8). Y. L. Jeng, J. Wolfenstine, and E.J. Lavernia; D. E. Bailey and A. Sickinger , "SiC Reinforced MoSi<sub>2</sub> Composites Prepared by Low-Pressure Plasma Deposition" *PM in Aerospace, Defense and Demanding Applications - 1993*, F. H. Froes ed., Metal Powder Industries Federation, Princeton, NJ, pp. 147-156, (1993).

- (9). H. Liu, E. Muehlberger, A. Sickinger, E.J. Lavernia and R.H. Rangel, "Numerical Investigation of Micro-Pore Formation During Substrate Impact of Molten Droplets in Spraying Processes," ASM International conference proceedings, National Thermal Spray Meeting, Boston, MA, (1994).
- (10). H. Liu, W. Cai, R.H. Rangel and E.J. Lavernia, "Numerical and Experimental Study of Porosity Evolution during Plasma Spray Deposition of W," conference proceedings, NATO Advanced Materials Conference, M.A. Otooni, ed., Science and technology of Rapid Solidification Processing, Kluwer Academic Publishers, pp. 73-107, West Point, NY (1994).
- (11). Y.C. Wu, E. Chin and E.J. Lavernia, "Microstructure and Aging Response of Spray Deposited Al-Li/TiC<sub>p</sub>," in *High Performance Metal and Ceramic Composites*, K. Upadhyaya, ed., The Metallurgical Society, Warrendale, PA, pp. 13-22, (1994).
- (12). W. D. Cai, F. A. Mohamed, A. Sickinger, E. Muehlberger, D. Bailey and E. J. Lavernia, "Porosity Evolution During Low Pressure Plasma Spraying of W", conference proceedings, International Conference on Tungsten & Refractory Metals, Washington, D. C., (1994).
- (13). D.E. Lawrynowicz, J. Wolfenstine, S. Nutt, D. E. Bailey, A. Sickinger, A.M. Hirt, , and E.J. Lavernia, "In-Situ Processing and Characterization of MoSi<sub>2</sub>/SiC Processed by Reactive Low Pressure Plasma Deposition," Conference proceedings, 1995 MRS Meeting, Boston, MA, (1995).

#### C. Invited Papers and Lectures

- (1) "Interaction Mechanisms in Metal Matrix Composites," lecture presented at the Chinese MRS meeting, Beijing, China, November 14, 1994.
- (2) "Fundamentals of Spray Atomization and Deposition," lecture presented at the Shanghai Iron and Steel Research Institute, Shanghai, China, November 16, 1994.
- (3) "Spray Atomization and Deposition: an Overview," invited lecture presented at the Alcoa Technical Center, Alcoa Center, PA, July 16, 1994.
- (4) "Spray Atomization and Deposition Processing of MMCs," invited lecture presented at the III International Conference on Materials Science and sponsored by the National Academy of Materials Scientists (Mexico), Cancun, Mexico, September 26-29, 1994.
- (5) "Numerical Simulation of Microporosity Evolution during Droplet Impingement," lecture presented at the Sandia National Laboratories, Albuquerque, NM, January 21, 1994.
- (6) "Spray Atomization and Deposition of Elevated Temperature Materials," invited lecture presented at the Ford Research Center, Dearborn, MI, July 15, 1994.
- (7) "Spray Deposition of Metal Matrix Composites," lecture presented at the Institute of Metals Research, Academia Sinica, Shenyang, China, July 23, 1993.
- (8) "Fundamental Transport Phenomena during Spray Atomization and Deposition," lecture presented at the Beijing Institute of Aeronautical Materials, Beijing, China, July 19, 1993.

- (9) "Recent Developments in the Spray Processing of Structural Materials," lecture presented at the Science and Technology Research Center, Kobe Corp., Kobe, Japan, July 9, 1993.
- (10) "Spray Deposited Materials: Microstructure, Properties and Applications," lecture presented at the Beijing Institute of Aeronautical Materials, Beijing, China, July 19, 1993.
- (11) "Non-Equilibrium Processing of Advanced Structural Materials," lecture presented at the 27th National Heat Transfer Conference & Exposition, Minneapolis, MN, July 28-31, 1991.

**LIST OF PARTICIPATING SCIENTIFIC PERSONNEL**

- |    |                    |  |
|----|--------------------|--|
| 1. | Dr. E. J. Lavernia | Principal Investigator, UCI, Irvine, CA    |
| 2. | Dr. F. A. Mohamed  | Co-Principal Investigator, UCI, Irvine, CA |
| 3. | Mr. I. Sauer       | Laboratory Technician, UCI, Irvine, CA     |
| 4. | Ms. H. Liu         | Assistant Specialist, UCI, Irvine, CA      |
| 5. | Mr. W. D. Cai      | Ph.D candidate (completion date: 1996)     |
| 6. | Mr. Y. Li          | Ph.D candidate (completion date: 1996)     |